

**SEISMIC CHARACTERIZATION OF MARINE
GAS HYDRATES AND FREE GAS AT
NORTHERN HYDRATE RIDGE, CASCADIA
MARGIN**

Dissertation

zur Erlangung des Doktorgrades
der Mathematisch-Naturwissenschaftlichen Fakultät
der Christian-Albrechts-Universität
zu Kiel

vorgelegt von

Carl Jörg Petersen

Kiel
2004

Referent: Prof. Dr. E. R. Flüh
Koreferent: Prof. Dr. W. Rabbel
Tag der mündlichen Prüfung:

Zum Druck genehmigt: Kiel,

Der Dekan
gez.

Contents

Abstract	v
Zusammenfassung	vii
1 Introduction	1
1.1 Gas Hydrates	1
1.2 Motivation and structural outline	3
2 Area of investigation - Hydrate Ridge	5
2.1 Regional structural setting	5
2.2 Gas hydrates and free gas at Hydrate Ridge	6
2.2.1 ODP Leg 146 - Site 892	7
2.2.2 ODP Leg 204	8
2.3 Database for this study	8
2.3.1 SO150 HYDGAS	8
2.3.2 MCS survey OR89	9
2.3.3 ODP Leg 146 - Site 892	10
3 Data processing	11
3.1 Seismic sources	11
3.2 OBH/S data	13
3.2.1 Relocation	13
3.2.2 Filtering	14
3.2.3 OBS component rotation	16
3.3 SCS data	18
4 Regional SCS data analysis	21
4.1 Structural analysis	21
4.2 Regional BSR analysis	24
4.2.1 BSR depth	24
4.2.2 Heatflow	28
4.2.3 SCS amplitude analysis	31
5 Velocity analysis	33
5.1 Traveltime inversion of OBH/S data	33
5.1.1 Model assessment	35

5.1.2	Interpretation of inversion result	37
5.2	ODP Site 892 velocity data	38
5.3	OR89-09 prestack depth migration	40
5.4	Shear wave velocities	42
6	Amplitude analysis	45
6.1	Reflectivity and AVO	45
6.2	Amplitude analysis at location OBS 41	47
6.2.1	Determination of v_p , ρ and Q_p	49
6.2.2	Determination of v_s and Q_s	55
6.3	PP AVO analysis of OBH/S data	60
6.4	MCS profile OR89-09	63
7	Estimation of hydrate and free gas saturation	67
7.1	Bulk and shear modulus	69
7.2	Hydrate saturation	70
7.3	Free gas saturation	71
7.4	Error discussion	74
8	Discussion and conclusions	75
9	Outlook	83
	Bibliography	85
	A Model statistics	95
	Acknowledgments	97
	Curriculum Vitae	99
	Eidesstattliche Erklärung	101

Abstract

Gas hydrates occur in huge quantities in the sediments at continental margins. Knowledge of the amount of methane stored in hydrates and of their spatial distribution is of great importance with respect to their potential economical use, their possible impact on global climate and their effect on seafloor stability.

To address these questions, a high-resolution seismic experiment was carried out at northern Hydrate Ridge in the accretionary complex of the Cascadia subduction zone. The experiment was specifically designed for hydrate investigations. The main focus was the deployment of different source and receiver systems in order to enable both an area-wide and a detailed local assessment and quantification of the gas hydrate reservoir.

The analyses presented in this work include the processing and interpretation of the seismic data acquired with ocean bottom hydrophones/seismometers (OBH/OBS) and surface streamers. They allow a comprehensive characterization of the gas hydrate and free gas bearing sediments at northern Hydrate Ridge. The BSR, which marks the base of the gas hydrate stability zone (GHSZ), represents the interface between sediments containing gas hydrate and free gas. A detailed 2D P-wave velocity model is obtained from the OBH/S data by analyzing the seismic properties of the BSR. Relatively low velocities dominate and point to minor hydrate saturations in the sediments. To scrutinize this further, the amplitude behaviour of the BSR is investigated. By using synthetic seismogram modeling, a detailed model of the elastic parameters at the BSR interface beneath an OBS is developed. The main focus in this study is an AVO (amplitude versus offset) analysis of shear waves, which originate by conversion at the BSR. The AVO analysis enables the determination of the shear wave velocity above the BSR. A velocity of 400 m/s above the BSR indicates that already small hydrate saturations are sufficient to increase the shear modulus of the sediment.

Furthermore, information about the attenuation and the shape of the BSR transition zone is obtained from the frequency-dependent amplitude behaviour of the BSR. Average Q factors of $Q_p = 150$ for P-waves and of $Q_s = 35$ for S-waves are determined within the GHSZ. The low Q_s factor points to a pronounced attenuation of S-waves in the uppermost sediments. The BSR transition is shown to be of a gradual type and can be described by a 1.5-2.5 m wide zone. Moreover, the investigations indicate that the BSR amplitude is predominantly controlled by the amount of free gas below the BSR.

From rock physics modeling, the hydrate saturation is locally estimated to be 4-10 %. Below the BSR, free gas saturations of 0.5 % and 8 % are determined. These values depend on the model chosen for the free gas distribution.

The analysis of the area-wide 2D single channel streamer data provides a regional map of the spatial and depth distribution of the BSR. A heatflow model for the survey area

is obtained from the BSR depth distribution. Increased heatflow at the western flank of the ridge indicates active zones of upward migrating, warm, gas-rich fluids, which are subduction-related. The regional BSR amplitude distribution enables a rough estimate of the amount of hydrate-bound and free methane of 1.3-3.9 Mt/km³. In the surveyed area of ~20 km², an amount of 4.8-10.3 Mt methane is obtained.

Zusammenfassung

Gashydrate treten massiv in den meeresbodennahen Sedimenten der Kontinentalränder auf. Kenntnisse über die Menge des in Hydraten gespeicherten Methans und über ihre räumliche Verteilung sind von großer Bedeutung in Hinblick auf eine potenzielle wirtschaftliche Nutzung, auf ihre Auswirkung auf das globale Klima sowie auf ihren Einfluß auf die Meeresbodenstabilität.

Um diesen Fragen nachzugehen, wurde ein speziell auf Hydratuntersuchungen ausgelegtes hochauflösendes seismisches Experiment am nördlichen Hydratrücken im Akkretionskomplex der Cascadia-Subduktionszone durchgeführt. Schwerpunkt der Messungen war der Einsatz verschiedener Quellen und Empfänger, um sowohl eine flächenhafte als auch eine detaillierte lokale Erfassung und Quantifizierung der Gashydratvorkommen zu ermöglichen.

Die in dieser Arbeit präsentierten Analysen beinhalten die Bearbeitung und Auswertung der mit Ozeanboden-Hydrophonen/-Seismometern (OBH/OBS) und Oberflächen-Streamern aufgezeichneten seismischen Daten und erlauben eine umfassende Charakterisierung der Gashydrat und freies Gas haltigen Sedimente am nördlichen Hydratrücken. Der BSR (Bottom Simulating Reflector), der die Unterkante der Gashydratstabilitätszone (GHSZ) kennzeichnet, stellt die Grenzschicht zwischen Sedimenten mit Hydrat und freiem Gas dar. Ein detailliertes zweidimensionales P-Wellen-Geschwindigkeitsmodell kann aus den OBH/S-Daten erhalten werden. Relativ niedrige Geschwindigkeiten dominieren und deuten auf geringe Hydratsättigungen im Sediment hin. Um dies genauer zu untersuchen, wird zusätzlich das Amplitudenverhalten des BSRs untersucht. Mit Hilfe von synthetischen Seismogrammen kann ein detailliertes Modell der elastischen Parameter am BSR-Übergang unterhalb eines OBS entwickelt werden. Einen Schwerpunkt bildet dabei eine AVO (Amplitude versus Offset)-Analyse von Scherwellen, die durch Konversion am BSR entstanden sind. Sie erlauben die Bestimmung der Scherwellengeschwindigkeit über dem BSR. Eine Geschwindigkeit von 400 m/s über dem BSR deutet darauf hin, dass schon geringe Hydratsättigungen ausreichend sind, um die Scherfestigkeit des Sediments heraufzusetzen.

Ausserdem können aus dem frequenzabhängigen Amplitudenverhalten des BSRs Aussagen über die Dämpfung und über die Form der Übergangszone am BSR gemacht werden. Dämpfungswerte von $Q_p = 150$ für P-Wellen und $Q_s = 35$ für S-Wellen werden als Mittelwerte für die GHSZ bestimmt. Der niedrige Wert für Q_s deutet auf eine überaus starke Dämpfung der S-Wellen in den obersten Sedimentschichten hin. Der Übergang am BSR ist graduell und kann durch eine 1.5-2.5 m mächtige Zone beschrieben werden. Weiterhin zeigen die Untersuchungen, dass die BSR-Amplitude maßgeblich durch das freie Gas unterhalb des BSRs kontrolliert wird.

Ein gesteinsphysikalischer Ansatz ermöglicht eine lokale Abschätzung der Hydratkonzentration zu 4-10 % des Porenraums. Unterhalb des BSRs wird eine Sättigung an freiem Gas von 0.5 % bzw. 8 %, je nach zugrunde liegendem Modell für die Verteilung des freien Gases, bestimmt.

Eine regionale Kartierung der räumlichen und tiefenabhängigen Verteilung des BSRs wird durch die Auswertung flächenhafter 2D-Einkanalstreamerdaten erzielt. Aus der BSR-Tiefenverteilung kann ein Wärmeflussmodell für das Untersuchungsgebiet gewonnen werden. Stark erhöhter Wärmefluss an der westlichen Flanke des Rückens deutet auf aktive, subduktionsbezogene Aufstiegszonen von warmen, gasreichen Fluiden hin. Die regionale BSR-Amplitudenverteilung ermöglicht eine grobe Abschätzung der Menge des in Form von Gashydraten und freiem Gas vorliegenden Methans zu 1.3-3.9 Mt/km³. Für das untersuchte Gebiet, das eine Fläche von ~ 20 km² einnimmt, ergibt sich eine Gesamtmenge an Methan von 4.8-10.3 Mt.

Chapter 1

Introduction

1.1 Gas Hydrates

Gas hydrates, more accurately called gas clathrates, are solid, ice-like, crystalline substances composed of cages of water molecules that surround gas molecules of low-molecular-weight. Methane CH_4 is the dominant gas, which occupies more than 99% of the marine gas hydrate cages worldwide. The gas hydrate structure I, which predominantly forms with methane, is a body-centred cubic structure (Figure 1.1).

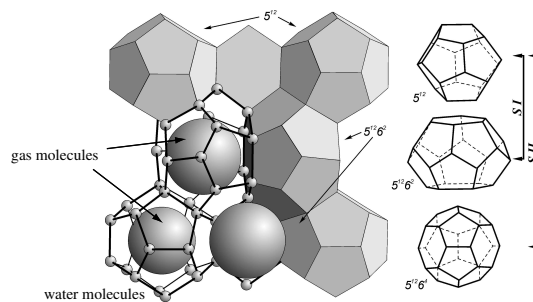


Figure 1.1: *Diagram of gas hydrate structure I (Greinert, 1999)*

Gas hydrates only form under appropriate low temperature and high pressure conditions, and when sufficient gas is supplied. The gas hydrate stability zone (GHSZ) is illustrated in Figure 1.2. In the natural environment, these conditions are met in two regions, in the onshore and offshore permafrost in polar regions and also in near surface marine sediments in the oceans and deep lakes at water depths greater than 300 m. In many places along the slopes and rises of continental and insular margins around the globe, gas hydrate appears to occur in huge quantities in the sediment up to 400 mbsf (meters below seafloor) (reviewed by *Kvenvolden, 1993*). Gas hydrates in oceanic sediment were directly observed for the first time in the Black Sea (*Yefremova and Zhizhchenko, 1974*).

The global amount of methane carbon in gas hydrate has been roughly estimated to be a factor of 2 larger than the carbon present in all known fossil fuel deposits (coal, oil and natural gas). A general consensus value of 10 Tt (teratons = 10^{15} kg) was suggested

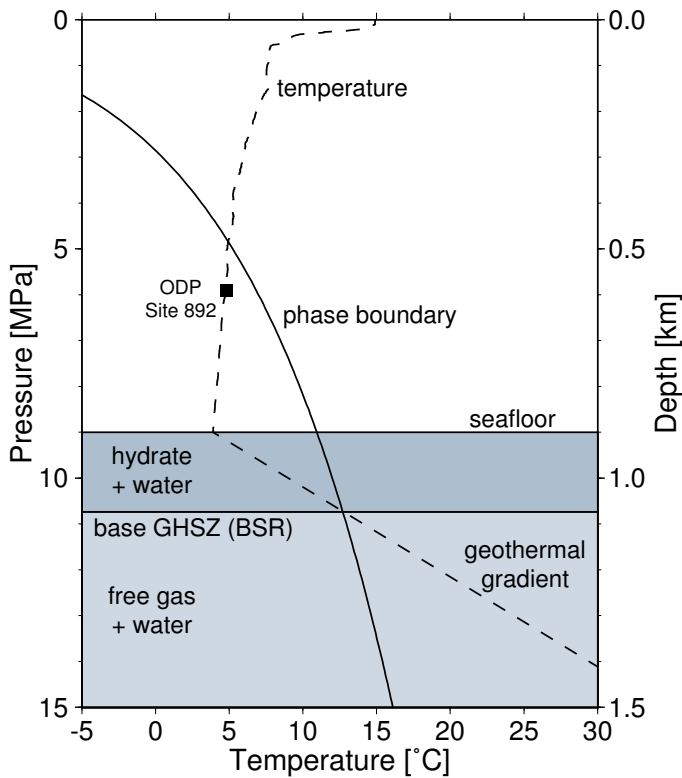


Figure 1.2:

Schematic profile of the GHSZ in marine sediments. The heavy line defines the limit in P/T of the stability field of methane hydrate for salt water derived from laboratory measurements (Dickens and Quinby-Hunt, 1994).

The effect of having a seafloor at 900m water depth is indicated by a temperature distribution typical for convergent margins (dashed line). The intersection of the local geotherm (51°C/km) with the temperature for three-phase equilibrium of the water-hydrate-free gas system defines the base of the GHSZ. In this example the GHSZ will extend from the seafloor to about 170m below it.

by Kvenvolden (1993); Kvenvolden and Lorenson (2001). Recently, the global estimates have been reviewed by Milkov (2004) who presented a lower estimate of 0.5-2.5 Tt.

Three aspects of gas hydrates are of significant importance:

- Potential Energy Resource

Marine gas hydrate might play a significant role as a future energy resource because of the enormous amount of methane contained in clathrate structures, its wide geographic distribution and its high energy density compared to other sources of gas (e.g. Collett, 2003). Under standard conditions, 1 m³ of methane hydrate can contain up to 164 m³ of methane gas (Sloan, 1998).

- Geologic Hazard

Continental margin sediment instability has been related to gas hydrate decomposition. Sediments in which gas hydrate grows are strengthened, whereas hydrate decomposition is hypothesized to weaken the sediment. This leads to the formation of horizons with increased potential for slope failures and submarine land slides (e.g., Paull et al., 2003). As a consequence, tsunamis, huge destructive waves, might be generated, which threaten coastal populations.

- Global Climate Change

In response to reduced hydrostatic pressure or increased bottom-water temperatures, huge amounts of methane can potentially be released from decomposing gas hydrates and introduced to the water column and atmosphere. Methane represents a very efficient greenhouse gas (about 100 times more efficient than CO₂). CO₂ is also generated by the oxidation of methane into water and carbon dioxide. Thus, methane

release from hydrate decomposition might contribute significantly to atmospheric greenhouse forcing and enhance global warming (e.g. *Haq*, 2003).

The above mentioned issues clearly show the necessity to investigate where, how and why gas hydrates occur in nature. The work presented here focuses on seismic methods used for a qualitative and quantitative assessment of a gas hydrate and free gas reservoir at northern Hydrate Ridge at the Cascadia convergent margin. In the following, due to the dominance of methane, the analyses will concentrate on methane hydrate only.

1.2 Motivation and structural outline

Seismic data analysis represents a powerful tool in hydrate research. On seismic sections the base of the GHSZ, where the phase transition from hydrated sediment to gas-containing sediment occurs, can be identified as a prominent reflector, the bottom simulating reflector (BSR). An example for a particularly strong BSR observed at northern Hydrate Ridge is given in Figure 1.3. The BSR generally mimics the seafloor at several hundred mbsf cutting through sedimentary strata. It has a reversed polarity with respect to the seafloor reflection due to the decrease in P-wave velocity. The BSR depth below seafloor depends on the water depth and the prevailing geothermal gradient, which forces hydrate dissociation beneath the BSR (see Figure 1.2). BSRs in seismic data have been widely used for identifying

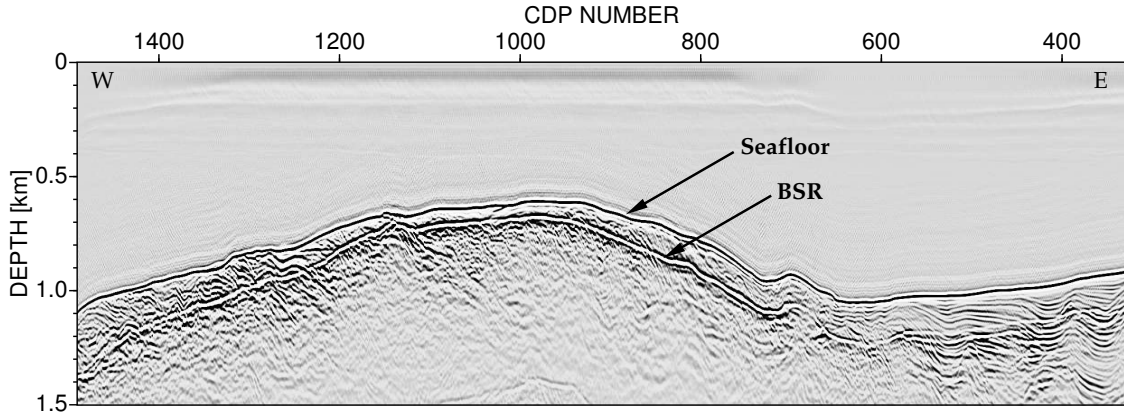


Figure 1.3: MCS profile OR89-09 after FD prestack depth migration illustrating BSR appearance at Hydrate Ridge.

and locating hydrate reservoirs (e.g., *Shipley et al.*, 1979). A detailed analysis of the sediment's seismic velocities offers a way to quantify the amounts of hydrate and free gas by comparing the obtained velocities with those calculated for sediments without hydrate. This analysis is hampered by the fact that there are commonly many uncertainties when calculating the hydrate- and gas-free sediment velocities. In general, drill hole information is needed. Pure methane hydrate has a P-wave velocity v_p of ~ 3.78 km/s and a shear wave velocity v_s of ~ 1.96 km/s (*Helgerud et al.*, 2003). Consequently, hydrate will increase the seismic velocities. Below the BSR v_p is decreased significantly by the presence of free gas in the pore space. This leads to a large negative impedance contrast at the BSR and produces the strong P-wave reflection. The deployment of ocean bottom instruments

allows to registrate the seismic wavefield at far offsets and thus enables a detailed velocity and amplitude-versus-offset (AVO) analysis. A typical ocean bottom hydrophone (OBH) seismogram is shown in Figure 1.4. In addition, ocean bottom seismometers (OBS) allow measurements of P-S converted waves and the determination of shear wave velocities. An investigation of the amplitudes of the BSR and their angle dependency (AVO behaviour) leads to a better estimate of the physical properties above and below the GHSZ.

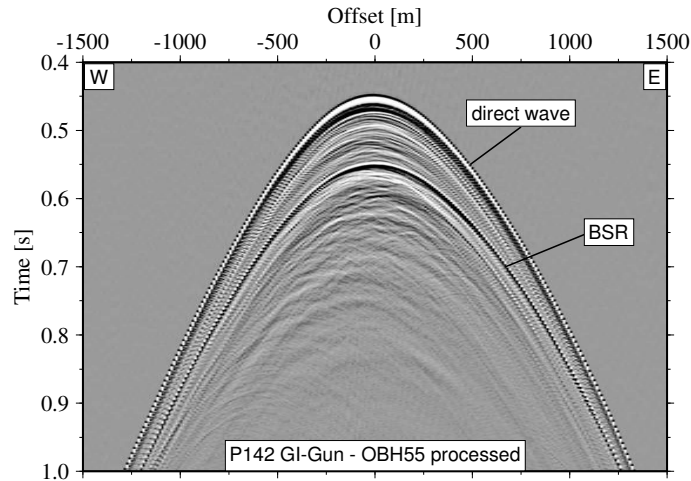


Figure 1.4: *Example of a typical OBH recording at northern Hydrate Ridge.*

This work is structured in the following parts:

Chapter 2 deals with the area of investigation, Hydrate Ridge. A short overview of the tectonic evolution and the gas hydrate environment is given followed by an introduction to the different data sets that were available for this study. Subsequently, Chapter 3 provides a description of the basic processing applied to the data sets. A detailed analysis of the single-channel streamer (SCS) data is provided in Chapter 4 to assess the regional hydrate reservoir properties. Chapter 5 refers to the velocity models obtained from the different data sets. An amplitude analysis is performed in Chapter 6 and includes the AVO effects of the BSR. The resulting model of the elastic parameters is used for a local estimate of the amounts of hydrate and free gas in the sediment based on rock physics modeling in Chapter 7. In Chapter 8, all obtained results are discussed, leading to a comprehensive characterization of the gas hydrate reservoir at northern Hydrate Ridge. Finally, an outlook is given in Chapter 9.

Chapter 2

Area of investigation - Hydrate Ridge

2.1 Regional structural setting

Along the Oregon-Washington margin upper Miocene (8 Ma) crust of the Juan de Fuca plate is obliquely subducted beneath North America (Figure 2.1) at a rate of about 42 mm/a (*Kulm et al.*, 1984; *DeMets et al.*, 1990). The basement of the Oregon continental shelf and Coast Range is formed by early Eocene-aged oceanic crustal rocks of the Siletz terrane, which were sutured to North America approximately 50 Ma ago. They are overlain by up to 7 km thick sedimentary basins. Seaward of the terrane a well-developed accretionary prism has evolved since convergence was initiated during the late Eocene (*Snively, 1987; Snively et al., 1980; Trehu et al., 1995*).

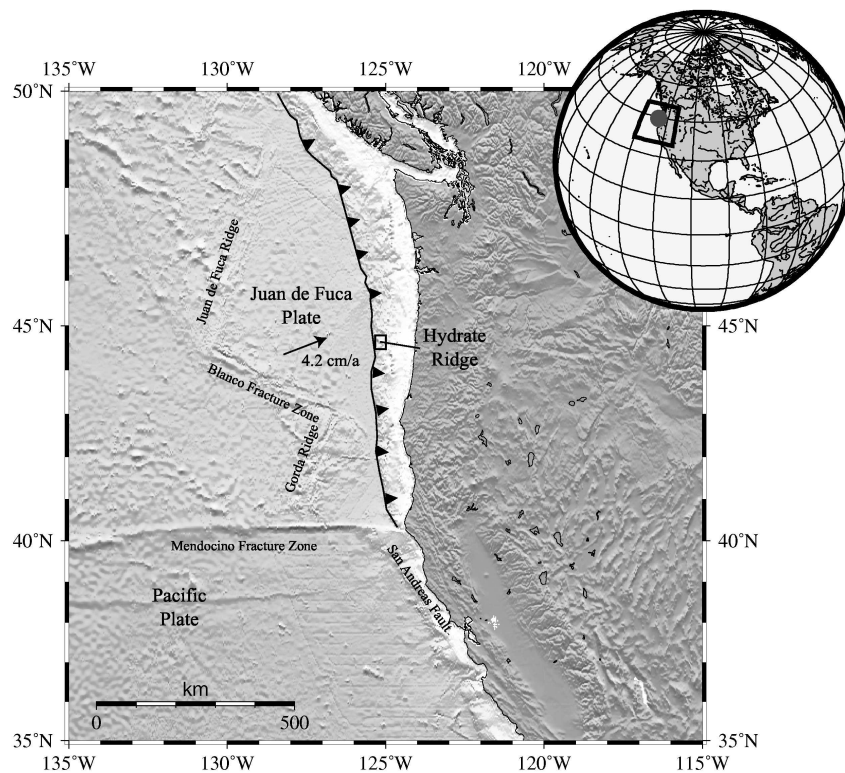


Figure 2.1: Tectonic setting of Cascadia subduction zone.

The incoming sediments of the Juan de Fuca plate consist of Pliocene/Pleistocene turbidites which exceed a thickness of 4 km at the toe of the slope (Cochrane *et al.*, 1988) and eliminate the topographic expression of the trench (Kulm *et al.* (1973), Kulm *et al.* (1984)). The along-strike deformation style changes from seaward verging structures (thrust faults dipping toward the continental plate) south of $44^{\circ}52'N$ to landward verging structures (thrust faults dipping toward the oceanic plate) north of $44^{\circ}52'N$ (MacKay *et al.*, 1992). Hydrate Ridge lies within the northern end of the seaward-vergent province, offshore central Oregon, and is the second seaward-vergent accretionary thrust ridge from the deformation front (Figure 2.2). The ridge is 25 km long and 15 km wide and has accumulated large volumes of mainly Pliocene sediments, which are imbricated against their onshore abutment (Westbrook *et al.*, 1994; MacKay, 1995). It is characterized by a northern summit peaking at about 590 m water depth and a southern peak at about 800 m.

2.2 Gas hydrates and free gas at Hydrate Ridge

Numerous geophysical and geological investigations of the gas hydrate environment at Hydrate Ridge have been carried out in the past. However, only the studies most relevant to the thesis are mentioned here.

In 1989, the multi-channel streamer (MCS) survey OR89 was carried out and collected several MCS profiles across Hydrate Ridge, which indicated the presence of hydrate and free gas by a prominent BSR appearance (MacKay *et al.*, 1992). Active venting and massive carbonate formation were discovered and investigated at the ridge by submersible dives and video observations during several research cruises in the past (e.g. Kulm *et al.*, 1986; Linke *et al.*, 1994; Bohrmann *et al.*, 1998; Brown *et al.*, 1999; Suess *et al.*, 1999;

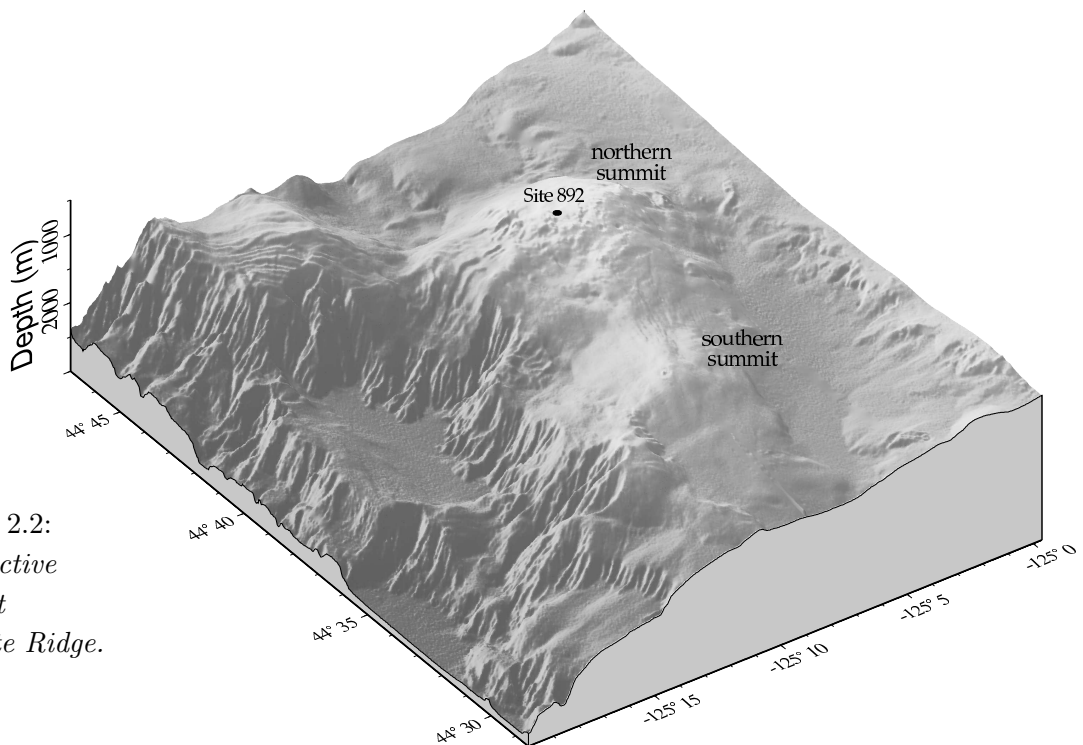


Figure 2.2:
Perspective
view at
Hydrate Ridge.

Torres et al., 2002; *Bohrmann and Suess*, 2001). At the northern ridge, hydrates and carbonates are exposed as a pavement at the seafloor leading to a rough bathymetry, which was mapped in detail by side-scan sonar and multibeam bathymetry surveys (e.g. *Carson et al.*, 1994; *Clague et al.*, 2001; *Johnson et al.*, 2003; *Klaucke et al.*, submitted). A model for the temporal and spatial evolution of a hydrate-bearing accretionary ridge based on a comparison between the southern and northern Hydrate Ridge has been proposed by *Trehu et al.* (1999). They speculated from the ubiquitous and strong BSR appearance that the northern ridge might be capped by hydrate and represent a more mature evolution stage than the southern ridge. The shallow depth, smooth top and steep sides of Hydrate Ridge have been suggested to be an indicator for hydrate deposits, which strengthen the sediments and lead to oversteepening of slopes and less frequent but larger slump events. Massive hydrate occurrence beneath a prominent chemoherm at northern Hydrate Ridge was postulated from high amplitude and chaotic reflectivity observed in seismic data acquired in 2000 (*Trehu et al.*, 2002, 2004).

Hydrate Ridge was selected twice as a drilling site within the Ocean Drilling Program (ODP). In 1992, ODP Site 892 was drilled on the western flank of northern Hydrate Ridge during ODP Leg 146 (*Westbrook et al.*, 1994) and the southern ridge was investigated by nine sites of ODP Leg 204 in 2002 (*Trehu et al.*, 2003).

2.2.1 ODP Leg 146 - Site 892

The location of Site 892 was chosen to study the nature of the BSR and to investigate fluid-flow related to a major thrust fault. Gas hydrate was only found and sampled down to a depth of 19 mbsf, but low temperatures and discrete layers of anomalously high water contents and depleted chlorinity down to 68 mbsf suggest layers of disseminated gas hydrates. During recovery, the hydrates leave the stability field and start to dissociate. This is an endothermic reaction, which produces negative temperature anomalies. Furthermore, the bound fresh water will be released and freshen the pore water.

The visible hydrate was sampled as irregular clear nodules of a size of a few cm and as pellets of 4-5 mm distributed evenly with spacings of 50-60 mm (*Westbrook et al.*, 1994; *Hovland et al.*, 1995). The gas regime at Site 892 can be divided in a shallow layer down to 68 mbsf which is dominated by CH_4 (90-95 %). In the upper 19 m, which is a near-surface active sulfate reduction zone, significant amounts of H_2S (~10 %) were measured from dissociating hydrates (*Kastner et al.*, 1995, 1998). Isotopic analyses indicate that the methane was generated microbially (biogen) in the shallow regime. In the deep gas pool below 68 mbsf, increased concentrations of higher hydrocarbons indicate a change to a mixture of biogenic and thermogenic gases. These gases are believed to have migrated upward from greater depth driven by tectonically induced fluid flow (*Hovland et al.*, 1995). From the analysis of the chlorinity measurements at Site 892, the maximum hydrate content in the pore space was suggested to be ~16 % and it was suggested that finely disseminated hydrate prevails (*Kastner et al.*, 1995). Porosities derived from resistivity and neutron porosity measurements are broadly consistent with empirical trends for normally compacted sediments (*Hamilton*, 1976b) and range from ~67 % at the seafloor to ~57 % at the BSR (*Jarrard et al.*, 1995; *Moran et al.*, 1995).

2.2.2 ODP Leg 204

At the southern summit of Hydrate Ridge, high concentrations of gas hydrate (30-40 %) were found in the near-surface sediments down to a depth of ~ 30 mbsf whereas, away from the summit, no hydrate was present in the upper ~ 45 mbsf. Between 45 mbsf and the base of the GHSZ, gas hydrates are distributed in lenses that are probably controlled by the physical properties of the sediment. The average gas hydrate saturation for the locations away from the summit was estimated to be less than 2 % (Trehu *et al.*, 2004). For details, the reader is referred to the ODP report (Trehu *et al.*, 2003). Moreover, a discussion of the drilling results with respect to seismic data analysis can be found in Papenberg (in prep.).

2.3 Database for this study

Numerous different data sets were available for this study, which allow an integrated analysis of the hydrate environment at Hydrate Ridge. The main data part was acquired within the SO150 HYDGAS project and consists of multi-frequent seismic data including wide-angle ocean bottom recordings as well as single-channel streamer (SCS) acquisitions. Pre-existing multi-channel streamer (MCS) data and ODP borehole information complement the data set.

2.3.1 SO150 HYDGAS

In September 2000, the BMBF funded project SO150 HYDGAS was carried out at Hydrate Ridge on-board of R/V *Sonne* by the GEOMAR Research Center. The major aim was the quantification of gas hydrates and free gas in the sediments of the Cascadia accretionary wedge by using seismic methods. During the project, 120 streamer profiles with a total length of 1254 km were acquired at Hydrate Ridge. The wide-angle seismic measurements consisted of 7 deployments with a total of 70 ocean bottom hydrophones (OBH) and seismometers (OBS). A description of the OBH/S technology can be found in Flueh and Bialas (1996) and Bialas and Flueh (1999). Whereas the OBH only record pressure changes with the hydrophone sensor, the OBS operate a hydrophone and a three-component seismometer, which enables the registration of the full wave field. The main focus was put on a broad frequency range to increase the subsurface resolution which was achieved by using 5 different sources during the survey. Low frequencies were provided by a 321 Bolt-gun, the mid-frequency range from 100-200 Hz was covered by a 5.161 Prakla-airgun-array and a 1.721 GI-gun and finally, a 0.251 Watergun and a Sparker were used to obtain high-resolution data of 500 to more than 1000 kHz. In the northern survey area data from two OBH/S deployments and 49 streamer profiles were collected. The location maps of the wide-angle measurements used here are given in Figure 2.3.

The main E-W line highlighted by a bold line in Figure 2.3 was shot with all sources and was chosen parallel to the pre-existing MCS profile OR89-09 and crosses ODP Site 892. For a detailed analysis, the OBH/S were deployed closely around the ODP site separated by only about 200 m. The N-S-oriented crossline profiles are of great importance for the relocation of the deployment positions and also for the rotation of the seismometer components (Sections 3.2.1 and 3.2.3). In addition, a set of SCS profiles was

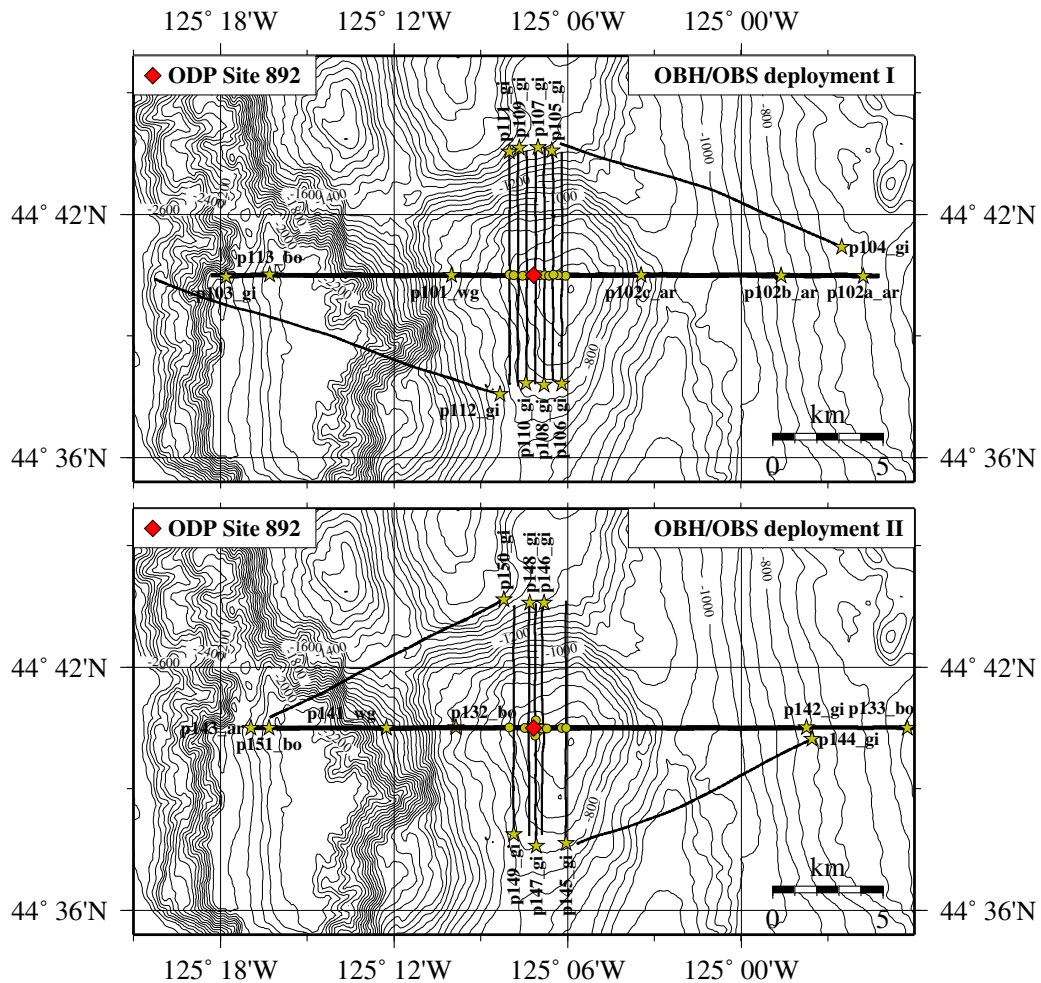


Figure 2.3: Location map of OBH/S measurements. Stars mark locations where profiles begin. Source types are abbreviated as follows: bo=Bolt-gun, ar=Prakla-array, gi=GI-gun, sp=Sparker, wg=Watergun.

acquired with the sparker and the GI-gun source at locations shown in Figure 2.4. These profiles complement the SCS data collected during the OBH/S measurements. Thus, a good SCS coverage of the northern summit area was obtained, which allows a regional characterization and will be referred to later in Chapter 4.

In summary, a total of 11 OBH and 6 OBS were operated successfully in the northern survey area. Together with data from 35 GI-gun profiles, 6 Sparker profiles and the main E-W profile shot with all sources, these form the database for this study. As it will be shown in subsequent chapters, the GI-gun proved to be a suitable source for investigating the BSR properties in both streamer and ocean bottom recordings.

2.3.2 MCS survey OR89

Regional MCS profiles were collected during a cruise off Oregon in 1989 (*MacKay et al.*, 1992) and were at the department's disposal for further processing. The seismic source was a tuned 4560 cubic inch airgun array fired at 25 m intervals. The streamer had 144 channels with a group spacing of 25 m yielding 72-fold CMP data with a CMP interval

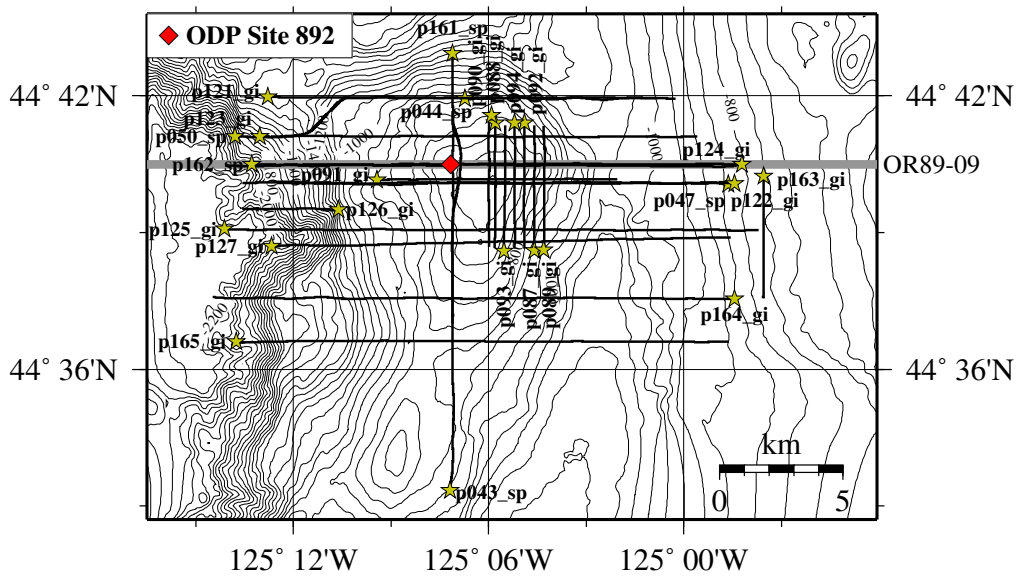


Figure 2.4: Location map of regional SCS lines.

of 12.5 m. The MCS profile OR89-09 is running parallel to the main E-W line and its location is given in Figure 2.4. Results from prestack depth migration and AVA inversion of line OR89-09 provided additional constraints for the velocity and amplitude modeling of the OBH/S data. They are shown and discussed later in Chapters 5 and 6.

2.3.3 ODP Leg 146 - Site 892

Drill hole data collected at Site 892 during ODP Leg 146 (*Westbrook et al.*, 1994) gave crucial information about sediment properties at northern Hydrate Ridge. The site is marked as a rhombus in the above shown location maps. Beside physical properties determined on recovered cores and discrete rock samples, downhole logging measurements yielded v_p , porosity and density as in situ properties. In addition, velocity information from a zero-offset vertical seismic profiling (VSP) experiment was available (*Westbrook et al.*, 1994; *MacKay et al.*, 1994, 1995). The log and VSP data are shown later in the particular sections when needed.

Chapter 3

Data processing

In this chapter, the seismic sources are introduced. A presentation of the processing steps follows, which have been applied to improve the data quality and which were necessary prerequisites for the conducted studies. For all seismic data, a similar basic data processing was applied, which consisted of frequency filtering and a residual static correction to account for small errors in trigger times and navigation, in the following termed swell-filtering. Moreover, the OBH/S data needed further specific processing - a relocation of the instrument positions and a rotation of the seismometer components.

3.1 Seismic sources

First, for each seismic source the wavelet and the frequency spectrum are shown in Figure 3.1 to illustrate the available frequency bandwidth. All wavelets were extracted from raw data of an OBH suspended on a rope several hundred meters in the water column, except for the MCS-Array signature which represents the near-trace seafloor reflection after processing and has zero-phase character. The suspended hydrophone allows to measure the far-field signature without interference of the seafloor reflection. Unfortunately, due to an overamplification of the hydrophone channels in the OBH recorders, the amplitudes of the direct wave were clipped in the near-offset area; that is, the amplitudes reached the maximum positive and negative values and were therefore useless. Thus, the source signatures had to be taken from unclipped traces at offsets ranging from 1 km for the GI-Gun and Sparker to 5 km for the Bolt-Gun. Directivity and ghost effects might possibly alter the wavelet shape slightly and introduce frequency notches, but can be considered to be of minor importance. As it is seen in the spectra, pairs of sources cover roughly a similar frequency range, i.e., Watergun and Sparker, GI-Gun and Airgun-Array and Bolt-Gun and the MCS-Array respectively. In Table 3.1 the resulting temporal and spatial resolutions are summarized. The main frequency f_m of the source pulse was obtained by taking the inverse of the temporal length of the main wavelet cycle. According to the $\lambda_m/2$ -criterion given by *Sheriff* (1980), which yields rather conservative estimates, the vertical resolution Δz can be calculated as a quarter of the main wavelength $\lambda_m/4$. An average medium velocity of 1550 m/s is assumed in the shallow sediments.

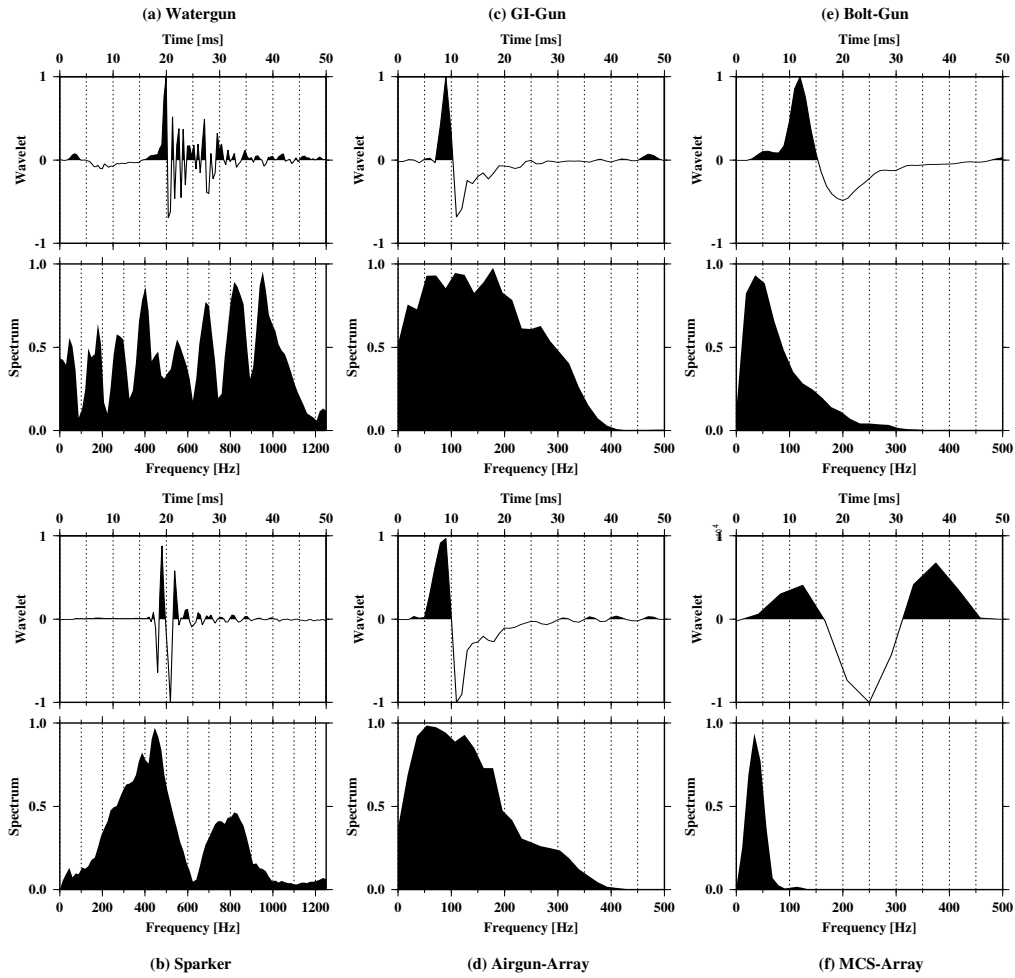


Figure 3.1: Source wavelets and associated frequency spectra.

As a measure of the horizontal resolution the first Fresnel radius r_F can be approximated using again the above criterium:

$$r_F = \sqrt{\frac{z \cdot \lambda_m}{2}}, \quad (3.1)$$

with reflection depth z set to 700 m. However, the calculated resolution values are only valid in the case of zero-offset data and a common source and receiver datum, i.e., SCS geometry. For the OBH/OBS configuration, the resolution estimation is more complex. Lowering the receiver to the seafloor leads to a smaller Fresnel radius of about 9 m for zero-offset; on the other hand, both vertical and horizontal resolutions decrease with increasing offset. A detailed discussion of this topic is beyond the scope of this work and can be found in *Otterbein (1997)*.

A selection of the profiles that were most appropriate for the presented study was made based on data quality. Looking at the spectra of the high-frequent sources, the Sparker wavelet shows a much smoother spectrum and would be preferred to the rather chaotic Watergun signature. However, due to unfavourable weather conditions, the Sparker SCS data of the main line was of worse quality than the Watergun profile P141. Moreover,

	Watergun	Sparker	GI-Gun	Airgun-Array	Bolt-Gun	MCS-Array
f_m	~ 550 Hz	~ 400 Hz	~ 130 Hz	~ 100 Hz	~ 42 Hz	~ 36 Hz
Δz	~ 0.7 m	~ 0.97 m	~ 3 m	~ 3.9 m	~ 9 m	~ 11 m
r_F	~ 31 m	~ 37 m	~ 65 m	~ 74 m	~ 114 m	~ 123 m

Table 3.1: *Temporal and spatial resolution (for SCS geometry) of seismic data.*

the Watergun profile was recorded by the OBH/OBS with a sufficient high sampling frequency of 2.5 kHz, whereas the Sparker was only sampled with 1 kHz. Therefore, only the Watergun was used for the high-frequent studies, but it must be mentioned that under calm weather conditions, the Sparker yields excellent data. The GI-Gun radiates energy in a broad frequency range from 30 to 350 Hz (Figure 3.1 (c)). The wavelet has a main frequency of ~ 130 Hz and its energy distribution is nearly minimum-phase. The typical airgun bubble, i.e., expanding air oscillations, is suppressed efficiently by the GI-gun. The Airgun-Array wavelet displayed in Figure 3.1 (d) has a main frequency of about 100 Hz. Comparing the low-frequent sources, the Bolt-Gun shows higher frequencies than the MCS-Array. Both the Airgun-Array and the Bolt-Gun suffer from strong bubble pulses with a periodicity of ~ 100 ms and ~ 142 ms, respectively. Due to their long delay, the bubble pulses are not displayed in Figure 3.1. Compared to the MCS data, the SCS data acquired with the Bolt-Gun provided no additional information and were therefore not further analyzed. Another disadvantage of the larger sources was the fact that even the BSR was strongly clipped in the near-offset range of the OBH data, and thus for BSR studies proved practically useless. In summary, it can be stated that the 1.71 GI-Gun represents an ideal source for hydrate investigations and therefore, it was mainly used for analyzing the BSR in the SCS and OBH/S data in this work.

3.2 OBH/S data

3.2.1 Relocation

In order to obtain the true positions of the OBH/S instruments at the seafloor a relocation is necessary. To determine the drift from the original deployment positions the travel time hyperbola of the direct wave is used. It can be calculated easily assuming a constant sound velocity in water and should be symmetrical for the correct position. The relocated positions are found by comparing the observed times of the direct wave with those calculated for varying positions until the best fit is obtained. Along a single profile, this scheme works accurately in inline direction but leaves the offline distance poorly determined. By incorporating the NS-running crossline profiles, the relocation could be performed in 3D leading to final position uncertainties of ± 5 m. The map in Figure 3.2 shows the relocated positions as black circles (OBH) and triangles (OBS) compared to the original positions marked as white circles. In general, the instruments have drifted less than 50 m. The resulting offline distances from the main profiles are summarized in Table 3.2. The average offset of 34 m is sufficiently small for the purpose of the conducted studies.

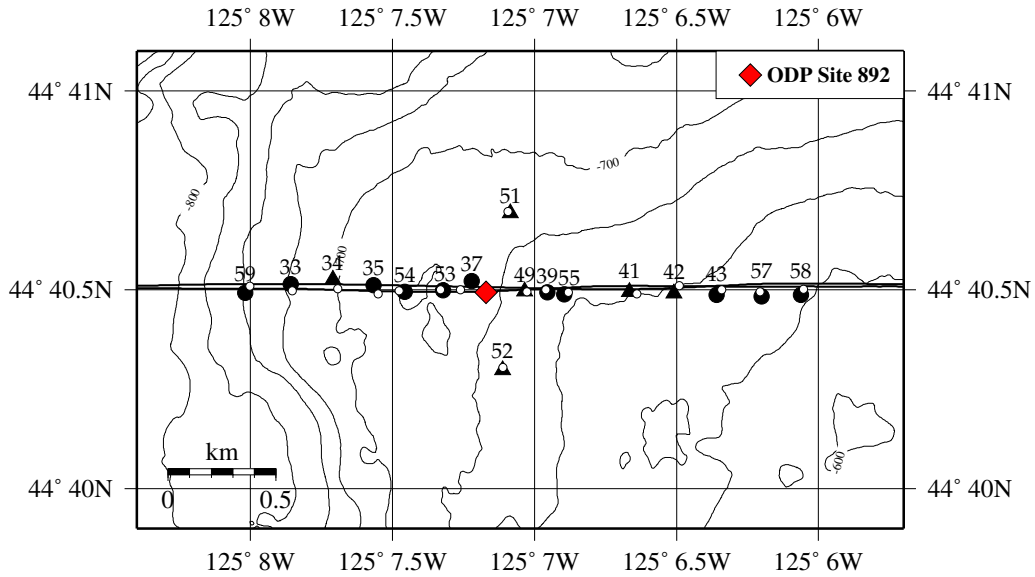


Figure 3.2: Relocated positions of OBH (black circles) and OBS (black triangles), white circles mark drop positions.

P103	Offline distance	P142	Offline distance	P147	Offline distance
OBH 33	20 m	OBS 49	15 m	OBS 51	34 m (P147)
OBS 34	46 m	OBH 53	17 m	OBS 52	32 m (P147)
OBH 35	28 m	OBH 54	29 m		
OBH 37	52 m	OBH 55	24 m		
OBH 39	17 m	OBH 57	62 m		
OBS 41	29 m	OBH 58	51 m		
OBS 42	34 m	OBH 59	46 m		
OBH 43	36 m				

Table 3.2: Final offline distances for OBH/S instruments after relocation.

3.2.2 Filtering

In order to improve the signal-to-noise ratio and to remove energy outside the frequency range of the source signal, an Ormsby band-pass frequency filter was applied to the data. The filter is designed in the frequency domain by specification of the corner frequencies of a trapezoidal-shaped amplitude spectrum. The filter operator in the time domain is obtained by inverse Fourier transform and the filtered output is then produced by convolution of the filter operator with the seismic trace. For the OBH/S data, different frequency filters with minimum-phase response were applied depending on source and receiver type. Since the hydrophone data predominantly show low-frequency noise, wide frequency bands of 10/25/350/400 Hz for the GI-Gun data and 50/80/1150/1250 Hz for the Watergun were chosen. For the GI-Gun seismometer components, a narrower band of 3/12/130/150 Hz was applied to retain the low-frequency shear waves and to remove higher-frequency noise of

~ 150 Hz, which seems to be related to the sensor coupling to the seafloor. The Watergun OBS data do not show any converted shear waves and have not been further processed. In addition to the frequency filter, a residual static correction, a so-called swell-filter, was applied to the data with the purpose of removing the effect of small errors in shot times or navigation. On the left side of Figures 3.3 and 3.4, the raw data of OBH 55 is shown for the GI-Gun and the Watergun. The seismic traces have been shifted to flatten the direct wave arrival to the zero-offset time t_0 according to the hyperbola equation given by:

$$\Delta t = \sqrt{t_0^2 + \left(\frac{x}{v_w}\right)^2} - t_0, \quad (3.2)$$

where x is the source-receiver offset and $v_w=1480$ m/s the wave velocity in water. This representation facilitates the identification of reflections and structural details and furthermore gives the opportunity to check the consistency of navigation, shot times and water velocity. As it can be seen in both data sets, the direct wave is undulating and jittering

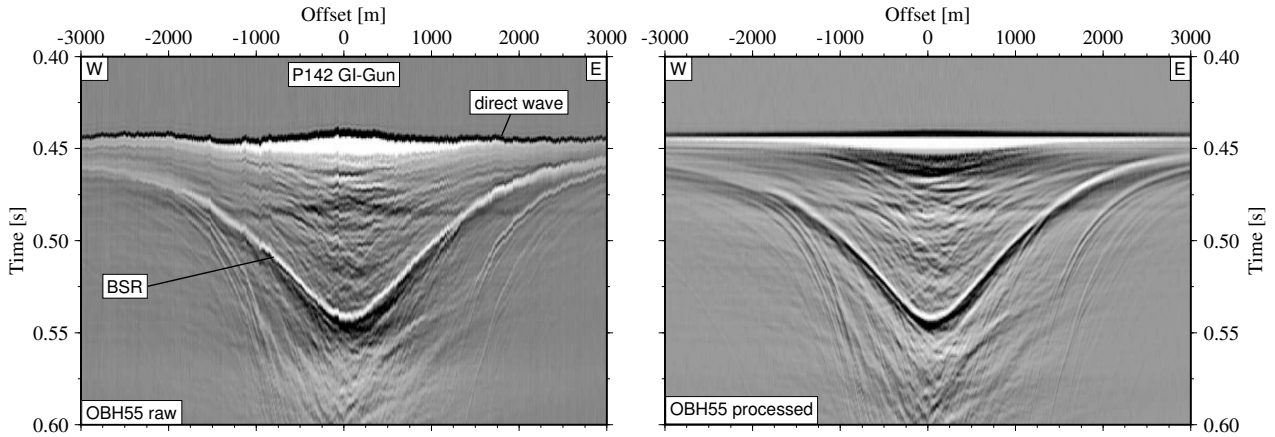


Figure 3.3: *OBH 55 before and after frequency filtering and swell-filtering.*

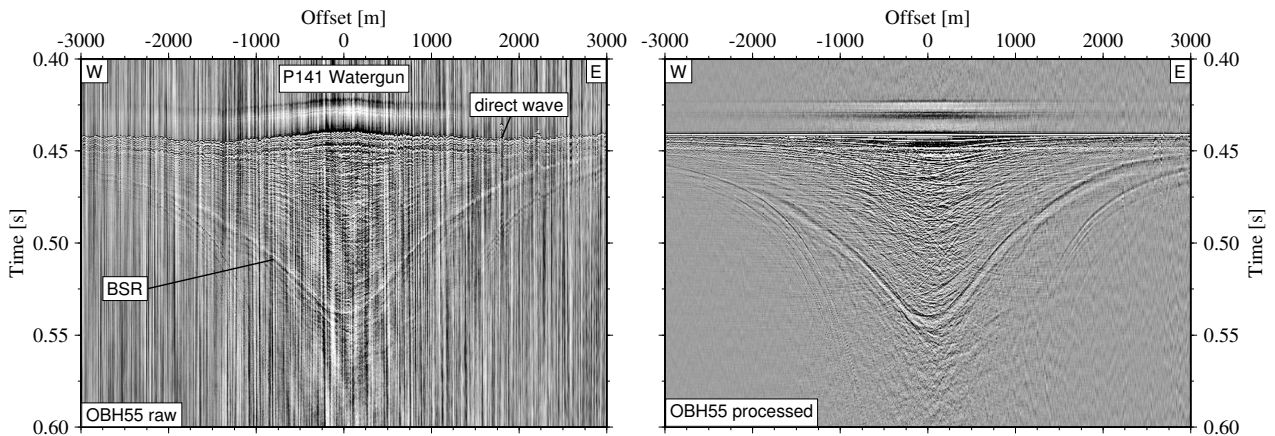


Figure 3.4: *OBH 55 before and after frequency filtering and swell-filtering.*

with abrupt shifts of a few ms. The jittering is caused predominantly by inaccuracies in shot times and in shot positions, which might be due to slightly varying airgun delay times, oceanic swell and variations in ship speed. The undulation is caused by uncertainties in the water depth at the receiver location and in the shot positions as well as by the assumption of a constant water velocity. The swell-filter determines the time sample of the first arrival and shifts it within each seismic trace to the desired time datum, which in this case is the t_0 time. The frequency- and swell-filtered sections are shown on the right side. The enhancements in s/n-ratio and coherency are clearly visible. However, the swell-filter may introduce absolute time shifts of up to ± 2 ms, i.e. the maximum undulation after flattening of the raw data. Keeping in mind what mainly causes this undulation, it is still reasonable to apply the swell-filter because a constant water velocity is also used in the velocity model and the data are perfectly consistent regarding water depth, shot time and position and water velocity. Additionally, if the undulation is caused by shot position inaccuracies, e.g. due to changing source offsets, a shift towards a time that is consistent with the navigation data does not increase the overall error.

3.2.3 OBS component rotation

A typical four-component OBS data set is displayed in Figure 3.5 consisting of the hydrophone component and three orthogonal seismometer components. When looking at the

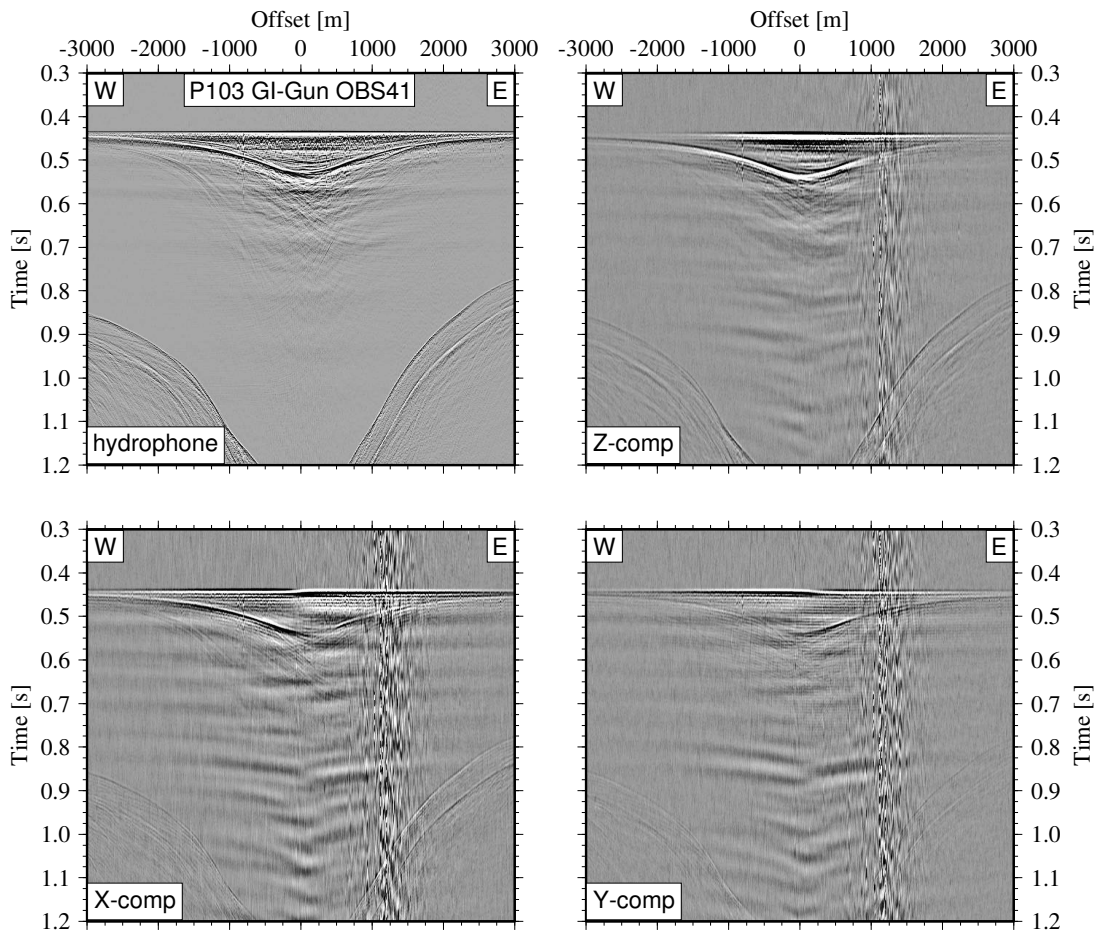


Figure 3.5: Four components of OBS41, filtered.

vertical z component, one can see from the asymmetrical amplitude decay of the direct wave with increasing offset that the geophone z -axis has an inclination to the vertical. The horizontal x and y components exhibit clear phase reversals in the near-offset range, which occurs when the seismic source passes the plane orthogonal to the particular horizontal component. Beside the compressional wave field, the seismometer components also show low-frequency shear wave phases at later traveltimes, which cannot be seen in the hydrophone data. These S-waves arise from P-waves which convert to shear waves when they encounter an interface where the shear modulus $\mu = v_s^2 \cdot \rho$ changes. Here v_s is the shear wave velocity and ρ is the density. For reflectors which are perpendicular to the plane given by the incoming P-wave and the vertical, the P-S converted waves are completely polarized vertically (SV). Obliquely dipping interfaces will excite additional S-wave energy out of the vertical plane that is horizontally polarized (SH). Since the BSR represents the by far strongest impedance contrast in the shallow sediments at Hydrate Ridge, the high-amplitude shear waves arriving at ~ 0.8 s are likely to have their origin in a P-S conversion at the BSR. In order to analyze the S-waves, the data must be rotated to a suitable coordinate frame. If the receiver components are rotated to simulate a receiver oriented in a radial (source to receiver), a transverse (orthogonal to radial) and a vertical direction, the P and SV energy will mainly be in the radial vertical plane.

In theory, after successful rotation the transversal component should contain almost no energy anymore unless SH waves are generated by conversion at non-horizontal or anisotropic layers. The rotation was accomplished using the industrial software package SEISMOS (Schlumberger). The module @ROTATE was applied to transfer the energy to the rotated components. It uses simple trigonometric relationships and also accounts for possible inclinations of the seismometers. The output was confirmed by applying the module @POLAR, which provides information about the orientation of the polarisation axes. The rotation result is shown in Figure 3.6. Most of the energy was transferred successfully to the radial component and the polarity flip disappeared. The strong P-S converted BSR phase now appears symmetrical and can be further analyzed (Section 6.2). The transversal component contains much less energy, but P-wave energy from the direct wave, and the BSR and the P-S converted phase are still visible. This might be due to an improper rotation, but it is more likely to be caused by 3D-effects and anisotropy. Strong energy pulses may have also jumped over to all components, leading to an incomplete

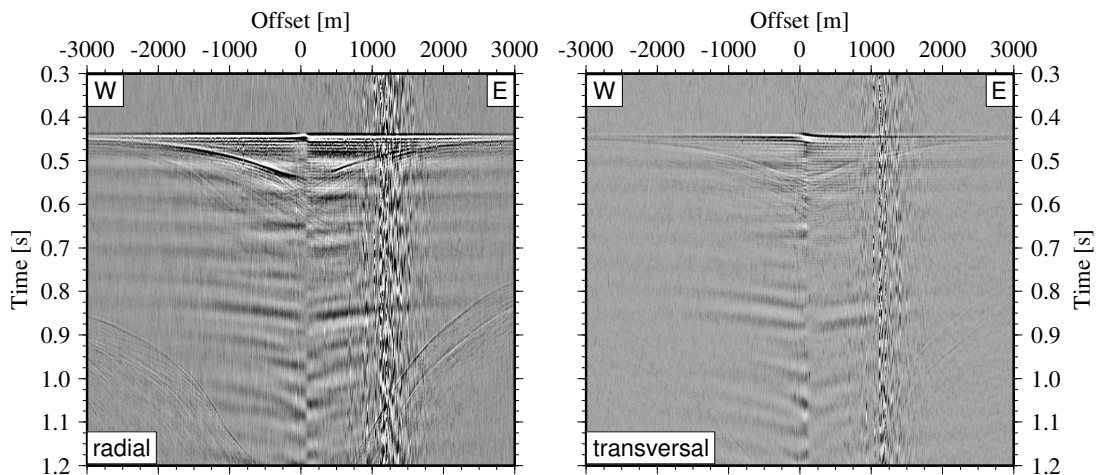


Figure 3.6: *Radial and transversal component of OBS 41 after rotation.*

removal of the direct wave energy.

3.3 *SCS data*

An Ormsby band-pass frequency filter was applied to the SCS data followed by a swell-filter. The swell-filter shifted the seafloor reflection arrivals to a smoothed datum which was obtained after filtering of the picked times. This was necessary to account for the observed jittering of a few ms due to inaccuracies in shot times and positions. The filtered data were input to a trace interpolation which added two traces per shot increment. Subsequently, the data were time-migrated with a constant velocity of 1480 m/s (water migration) using a f-k Stolt migration algorithm. The major aim of the migration was to collapse diffraction hyperbolas and to take focusing and defocusing effects into account.

This processing scheme was applied to all SCS profiles. The raw seismic sections of six selected GI-Gun profiles are displayed in Figure 3.7. These profiles cover the main area of interest west of the summit (see location map on top of Figure 2.3). The final time-migrated sections obtained after processing are shown in Figure 3.8. The migration successfully collapsed the diffractive energy and yielded data which allow an interpretation with respect to structural and amplitude variation. A strong and nearly ubiquitous BSR is visible, which is in some places disrupted and obscured by chaotic reflectivity. The profiles will be discussed in greater detail within the regional context in Chapter 4.

SCS data before processing

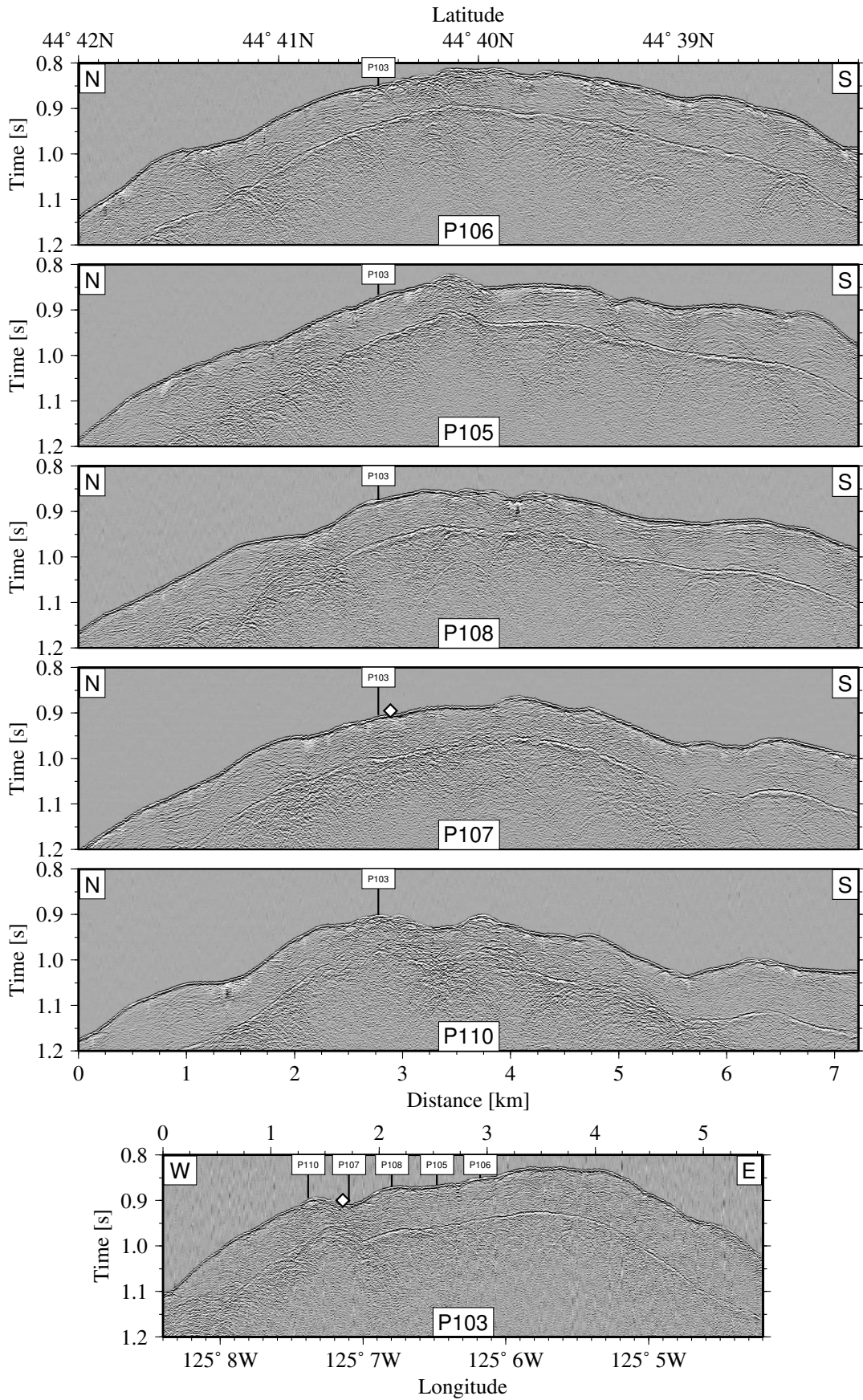


Figure 3.7: Selected SCS profiles before data processing, source: GI-Gun. White rhombus marks ODP Site 892.

SCS data after processing

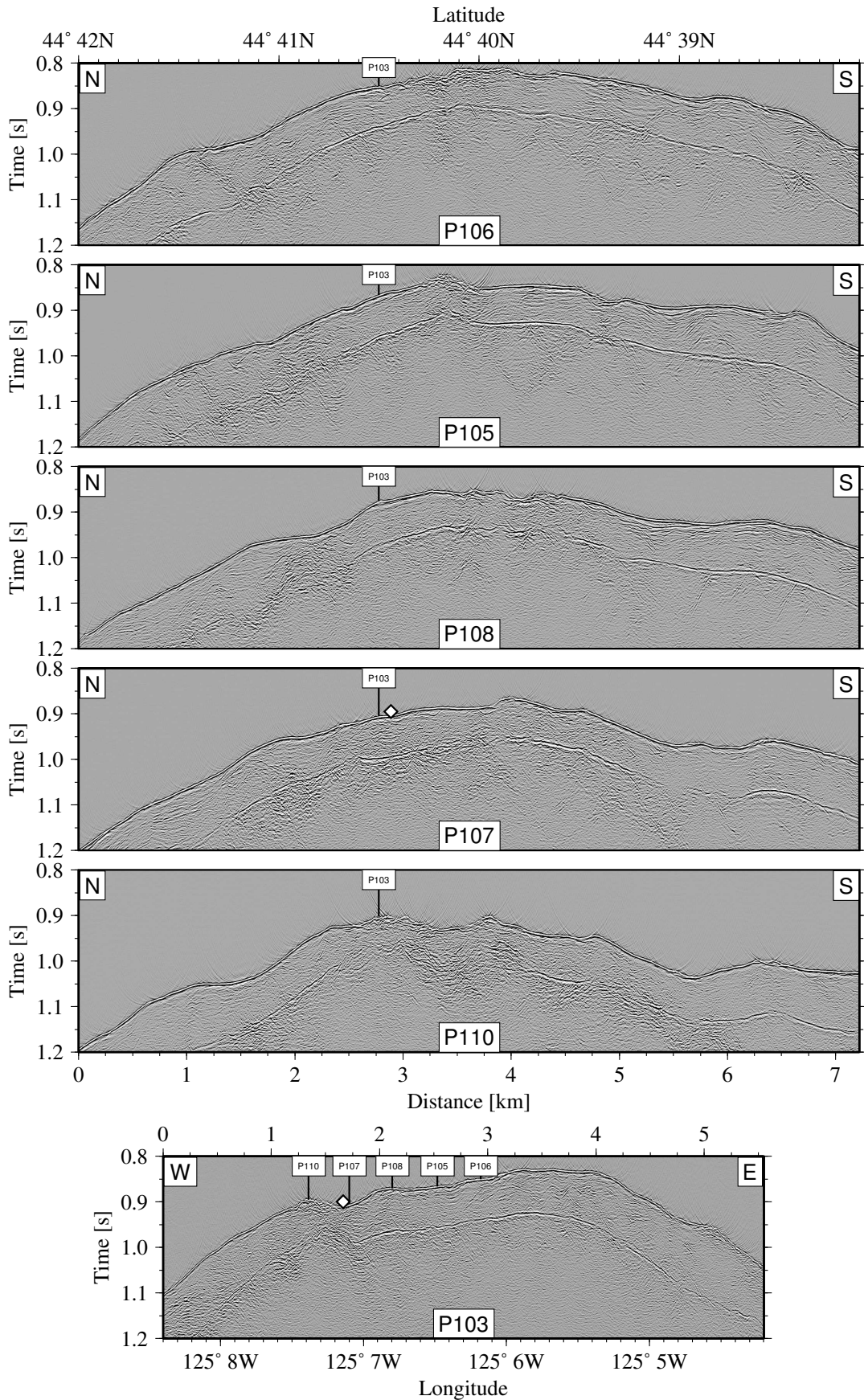


Figure 3.8: Selected SCS profiles after frequency and swell-filtering, trace interpolation and time migration with a constant velocity of 1480m/s, source: GI-Gun. White rhombus marks ODP Site 892.

Chapter 4

Regional SCS data analysis

For a regional seismic study at northern Hydrate Ridge, a total of 25 densely spaced single-channel streamer (SCS) profiles were acquired with the 1.721 GI-Gun across the northern summit. The processing scheme described in Section 3.3 was applied to the SCS data and yielded time-migrated profiles, which were used for an extensive mapping of the area. First, a structural interpretation of some selected profiles is given focusing on the identification and mapping of possible fluid pathways and cold vents. Furthermore, a high frequency Watergun profile, a GI-Gun profile and low frequency MCS data are examined along a profile segment of the main line to illustrate the influence of the source frequency on resolution. Second, the BSR signature and its regional characteristics are examined including heatflow derivation and amplitude interpretation.

4.1 Structural analysis

Six GI-Gun profiles (the east-west running main line 103 and five north-south trending profiles) are displayed together with high-resolution bathymetry in a 3D-perspective view in Figure 4.1; they provide insight into the regional structural setting. The time-migrated seismic sections, which are also shown in greater detail in Figure 3.8, reveal a strong, nearly ubiquitous BSR, marking the transition zone from hydrate to free gas bearing sediments. Along some profiles (e.g., the northern part of P105 and P108, and south of ODP Site 892 along P110) the BSR is dramatically weakened and obscured by diffusive chaotic reflectivity patterns. These features indicate zones of disturbed sediment strata, where unfocused upward flow of gas-rich fluids, destabilized hydrates and shallow free gas can be assumed. By comparison with side-scan sonar data displayed in Figure 4.4 (b), a direct link to backscatter anomalies cannot be established. In addition, smooth sediment cover and no active fluid flow were observed at the disturbed part of P110 on a TV-grab profile (*Greinert, 1999*). Thus, the methane might be accumulating in the shallow sediments over larger areas of up to 1 km rather than reaching the sea floor, due to insufficient local concentrations or missing pathways. The BSR is disrupted and offset at several locations (e.g., P105 at $44^{\circ}40.1'N$ and $44^{\circ}39.3'N$, P106 at $44^{\circ}41.2'N$ and P108 at $44^{\circ}39.4'N$). Here, methane-rich fluids are assumed to migrate rapidly upwards along faults, leading to the formation of carbonate chemohermes, hydrate outcrops, bacterial mats and clam fields. Many of these sites were directly correlated to seafloor features by ground-truthing

data, deep-towed video systems and acoustic data obtained during several research cruises in the past. For example, cruises by R/V *Sonne* confirmed that the northern summit is characterized by a massive carbonate boulder complex. They discovered and sampled the *Sonne* chemoherm about 600 m further west (*Herzig et al.*, 1997; *Suess and Bohrmann*, 1997; *Bohrmann et al.*, 2000; *Linke and Suess*, 2001; *Brown et al.*, 1999) which can be clearly identified in the seismic data (P105 at $44^{\circ}40.1'N$). The BSR is significantly deflected upwards indicating that warm methane-rich fluids ascend from below the hydrate stability zone. By destabilizing the existing hydrate reservoir, fluid flow is further enhanced, feeding the build-up of the chemoherm structure. Massive methane ebullition was confirmed at the summit and at the *Sonne* chemoherm, where plumes of high methane concentrations were measured reaching up to 74.000 nl/l and extending several hundreds of meters into the water column (*Suess et al.*, 1999). By comparison, concentrations of less than 20 nl/l have been found as a background in deep oceans by *Scranton and Brewer* (1978). A third structure, the *Alvin* chemoherm, is located 350 m west of ODP Site 892 at the surface trace of the prominent eastward-dipping thrust fault and was observed and first sampled with the submersible *Alvin* (*Linke et al.*, 1994; *Sample and Reid*, 1998). The gas discharge at these active methane vents seems to be related to pressure changes in a deep gas reservoir being released episodically with up to 1 m/s following tidal periodicity (*Torres et al.*, 2002). *Sample* (1996) has given isotopic evidence for a rapid seismically induced upward fluid flow to the *Alvin* chemoherm originating from depths of greater than 2 km.

A more detailed structural interpretation is possible with the high-frequent Watergun profile and is discussed in the following. The influence of the source frequency on the imaging result is illustrated in Figure 4.2, which shows the same segment of the east-west trending main profile for three different source-receiver configurations. All profiles are time-migrated; the processing scheme for the SCS data described in Section 3.3 was applied to the Watergun and GI-Gun profile. Reflection coefficients are displayed for the seafloor (above seismic) and the BSR (below seismic). The seafloor reflection coefficients have been derived from the amplitude ratio of the seafloor and the first multiple. The same scaling factor was applied to obtain the reflection coefficient at the BSR. Consequently, geometrical spreading, attenuation and effects of the BSR interface have not been taken into account. A more detailed discussion of the lateral variation of the reflection coefficients is given in Section 6.2. The top section represents a part of the MCS line OR89-09 shot with a tuned airgun array (*MacKay et al.*, 1992) containing low frequencies with a center frequency of ~ 36 Hz. The GI-Gun SCS profile 142 in the middle comprises frequencies of up to 350 Hz with a main frequency of 130 Hz, whereas the highest-frequency Watergun SCS section from profile 141 at the bottom has a center frequency of about 550 Hz. Comparison of the sections illustrates the frequency-dependent character of the reflections. In the low frequency MCS section, the BSR looks rather continuous with a major breakdown in reflection amplitude west of OBH 57. The sedimentary structures are poorly imaged; the main landward-dipping thrust fault appears homogeneously as a single reflection event. The GI-Gun with a vertical resolution of about 3 m allows a much more detailed look at the sediments, e.g., the major thrust fault reveals now a multi-layered internal structure. Also, the seaward-dipping fault at OBH 57 is imaged in much greater detail and some weak internal reflection patterns between seafloor and BSR can be observed.

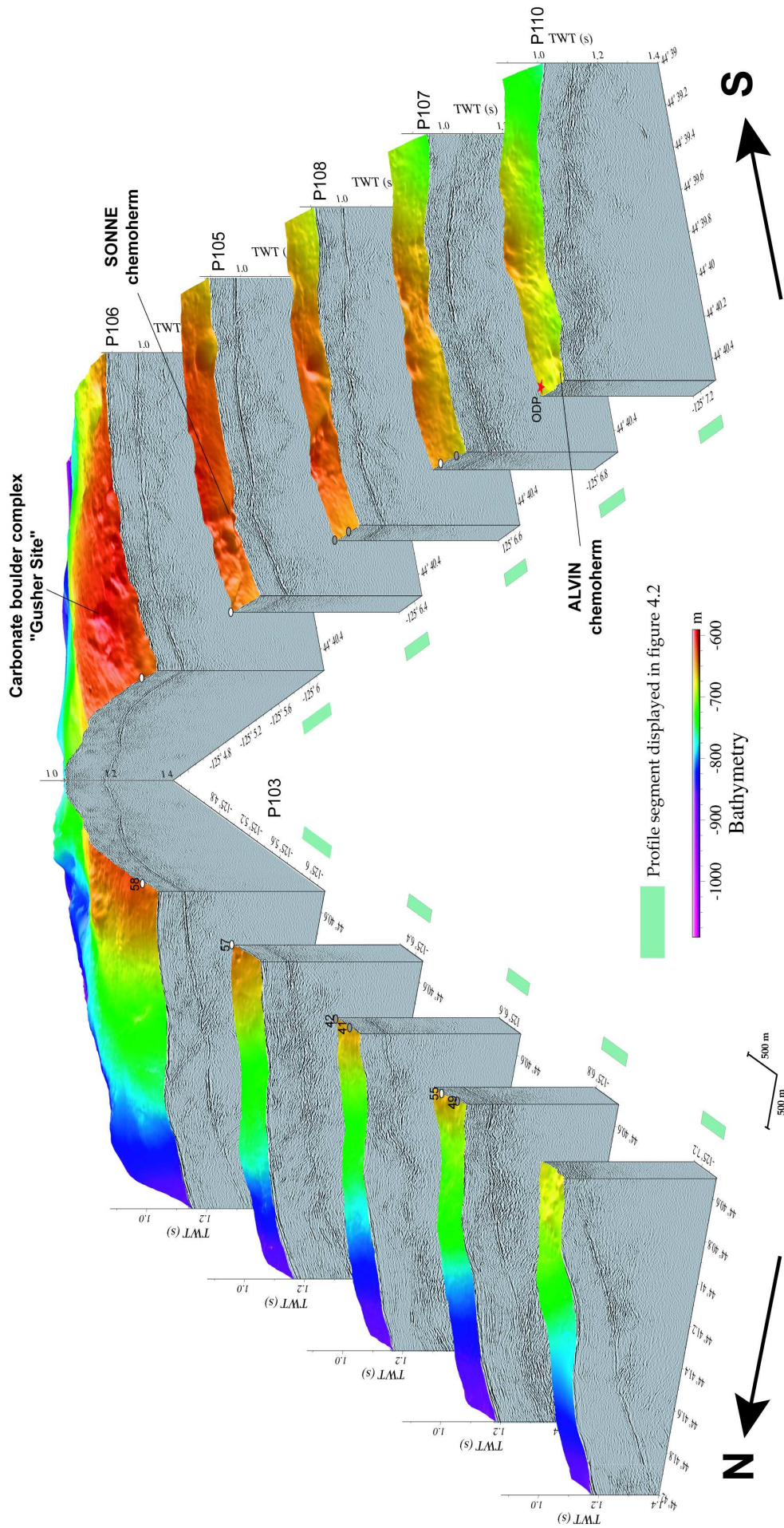


Figure 4.1: Bathymetry map of northern Hydrate Ridge plotted together with time-migrated Single Channel Streamer (SCS) lines shot with a 105 cubic inch GI-Gun during SO150 HYDGAS. The resolution of the bathymetric grid is 0.2 seconds. ODP Site 892 is marked as a red star and was drilled during ODP Leg 146 in 675 m water depth (Westbrook et al., 1994).

The BSR signature reveals small structural variations and discontinuities along the BSR, which reflect lateral changes in the hydrate-free gas properties. West of OBH 57, the BSR can be well traced through the sediment with an amplitude only slightly decreased, thus much different than in the MCS section. The Watergun source yields the most detailed image resolving features of only tenth of centimeters in size. The upper 15 m, i.e. ~ 20 ms two-way-time (TWT), of the sediments below instruments 41 and 42 show a distinct reflectivity pattern and can be clearly distinguished from the underlying sediments. However, structures with a gradual change in elastic properties over a few meters, such as the faults and especially the BSR, yield only small reflection coefficients to the high-frequency seismic waves and are therefore only poorly imaged. Nevertheless, the BSR shows an even more disrupted and lateral variable behaviour compared to the GI-Gun, which clearly indicates that the transition from hydrate to free gas is a gradient of some meters rather than a sharp boundary. Furthermore, the thickness of the gradient zone might vary laterally and influence the observed reflections.

Thus, by comparing the seafloor and BSR reflection coefficients for the three sources the variations resulting from the different prevailing wavelengths, Fresnel zones and interference behaviour are not surprising.

In conclusion, it can be stated that the right target-oriented choice of the source is of immense importance for a successful interpretation. The GI-Gun was shown to be a very good source when investigating gas hydrates because it provides enough energy and low frequencies to image the BSR clearly, but also allows structural interpretations and reliable amplitude analyses without being hampered by small-scale interference effects.

4.2 Regional BSR analysis

For the regional BSR study, a rectangular area of 5.5 km x 7 km was chosen around the summit. The bathymetry was acquired with an EM120 Simrad system on R/V *Sonne* during SO165 (*Pfannkuche et al.*, 2002) and is shown in Fig. 4.3 (a), grid spacing is 0.2'' and about 6 m respectively. The area contains 25 SCS profiles shown as white lines with a spacing of 200-1500 m. Along these profiles, the traveltime and the amplitude of the seafloor reflection and of the BSR have been measured. In the following, the information obtained from the distribution of these BSR characteristics will be discussed.

4.2.1 BSR depth

Since the velocity variations along the main profile are rather small, which will be shown in Chapter 5, it is justified to convert the traveltime data into BSR depth below the seafloor using an average sediment velocity v of 1550 m/s. For example, an error of 20 m/s in average velocity would only lead to a misplacement of the BSR of 1 m for a traveltime of 100 ms.

Hence the BSR depth z_{bsr} was simply obtained by using the equation:

$$z_{bsr} = \frac{1}{2} \cdot v \cdot (t_{bsr} - t_{sf}), \quad (4.1)$$

where t_{bsr} and t_{sf} are the traveltime of the BSR and the seafloor reflection, respectively. The map of the BSR depth distribution is given in Fig. 4.3 (b).

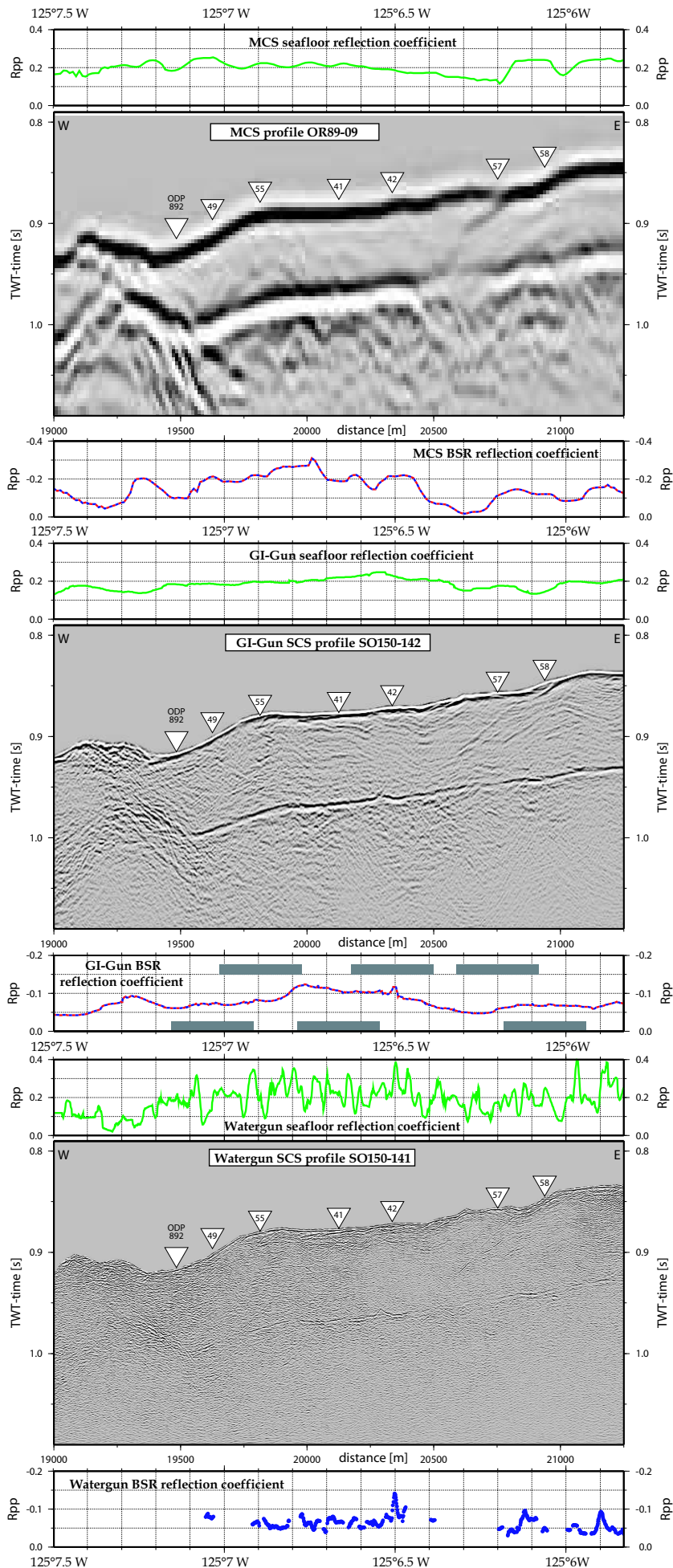


Figure 4.2: Time-migrated profile segment of the main line shot with different sources, displayed with reflection coefficients at the seafloor (above seismic sections) and at the BSR (below seismic sections). Grey areas beneath GI-Gun section illustrate the size of the PP BSR reflection footprint for the particular OBH/S.

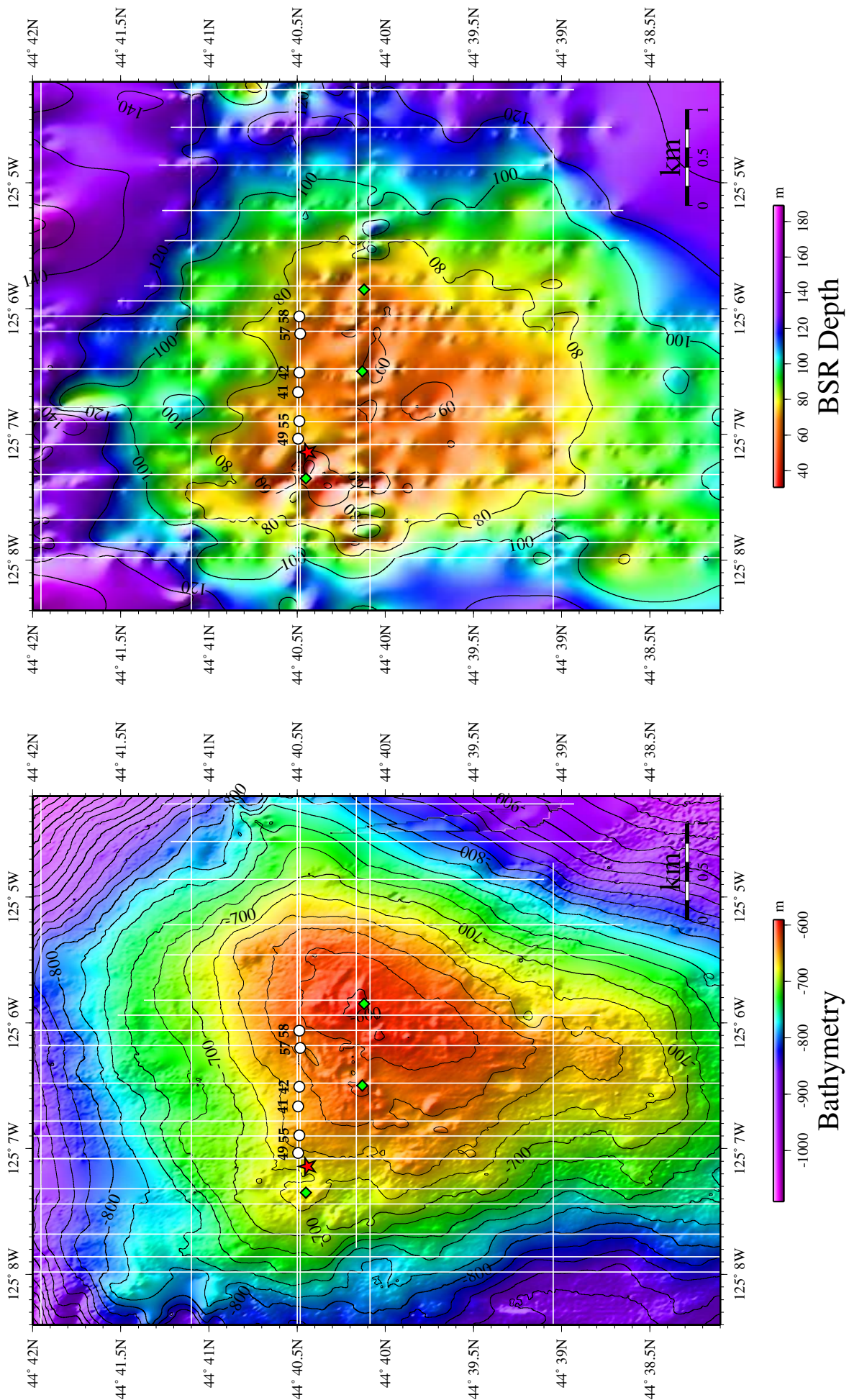


Figure 4.3: Bathymetry grid acquired with a Simrad 120 system on R/V Sonne cruise SO165 in 2002 (a), Distribution of BSR depth below seafloor (b). White lines indicate GI-Gun SCS profiles along which the BSR was analysed. ODP Site 892 is marked as a red star, carbonate structures (see Figure 4.1) are marked as green rhombuses.

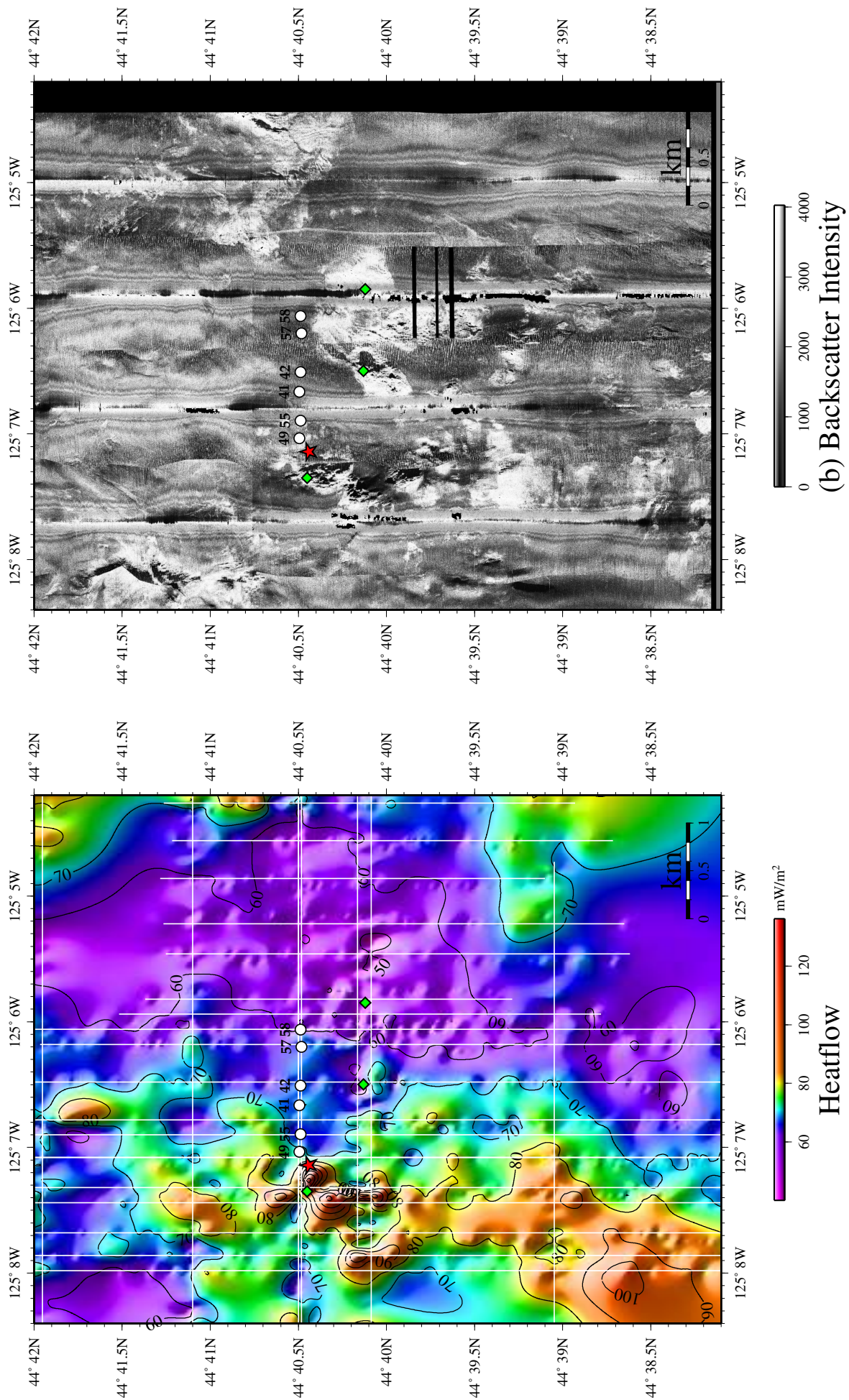


Figure 4.4: Heatflow distribution derived from BSR depth (a), Backscatter intensity from Side-scan sonar survey during SO165 (Klaucke et al., submitted) (b). White lines indicate GI-Gun SCS profiles along which the BSR was analysed. ODP Site 892 is marked as a red star, carbonate structures (see Figure 4.1) are marked as green rhombuses.

Because of the irregular data point spacing of less than 10 m along-track and in some cases over 1 km perpendicular to the profiles, a compromise was chosen by gridding the data every 0.72'' which corresponds to about 20 m. Gridding was accomplished with the *surface* routine provided by the GMT (Generic Mapping Tools) software giving the 'minimum curvature' solution. Due to the irregular coverage, the result of the interpolation scheme for profile-distant locations is not well-constrained and has to be interpreted with caution. In general, the map is reflecting the expected broad correlation between BSR depth and water depth, i.e., decreased hydrostatic pressure due to shallower water depths implies an upward shift of the GHSZ and therefore a shoaling of the BSR.

Looking at the depth distribution in more detail, the BSR isopachs, which mark contours of similar GHSZ thickness, are shifted westward compared to the isobaths of the seafloor, indicating higher thermal activity at the western slope of the ridge. Furthermore, four major regions of an anomalous shallow BSR located west of ODP Site 892, at the northeastern flank and west and southwest of the topographic summit can be identified. These areas are indicative for higher heatflow, which will be investigated in the following section.

4.2.2 Heatflow

A standard method to provide estimates of the thermal structure at continental margins is to use the BSR depth as an isothermic boundary. Local variations in heatflow are likely to reflect focused fluid flow along faults or other structurally controlled pathways (e.g., *Davis et al.*, 1990; *Zwart et al.*, 1996). Crucial parameters are the temperature at the BSR T_{bsr} and at the seafloor T_{sf} and the thermal conductivity k between the BSR and the seafloor. The heatflow q was calculated by assuming linear temperature gradients:

$$q = k \cdot \frac{T_{bsr} - T_{sf}}{z_{bsr}}. \quad (4.2)$$

The temperature at the BSR was derived from the methane hydrate stability condition for a salt water-methane hydrate system described by the following empirical equation after *Dickens and Quinby-Hunt* (1994)(see chapter 1, Fig. 1.2):

$$\frac{1}{T_{bsr}} = 3.79 \cdot 10^{-3} - 2.83 \cdot 10^{-4} \cdot \log P_{bsr}, \quad (4.3)$$

where T_{bsr} is the temperature in °Celsius and P_{bsr} is the pressure in MPa inferred from the BSR depth. To determine P_{bsr} , hydrostatic pressure was assumed since substantial over-pressures at the shallow BSR depth are rather unlikely. The effect of additional lithostatic pressure would lead to a water depth-dependent shift to higher temperatures of a few degrees. On the other hand, BSR temperatures in advective systems may be several degrees cooler than the theoretical values due to capillary effects (*Ruppel*, 1997; *Xu and Ruppel*, 1999). Seafloor temperature was derived from CTD measurements (Figure 4.5). The displayed CTD profile was taken about 12 km west of Hydrate Ridge during cruise SO165 and is representative for the whole Hydrate Ridge area (*Pfannkuche et al.*, 2002).

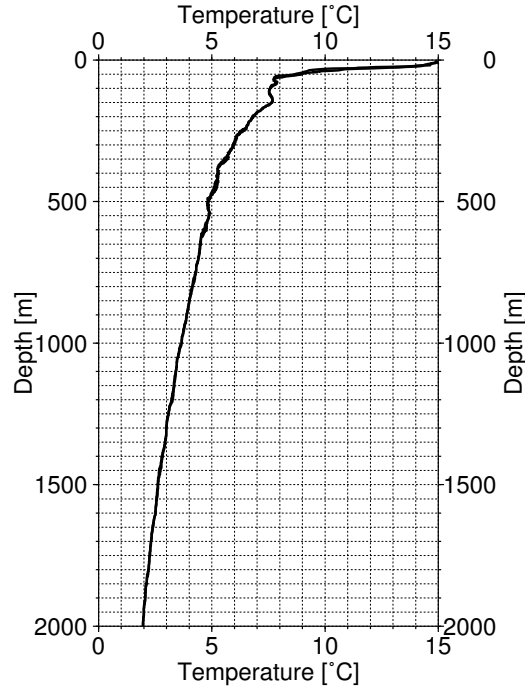


Figure 4.5: *Representative CTD measurement for Hydrate Ridge.*

Thermal conductivity k was determined using the following second-order fit to mean conductivities derived from seismic velocities in the Cascadia accretionary prism (*Davis et al.*, 1990).

$$k = 1.07 + 5.86 \cdot 10^{-4} \cdot z - 3.24 \cdot 10^{-7} \cdot z^2. \quad (4.4)$$

The resulting heatflow is shown in Fig. 4.4 (a), with an estimated overall error of about $\pm 17.5\%$. This error is resulting from the propagation of the errors for the single measurements given in Table 4.1 and has to be regarded just as a rough estimate since absolute accuracies, e.g. of the applied stability model, CTD and conductivity values are difficult to quantify. However, these effects mainly influence the absolute heatflow values and are more or less negligible with respect to relative changes in the thermal structure.

Nevertheless, the deduced heatflow stands in good agreement with results from previ-

measure unit	absolute error	relative error
t_{bsr}, t_{sf}	± 2 ms	$\sim \pm 0.2\%$
v	± 20 m/s	$\sim \pm 1.3\%$
z_{bsr}	± 4 m	$\sim \pm 5\%$
T_{sf}	± 0.2 K	$\sim \pm 5\%$
T_{bsr}	± 1 K	$\sim \pm 10\%$
k	± 0.1 W/m K	$\sim \pm 10\%$
q	± 12 mW/m ²	$\sim \pm 17.5\%$

Table 4.1: *Error estimates for heatflow calculation.*

ous heatflow studies using the BSR depth (*Zwart et al.*, 1996) and ODP drill hole measurements. At Site 892, a value of 78 mW/m^2 determined from the SCS data compares to 71 mW/m^2 obtained from long-term monitoring (*Davis et al.*, 1995). Thus, the results seem to provide representative values of the thermal conditions at Hydrate Ridge.

The heatflow map shows several areas of increased thermal gradients. As already indicated by the BSR depth distribution, the western flank of the northern ridge is characterized by higher heatflow values of more than 80 mW/m^2 compared to about 60 mW/m^2 further east. The north-south alignment of these patterns clearly implies a general dependency on major subduction-related fault structures which, in general, run perpendicular to the direction of accretion. This indicates that, at present, the western slope represents a highly active area, where warm fluids ascend along faults from greater depth due to accretion-caused sediment compaction and dewatering. On the contrary, east of this area, the low heatflow with an absolute minimum of under 50 mW/m^2 near the summit gives evidence for the absence of ascending warm fluids. The massive occurrence of authigenic carbonates, hydrate outcrops and fluid expulsion near the summit might be explained rather with a topographically focused diffusive buoyant lift of methane-rich fluids and methane release through hydrate dissociation in response to tectonic uplift of the ridge than fault-driven fluid migration. However, in times when the thermal regime was more active, extensive carbonate formation might also have taken place along faults which have become recently inactive.

By looking at the heatflow in particular, several anomalous features are apparent. The most prominent high is observed west of ODP Site 892 in the vicinity of the *Alvin* chemoherm. Here, heatflow exceeds 100 mW/m^2 in an area of $\sim 300 \text{ m} \times 800 \text{ m}$ and is well constrained by the dense profile coverage. By comparison with the backscatter intensity map from side-scan sonar data given in Fig. 4.4 (b) (*Klaucke et al.*, submitted) a good correlation to authigenic carbonate chemoherms characterized by high backscatter and an apparent surface roughness can be stated. To the south, the high values of over 80 mW/m^2 also match backscatter features interpreted as carbonates. Looking at the positive anomalies in the south-west and south-east corners and in the northern part of the box, no clear correlation can be seen, but these features are either poorly constrained or oversized due to interpolation effects, or they lie on-track and thus in the shadow zone of the side-scan sonar. At the *Sonne* chemoherm and south of it, the shoaling of the BSR is well preserved as positive local heatflow maxima which again show clear chemoherm-type backscatter anomalies. Remarkable sharp boundaries can be seen at the chemoherms in both the heatflow and the side-scan data. The high heatflow gradients indicate that massive chemoherm formation requires a large focused methane source that is located in greater depth and brings warm fluids rapidly to the surface.

In conclusion, it can be stated that the regional heatflow map derived from the BSR depth gives a reliable picture of the thermal regime at Hydrate Ridge and hence a good link between the observed seafloor features and possible fluid origins.

4.2.3 SCS amplitude analysis

In addition to the structural and thermal properties the SCS data provide information about the regional distribution of the vertical-incidence reflection amplitude. Amplitudes have been measured in the time-migrated sections at the seafloor and at the BSR. They represent a relative measure of the reflection strength given in raw amplitude values and are displayed in Fig. 4.6. Due to variations in source strength, some profiles had to be excluded, leading to a total of 20 SCS lines available for the analysis. The consistency of the derived amplitudes was confirmed by calibration at crossover points and at the mean amplitude values of adjacent profiles. In areas of smooth morphology, the seafloor shows a fairly uniform reflectivity distribution (Fig. 4.6 (a)) ranging from about 35000 to 45000. Only in places of rough topography, where carbonate or hydrate outcrops are known or assumed, the amplitudes are significantly reduced due to scattering and migration effects. This can be nicely seen by comparison with the backscatter map (Fig. 4.4 (b)). However, the transmitted energy should be affected only to a moderate extent. Consequently, the obtained BSR amplitudes shown in Fig. 4.6 (b) yield a reliable measure of the impedance contrast between hydrate- and free gas-containing sediment. The BSR amplitude map shows a patchy reflectivity distribution with three major regions of strong amplitudes (> 35000) east of the ODP Site and south and north of the *Sonne* chemoherm. Amplitudes were only taken into account where the BSR was clearly visible and not interfered by other reflections. These profile segments are marked in the map as white lines. Amplitudes were set to zero at locations along the profiles where the BSR was not visible or strongly disturbed. Hence the deep purple regions in the map indicate the distribution of areas where gas-rich fluids might ascend into the GHSZ. It is not possible to quantify the hydrate and gas concentration on the basis of SCS amplitude data. However, in Chapter 8 the results obtained from AVO modeling of OBS data will be used to calibrate the SCS amplitude and lead to a limited regional estimate of the amounts of hydrate and free gas. So far, only a qualitative assessment is possible, i.e. that stronger impedance contrasts are caused by higher amounts of hydrate or free gas or both. Since hydrate and free gas interact strongly at the phase boundary, it might be suggested that their concentrations are roughly linked. In other words, the positive anomalies might indicate BSR locations where the sediment contains increased concentrations of methane hydrate and free methane.

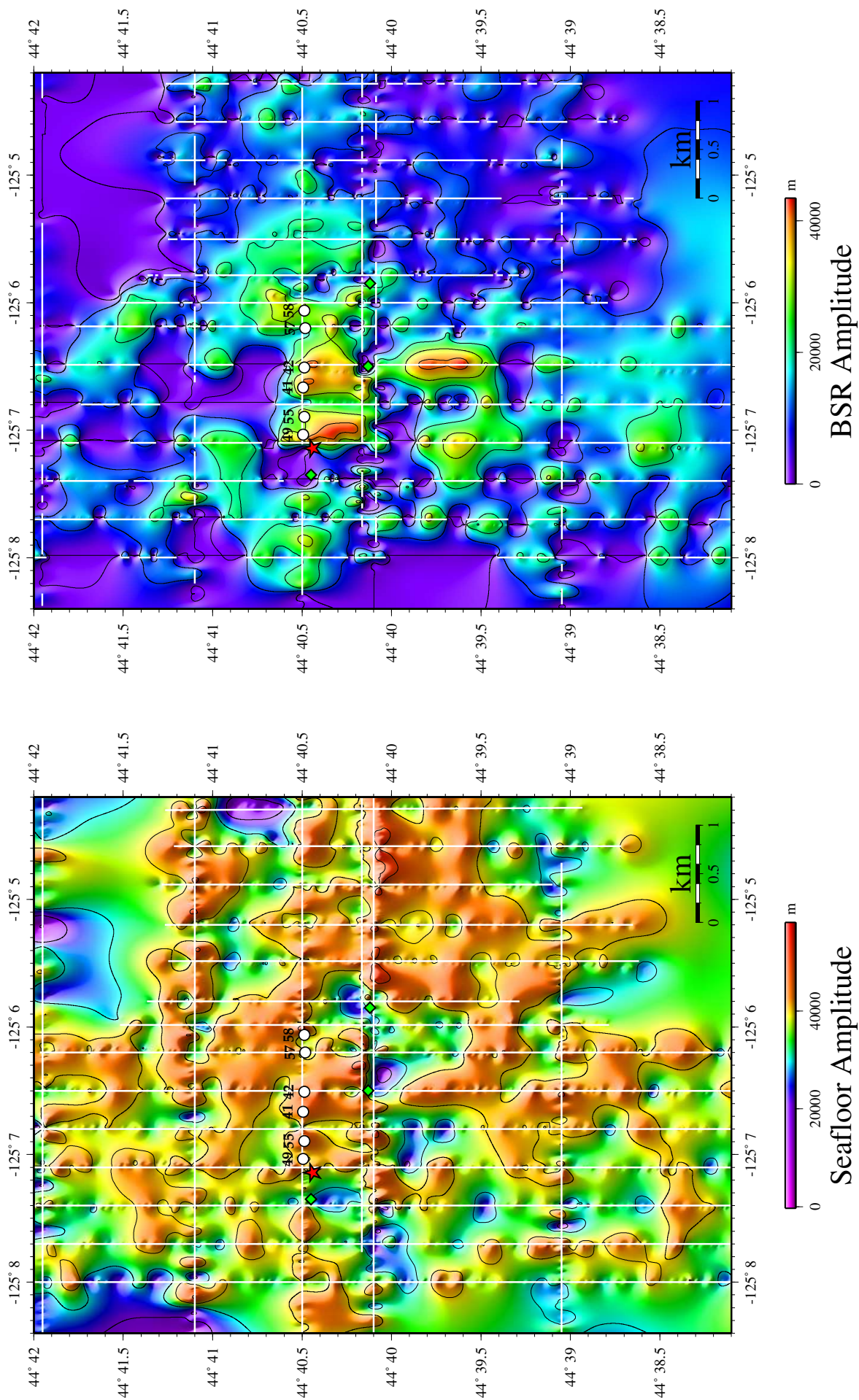


Figure 4.6: Amplitude distribution derived from SCS data for the seafloor (a) and the BSR (b). White lines indicate GI-Gun SCS profiles along which amplitudes were analysed. ODP Site 892 is marked as a red star, carbonate structures (see Figure 4.1) are marked as green rhombuses.

Chapter 5

Velocity analysis

Accurate knowledge of the seismic velocities is crucial for a reliable seismic characterization of hydrate-bearing sediments, because hydrate increases both compressional and shear wave velocities. For this purpose a total of 15 densely spaced OBH/S instruments were deployed along the main E-W running profile at northern Hydrate Ridge (Figure 3.2). The hydrophone P-wave data were input to a 2D traveltime inversion, which yielded a detailed velocity model for the sediments between the seafloor and the BSR. Sonic log and VSP data acquired during ODP leg 146 give further constraints on the velocity profile at ODP Site 892. Further velocity information from prestack depth migration with lower resolution were available from the pre-existing MCS line OR89-09. Additionally, at four OBS stations the average shear wave velocity between the seafloor and the BSR could be determined from shear waves originating from P-S conversion at the BSR.

5.1 Traveltime inversion of OBH/S data

BSR traveltimes were determined from the data of 15 receiver positions, which led to a total of 2684 data picks. These traveltimes were input to the 2D inversion program *rayinvr* (Zelt and Smith, 1992). Since there are no continuous sedimentary reflections above the BSR the starting model consisted only of three layers, the water column, the sediment between the seafloor and the BSR and a sediment layer below the BSR. A constant P-wave velocity in the water of 1.48 km/s was determined from the traveltime of the direct wave during OBH/S data processing (Section 3.2.2) and confirmed by CTD measurements during research cruise SO150 (Klaeschen *et al.*, 2001). The GI-Gun data did not show reflections below the BSR, which left the area of possibly free gas bearing sediments below the BSR unconstrained. A model box of 4 km width centered around OBS 49 proved to be sufficient to account for all data picks during raytracing and inversion. To get a detailed model of the sediment velocities above the BSR, a horizontal node spacing of 30 m was chosen.

A drawback of the *rayinvr* package is that the model parameterization only allows to define a linear velocity gradient for each grid node, i.e. every 30 m, by a top velocity at the seafloor and a bottom velocity at the BSR. Thus, the inversion output has to be interpreted carefully keeping in mind that the obtained velocities are assuming linear vertical velocity gradients and cannot take fine-scaled vertical variations into account.

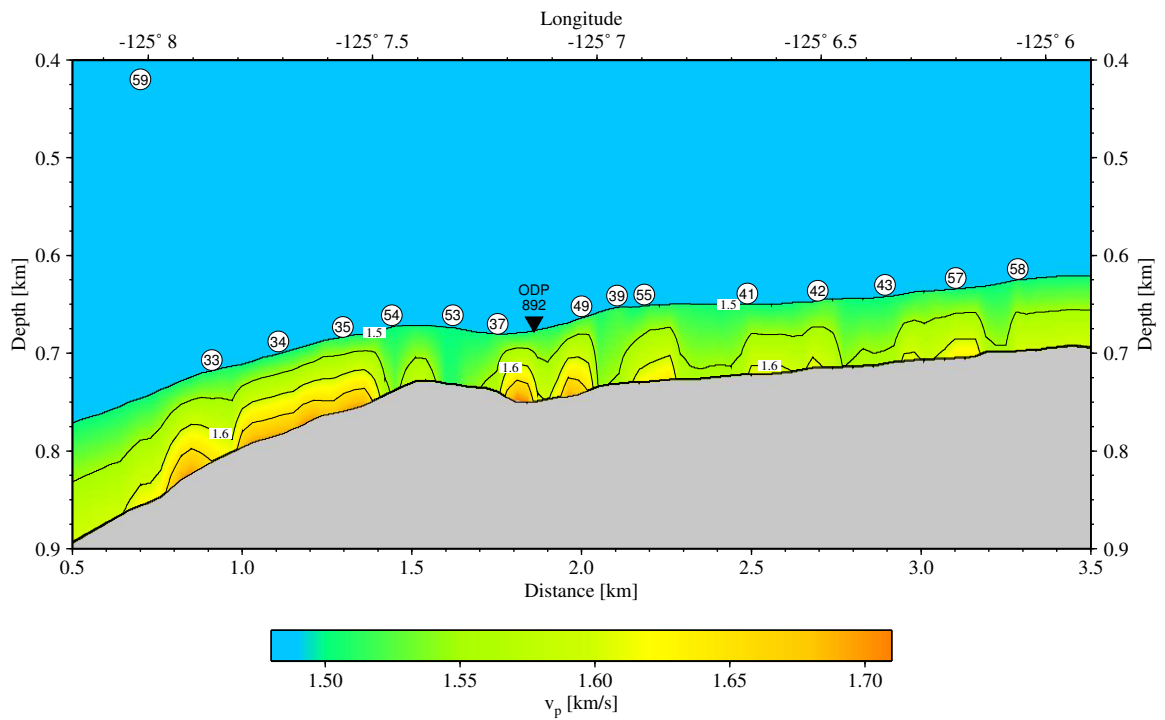


Figure 5.1: *Final P-wave velocity model obtained from rayinvr traveltimes inversion.*

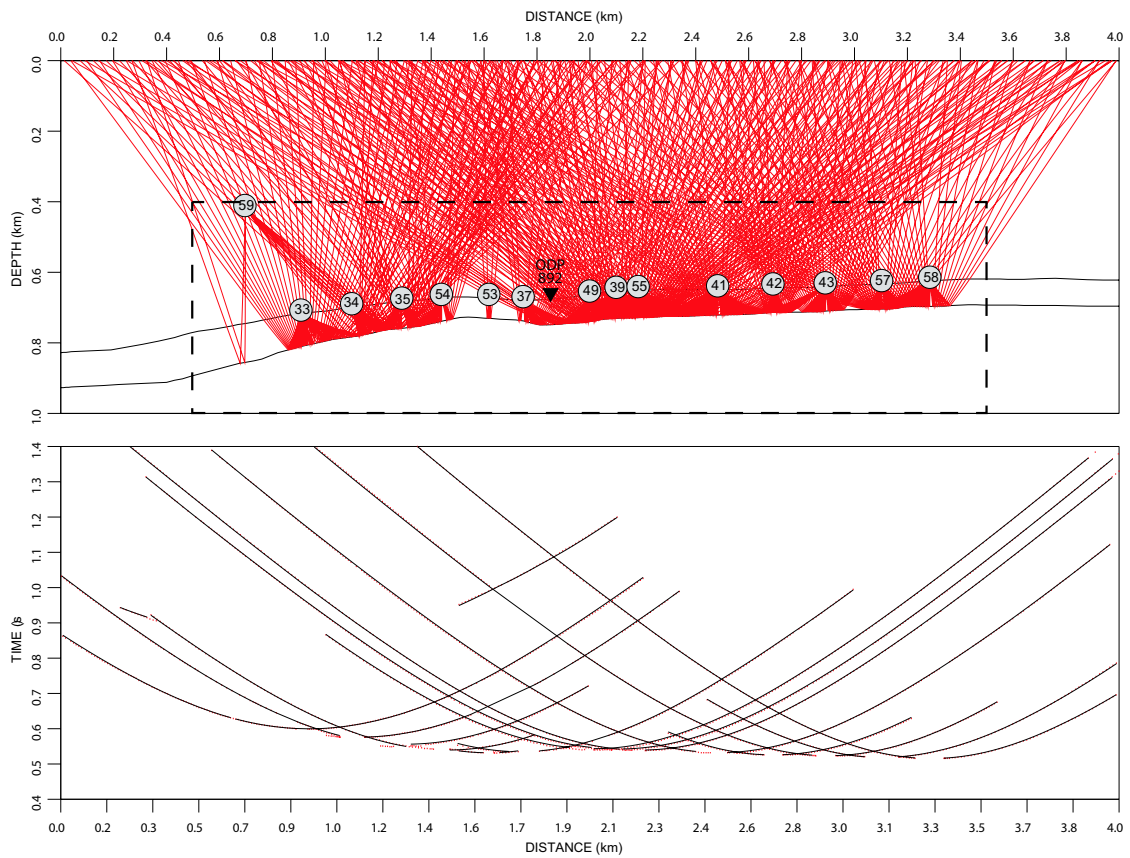


Figure 5.2: *Ray coverage for region modeled with OBS data (top), dashed box indicates extent of P-wave velocity model from Figure 5.1; observed and calculated traveltimes of BSR reflections (bottom), error bars ± 2 ms.*

Nevertheless, the velocity model is capable of reflecting the general lateral velocity variation along the profile. The final traveltime inversion result is shown in Figure 5.1 and will be discussed in detail in Section 5.1.2. The ray coverage with associated traveltime picks and curves is illustrated in Figure 5.2. The BSR was sufficiently sampled from 0.8-3.4 km lateral coordinates, except for the area around OBH 53 (1.5-1.7 km) where, due to the complex reflection pattern of the thrust fault, a BSR could not be clearly identified. In general, the BSR footprints of neighbouring stations overlap, only between stations 42, 43 and 57 small segments of 20-40 m width were not illuminated. Here, the receiver spacing of ~ 200 m was too large and should have been chosen smaller.

5.1.1 Model assessment

In order to establish the reliability of the final model, a model assessment was carried out. First, to illustrate the achieved fit between the observed and the calculated traveltimes, a close-up view of some traces of OBH 55 is shown in Figure 5.3. The picks are plotted as red dots with error bars of ± 2 ms, which correspond to the assumed overall pick uncertainty. Raytracing of the final model results in the traveltimes marked as yellow crosses, which apparently fit the data and lie well within the error bars. One possibility to assess the final model is given by presenting model statistics in the form of final rms and χ^2 measures of the traveltime misfit. The normalized χ^2 value is defined as:

$$\chi^2 = \frac{1}{N} \cdot \sum \left(\frac{t_{obs} - t_{calc}}{\epsilon} \right)^2 \quad (5.1)$$

where N is the number of rays traced, t_{obs} and t_{calc} are the observed and calculated times and ϵ is the assumed pick uncertainty.

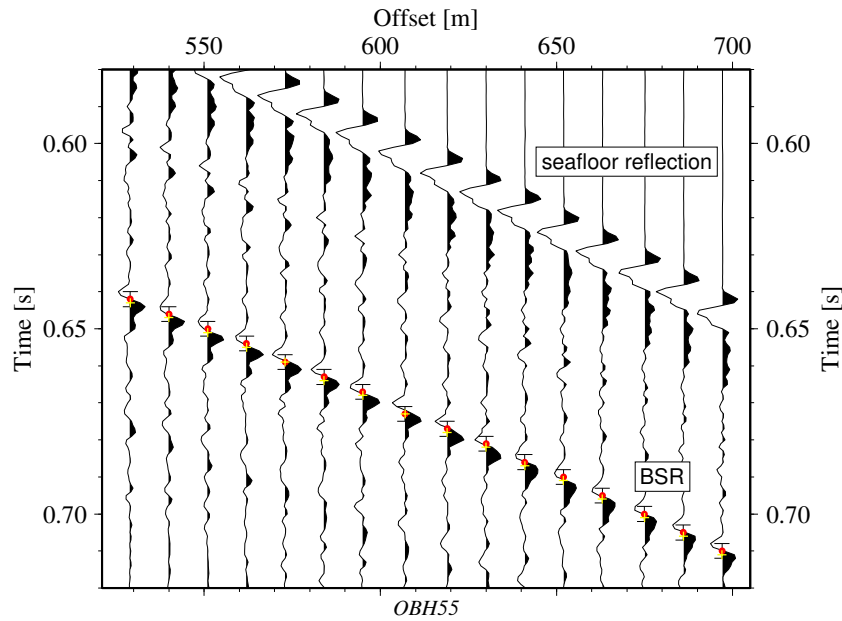


Figure 5.3: Close-up view of data picks (red dots) with error bars of ± 2 ms and of modeled traveltimes (yellow crosses) for the BSR at OBH 55.

A fit can be considered good if χ^2 is equal 1 or less, i.e., all calculated times lie on average within the pick uncertainty window. Obviously the final χ^2 measure is strongly dependent on the chosen pick uncertainty. With the assumed uncertainty of ± 2 ms, an χ^2 measure of less than 1 could be achieved for all receivers. The overall χ^2 value is 0.518 and the rms misfit is less than 2 ms. The detailed model statistics are given in Figure A.1 in the appendix. Although the traveltimes of the BSR could be picked in the seismic sections with an accuracy of 1 ms, i.e. the sampling rate, there are some additional error sources for the overall data pick uncertainty which have to be discussed when assessing the non-uniqueness of the final model.

These are uncertainties in shot and receiver positions, water depth and trigger times which can be assumed to be only in the order of 1-2 ms because the final sections have been checked very thoroughly for consistency (see Chapter 3). Furthermore, the inversion is a 2D process, and therefore it is unable to handle 3D effects. Also, instruments positioned offline will introduce additional errors. As shown in Chapter 3, the instruments are offset from the main line only by some tenth of meters in average. The maximum observed offset, 62 m for OBH 57 (water depth 633 m), introduces a time deviation of ~ 2 ms for the projected zero-offset position. However, with increasing shot offset, these effects will decrease quickly and can be neglected. In conclusion, the overall uncertainty is difficult to quantify, but it may reach values of ± 5 ms.

To illustrate the sensitivity of the final model to model variations, χ^2 values have been derived for a set of models with different velocity gradients and BSR depths assuming different uncertainty values (Figure 5.4). Variation of the gradients was done by shifting the velocities at the BSR by percentages of the original velocity keeping the BSR depth unchanged (left figure). In a second run, the BSR depth was varied with fixed velocities (right figure). If a traveltimes uncertainty of ± 5 ms is assumed, the final model can be varied by as much as $\pm 5\%$ in the velocities or ± 5 m in the BSR depth and the calculated times still yield an overall χ^2 value less than 1. This would imply an uncertainty of ± 80 m/s for a velocity of 1600 m/s which has to be considered as very large. With this assumption,

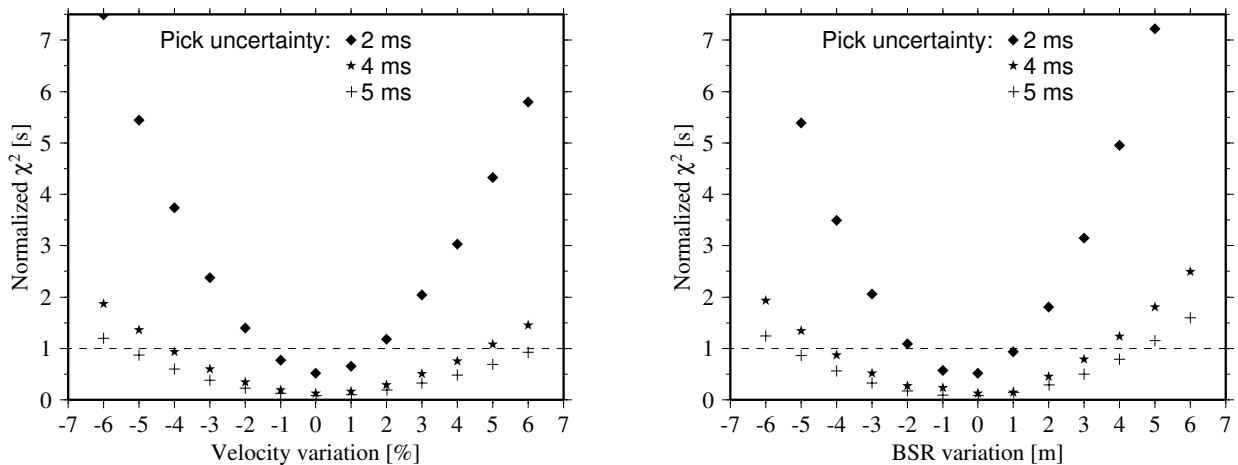


Figure 5.4: Normalized χ^2 values for different velocity models with varying velocities at BSR depth.

a reliable characterization of the sediment velocities is not possible. However, since the above mentioned time errors within the seismic traces are difficult to assess but are likely to be continuously distributed rather than erratic, they may be on average smaller in reality, and the general trend of positive and negative anomalies should have higher accuracy. For this reason and if one considers the investigation depth of less than 80 m, it seems justified to assume a smaller uncertainty of ± 2 ms for the majority of data picks which leads to velocities uncertainties of $\pm 1.5\%$, i.e. ± 25 m/s or BSR depth uncertainties of ± 1 -1.5 m. With these values, the final model is well constrained.

5.1.2 Interpretation of inversion result

In the following, an interpretation of the final traveltime inversion result (Figure 5.1) is given. Velocities range from 1.5 km/s, the predominant value at the seafloor, to a maximum of 1.714 km/s obtained 50 m west of ODP Site 892. The obtained final velocity-depth model contains several velocity anomalies. In order to describe and interpret these in a structural context, the time-migrated seismic SCS profile 142 is displayed together with the velocity field in Figure 5.6. See also the GI-Gun and Watergun seismic sections in Figure 4.2, which show greater structural details due to different amplitude scaling and higher frequency content, respectively. Starting in the west at 0.8 km, higher velocities reaching up to 1.7 km/s at the BSR suddenly decrease to ~ 1.55 km/s at 1.4 km, which can be attributed to the beginning influence of disturbed sediments within the fault outcrop region. Although poorly determined, a seismic indication for gas-rich fluids migrating upward along the fault is given by the further decrease of v_p to 1.5 km/s in the interval below OBH 53. When approaching ODP Site 892 and moving into the hanging wall of the fault complex, velocities at the BSR increase rapidly to over 1.7 km/s. Increased hydrate formation caused by methane entering the undisturbed sediments from the fault conduit could be an explanation for this anomaly.

The velocities decrease to 1.6 km/s east of the drill site, but reach again 1.7 km/s beneath OBS 49. The sudden drop to 1.55 km/s between instruments 49 and 55 might be explained by diffuse sediment reflectivity and a disruption at the BSR permitting upward gas flow (Figure 4.2). Below OBH 55 v_p increases again to 1.64 km/s and may be correlated to hydrated layers or lenses which cause some distinct reflection patterns. Further east, lower velocities of 1.55-1.56 km/s are prevailing until they rise again to 1.6-1.62 km/s at station 41 (2.5 km). A change to softer sediments near the seafloor, which can be seen nicely in the Watergun data, might explain this reduction; and thus, hydrate may still be present in the sediments down to the BSR. Nevertheless, intruding gas may also contribute to this effect because, at 2.3 km, the BSR bends when following the seafloor, changing style in the GI-Gun section and clearly being disrupted in the Watergun data. The elevated velocities beneath OBS 41 and 42 might be associated with increasing velocities in the near-seafloor sediments, but also with higher amounts of hydrate at the BSR. Between 2.75 and 2.95 km a v_p decrease to 1.55-1.56 km/s can be linked to weaker BSR amplitudes in all seismic sections in Figure 4.2, suggesting small amounts of hydrate or upward flow of gas-rich fluids. The ladder is supported by the presence of a seaward-dipping fault running from ~ 2.75 km at the BSR to 3.2 km at the seafloor, which probably acts as a fluid conduit transporting methane rapidly into the shallow sediments and to the seafloor.

In the footwall of the fault below OBH 57, velocities reach again a local maximum of 1.635 km/s, then drop again to 1.56 km/s within a ~ 50 m wide interval at 3.2 km and finally increase to 1.6 km/s below and east of OBH 58. The general increase in velocity below OBH 57 might be connected to the eastward increase in BSR amplitude, and thus, more hydrate in the sediments. Contrarily, the abrupt decrease at 3.2 km is accompanied by a local BSR maximum, which is indicative for higher amounts of free gas. A small disruption seen at the BSR might serve as an explanation, which allows free gas to protrude into the GHSZ and to lower the velocity.

5.2 ODP Site 892 velocity data

Another way to check the quality of the velocity model is given by the available ODP sonic log and VSP data at Site 892. A compilation of the existing velocity profiles at Site 892 is shown in Figure 5.5. The solid black line represents the linear velocity gradient of the final inversion model derived at 1.85 km ranging from 1.5-1.67 km/s. Unfortunately, sonic log data is only available for Hole C in an interval from 35-57 m (blue line, yellow line resampled to 1 m). In general, the log velocities are showing higher velocities increased by up to 70 m/s compared to the OBH/S model. A good fit can be obtained between 50 and 55 mbsf. Keeping in mind that the real velocity distribution is rather non-linear and that the sonic log shows the typical scatter and has only a limited coverage, the correlation can be considered satisfactory.

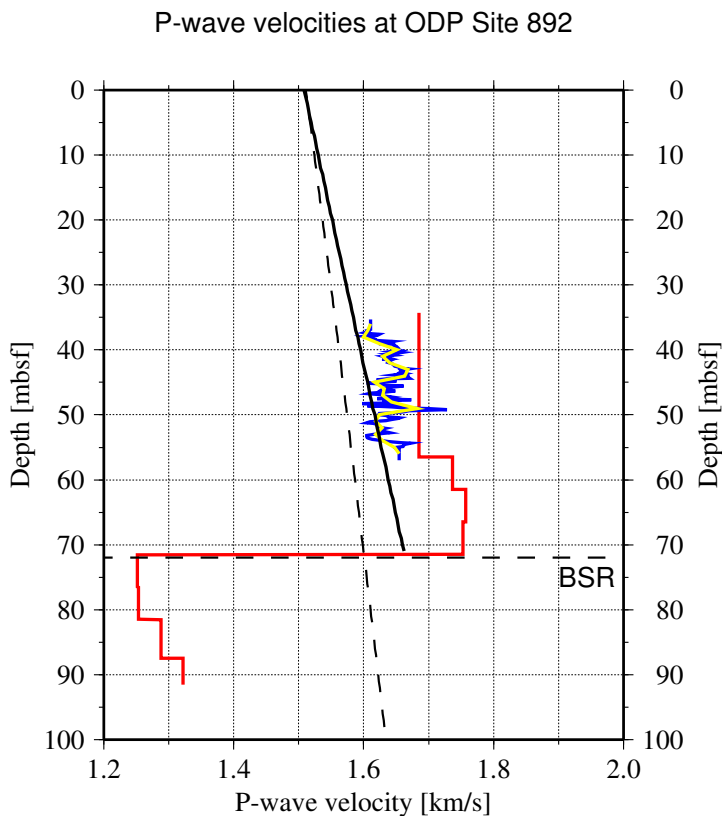


Figure 5.5: *P-wave velocities determined at ODP Site 892: VSP (red), sonic log (original blue, resampled yellow), OBH model (solid black), reference curve for terrigenous sediments (dashed black, Hamilton (1979)).*

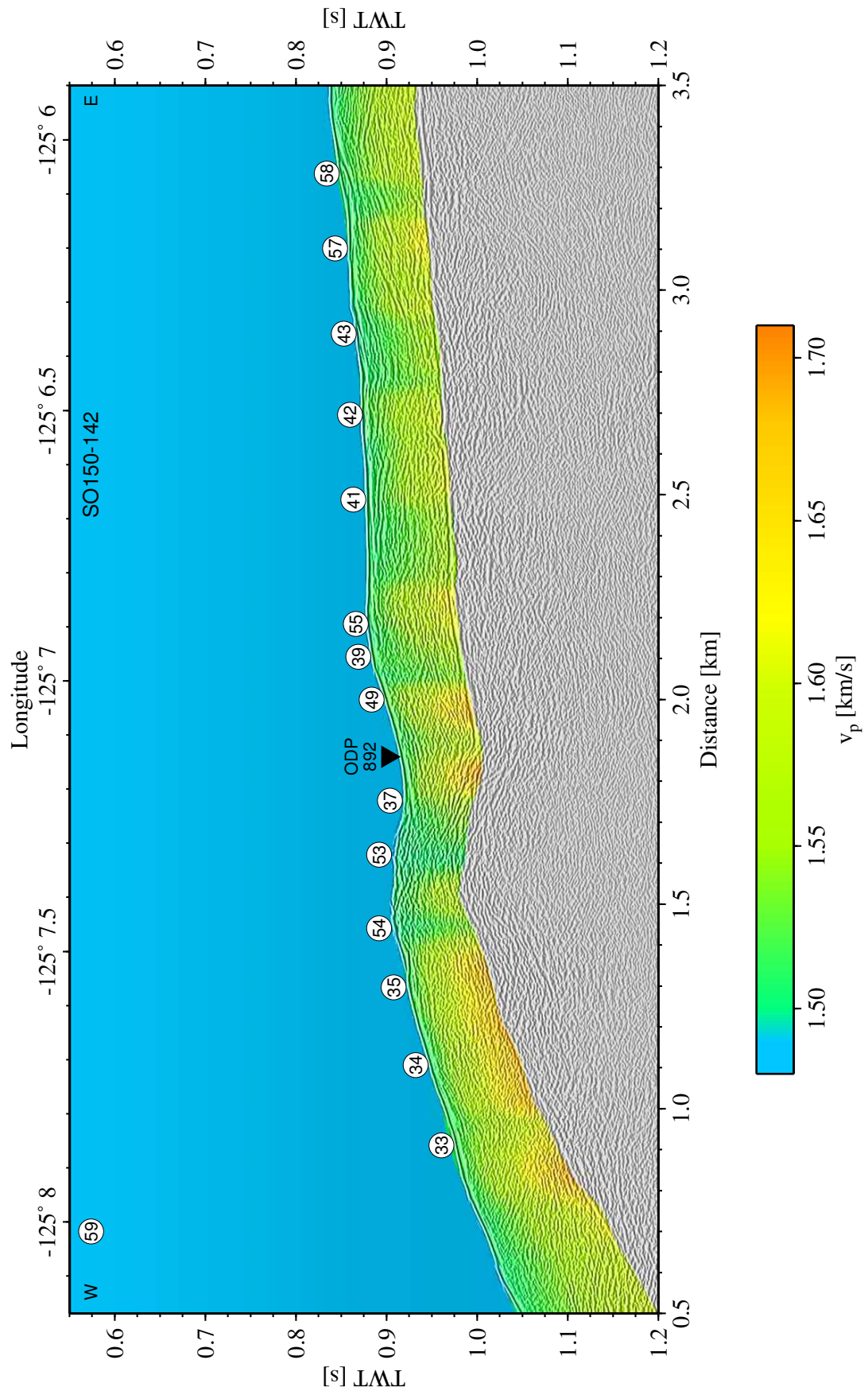


Figure 5.6: Time migrated SCS data of profile 142 overlain by final P-wave velocity model.

Moreover, a better match might not be expectable because the ODP drillholes are located ~ 80 -100 m south of the main OBH/S line.

The VSP velocities (*MacKay et al.*, 1995) displayed as solid red line lie well above the other velocity profiles. Starting with 1.685 km/s at 35 mbsf, they increase to over 1.75 km/s at 57 mbsf, where a lithological contrast in form of a fault has been proposed by *Clenell and Maltman* (1995). These high velocities stand in contradiction with the presented results, but might be explained by the fact that the physical properties are quickly changing laterally in the fault regime area and that even the different drill sites are separated by up to 50 m. As for the sonic log, the same limitations like inversion model resolution, uncertainties in log processing and offline borehole positions are valid when comparing the VSP data to the other data. For comparison, an empirically determined reference velocity profile by *Hamilton* (1979) for terrigenous sediments is shown as dashed line. Velocities increase from 1.511 km/s at the seafloor to 1.6 km/s at a BSR depth of 72 mbsf and thus, are considerably lower than those derived from the Hydrate Ridge data. This indicates that the presence of hydrate is increasing the seismic velocities of the sediment, which correlates well with the hydrate findings at Site 892 (Section 2.2.1).

In addition, the VSP data show a dramatic decrease in v_p down to 1.25 km/s below the BSR caused by free gas in the sediments. The extent of the free gas layer is resolved for at least 20 m and will be further discussed in detail in Chapter 8.

5.3 OR89-09 prestack depth migration

In comparison, the velocity model derived by prestack depth migration of MCS line OR89-09 is shown together with the seismic data in Figure 5.7. Because of the low-frequency of the data (wavelengths of ~ 40 m), the final velocity model cannot resolve the details which are seen in the OBH/S model. However, the main features are visible in the MCS data as well. In the west, velocities are also increased up to 1.7 km/s, in the fault region and around the ODP Site they decrease to values of ~ 1.6 -1.65 km/s and going further east they drop down to 1.55 km/s. In general, the MCS velocities are lower than those derived from traveltimes inversion, but these deviations are not resolvable with the moveout corrections applied to the CDP gathers. Thus, it can be stated that the OBH/OBS model coincides with the MCS model showing a similar general trend in lateral velocity variation.

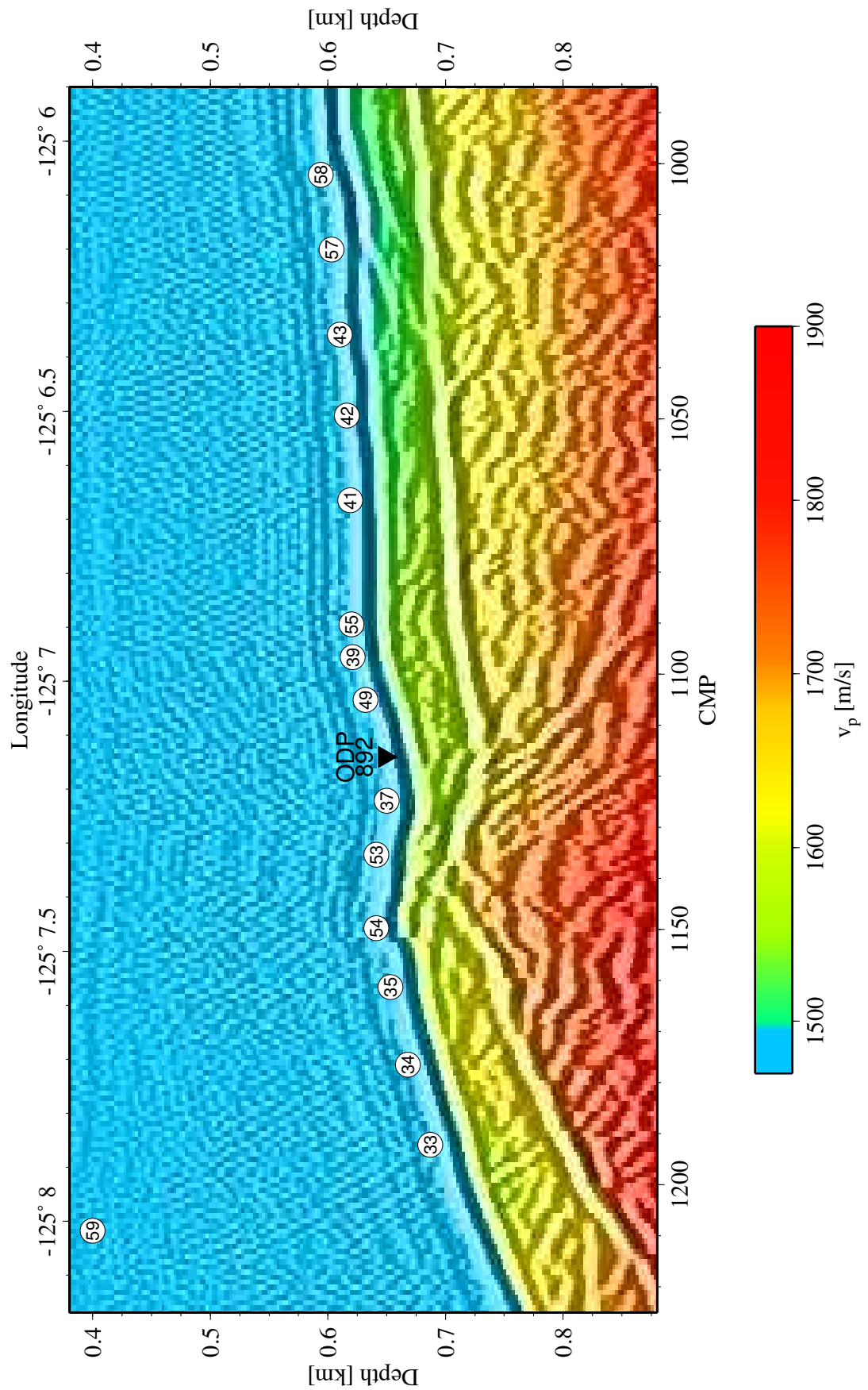


Figure 5.7: Prestack depth migrated MCS data of profile OR89-09 overlain by associated velocity model.

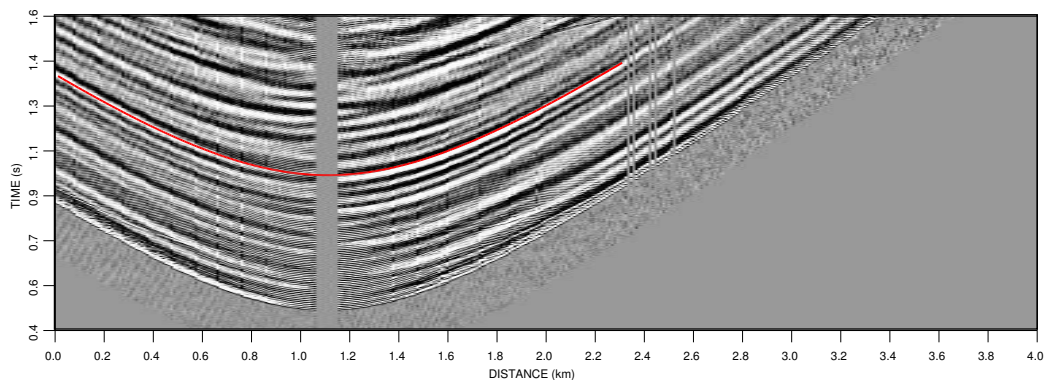
5.4 Shear wave velocities

Although the most significant change in physical properties at the BSR is the decrease in compressional wave velocity caused by free gas, density and shear wave velocity are also altered. Density decreases slightly due to the presence of gas. If hydrate is present in the pore space it will increase the shear strength of the sediment. Depending on its amount and distribution the shear wave velocity will be elevated compared to hydrate-free sediments. Since the shear modulus is not significantly affected by free gas, there should be a sufficient contrast in v_s and ρ for a conversion of P- to S-waves if hydrate is present and stiffening the sediments above the BSR. The radial components of the seismometers (Section 3.2.3) provide the opportunity to investigate the average shear wave velocities between the seafloor and the BSR. A P-S converted BSR phase could be identified in the radial components of four OBS stations which are shown in Figure 5.8. The traveltimes of the converted phase displayed as red lines have been calculated and fitted using the *rayinvr* raytracing routine with the OBH/S P-wave velocity model assuming a constant Poisson ratio σ that is linked to seismic velocities by:

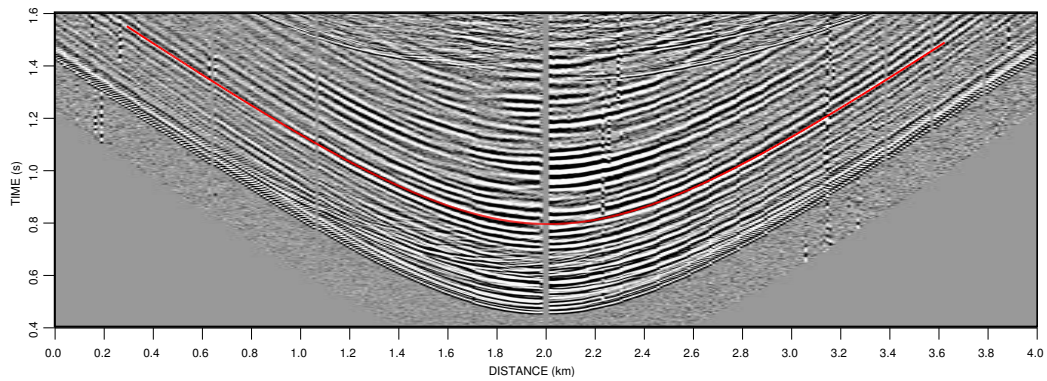
$$\frac{v_p}{v_s} = \sqrt{\frac{1 - \sigma}{0.5 - \sigma}}. \quad (5.2)$$

Because σ is likely to differ for near-surface sediments, hydrated sediments and hydrate-free sediments, the use of a constant σ that fits the data only provides information about the average shear wave velocity. The identification of the BSR converted phase is mainly based on the intensity and continuity of the observed reflections, and especially on their symmetrical presence at larger offsets. The strong reflections observed only in the near-offset do not originate from a continuous interface like the BSR, but rather are produced by point scatter elements only a few meters in width. At OBS 41 and 42 the P-S converted phase can be easily identified and yields σ values of 0.493 and 0.494 respectively, with errors of ± 0.001 resulting in average v_s of 182 ± 13 m/s and 170 ± 14 m/s. For station 49, the identification is hampered by the complex subsurface structure of the fault area. Choosing the first higher energy band seen also at greater offsets results in a Poisson ratio of 0.488.

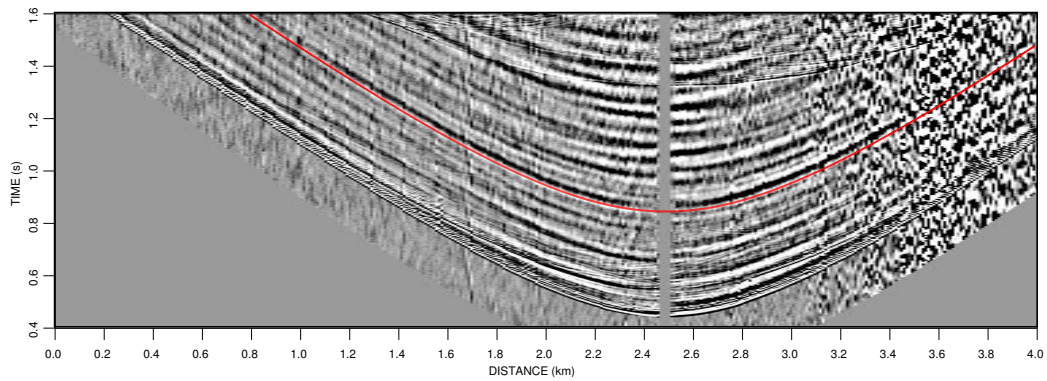
At OBS 34, the dip of seafloor and BSR and possible bad coupling of the seismometer produce a complex reflectivity and make the assignment difficult, but fitting the traveltimes to a stronger reflection seen on both sides yields a σ of 0.494. Because of the aforementioned difficulties, for the two western stations 34 and 49 the interpretation is arguable and therefore an uncertainty for σ of ± 0.002 has been assumed. This leads to average shear wave velocities of 244 ± 20 m/s for OBS 49 and 174 ± 30 m/s for OBS 34. In Figure 5.9, the obtained velocities are plotted together with a reference curve for water-saturated silt-clays and turbidites (*Hamilton, 1976a*) and sonic v_s log data from ODP Leg 204 Site 1245 at southern Hydrate Ridge (*Trehu et al., 2003*). On average, the reference curve shows higher velocities than the OBS data and lies also well above the ODP log data. However, it has to be kept in mind that the average velocity values provide only a limited estimate; the real velocity distribution are likely to be significantly different.



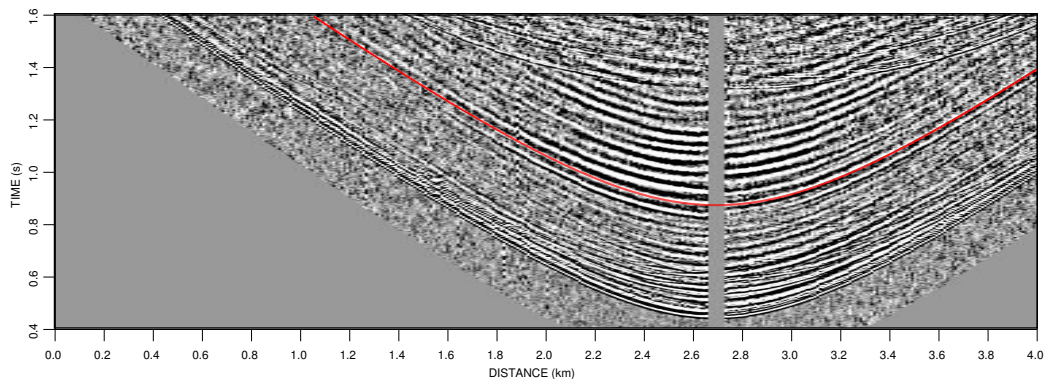
(a) Radial component of OBS 34, $\sigma=0.494$ corresponding to an average v_s of ~ 174 m/s.



(b) Radial component of OBS 49, $\sigma=0.488$ corresponding to an average v_s of ~ 244 m/s.



(c) Radial component of OBS 41, $\sigma=0.493$ corresponding to an average v_s of ~ 182 m/s.



(d) Radial component of OBS 42, $\sigma=0.494$ corresponding to an average v_s of ~ 170 m/s.

Figure 5.8: Radial components of four OBS stations displayed together with calculated ps -converted BSR traveltimes.

Therefore, the final shear velocity profile for OBS 41, which will be obtained later from the amplitude analysis in Section 6.2.2, is displayed as a red curve in Figure 5.9. It yields the same traveltime of the P-S converted phase as the average value of 182 m/s, and the curve is shown to provide an impression of how a more realistic velocity distribution looks in comparison with the average velocity value. The shear wave sonic log measurements at southern Hydrate Ridge start only at 73 mbsf and show velocities which are significantly lower than those obtained from the amplitude analysis. Because hydrate concentrations are believed to be less at the southern ridge compared to the northern area, shear wave velocities should also be lower. With the assumption that velocity gradients are similar to those in the Hamilton curve, the OBS v_s profiles can be easily modified keeping the average value, but ending with velocities below the BSR, which are equal to those measured at southern Hydrate Ridge. Whereas stations 34, 41 and 42 show similar average Poisson ratios of 0.493-0.494, OBS 49 yields a much lower value of 0.488 and thus a significant higher v_s . This might be an additional indicator for an increased hydrate concentration, which is also inferred by the increased v_p velocity in the hanging wall of the main fault. In contrast, the high σ value at the other stations indicates smaller amounts of hydrate in the sedimentary column. At OBS 34 the higher P-wave velocities reaching 1.69 km/s at the BSR are more likely connected to a different structural setting at the western flank of the ridge.

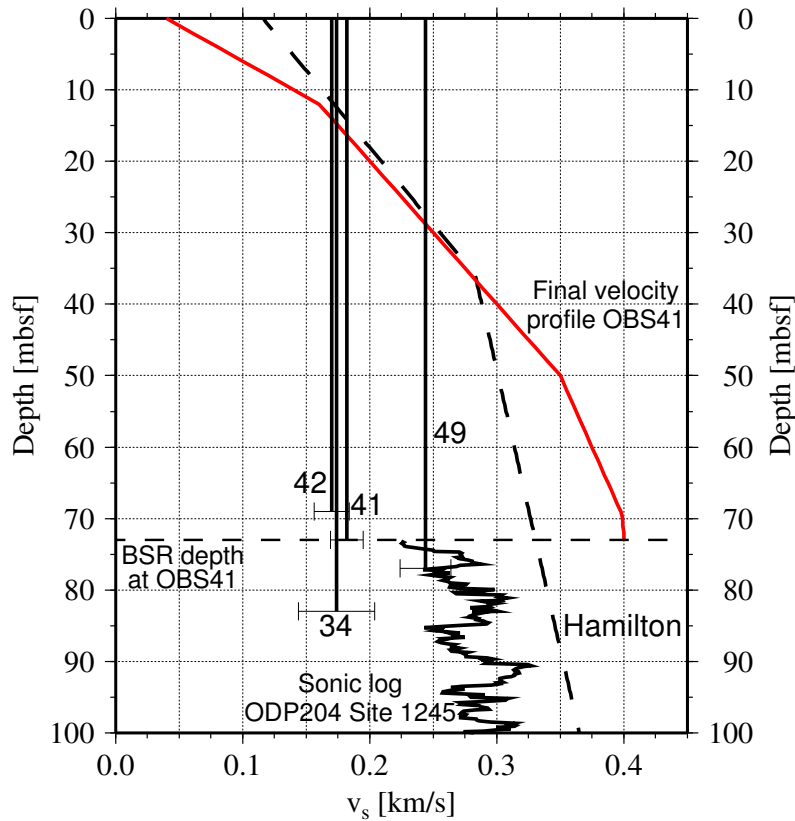


Figure 5.9: Average shear wave velocities determined at four OBS positions displayed together with reference curve from Hamilton (1976a) and sonic v_s log data from ODP204 at southern Hydrate Ridge. Red curve indicates final shear wave velocity profile obtained from amplitude analysis of OBS 41 (Section 6.2.2, Figure 6.15).

Chapter 6

Amplitude analysis

Seismic amplitude interpretation provides important information about the reflector properties that cannot be gleaned from traveltimes alone. Especially in the case of a shallow gas hydrate reservoir given at northern Hydrate Ridge, where velocities beneath the BSR are not constrained by seismic traveltimes, the analysis of the measured amplitudes in the OBH/S and streamer data enables the determination of the elastic parameters at the BSR. In this chapter a detailed amplitude analysis is presented that was performed at the location of OBS 41 and lead to a complete model of the elastic properties. Estimates of the BSR properties along the main line are obtained from an amplitude interpretation of six OBH/S instruments and of the MCS line OR89-09.

6.1 Reflectivity and AVO

When a P-wave strikes an interface at normal incidence, the amplitudes are partitioned into reflected and transmitted P-waves depending on the contrast of seismic impedance Z which is the product of density and P-wave velocity. The reflection coefficient R is the fraction of the reflected amplitude and is given by:

$$R = \frac{A_r}{A_i} = \frac{\rho_2 v_{p2} - \rho_1 v_{p1}}{\rho_2 v_{p2} + \rho_1 v_{p1}} = \frac{Z_2 - Z_1}{Z_2 + Z_1}, \quad (6.1)$$

where A_i and A_r are the amplitudes of the incident and reflected wave. A negative reflection coefficient causes a reversed polarity of the wave reflected from the interface. This is the case at the BSR due to the negative impedance contrast between hydrate-bearing and free gas-bearing sediments.

For nonnormal incidence the situation is more complicated. An incident P-wave generates both reflected and transmitted P- and S-waves (Figure 6.2). The reflection and transmission coefficients depend on the angle of incidence and on the material properties of the two layers. The incidence angles of incoming, reflected and transmitted P- and S-waves follow Snell's law and are inversely related to the layer velocities:

$$p = \frac{\sin \Theta_1}{v_{p1}} = \frac{\sin \Theta_2}{v_{p2}} = \frac{\sin \Phi_1}{v_{s1}} = \frac{\sin \Phi_2}{v_{s2}}, \quad (6.2)$$

where p is the ray parameter. The complete solution for the amplitudes of transmitted and reflected P- and S-waves is given by the Zoeppritz equations (Zoeppritz, 1919; Aki and

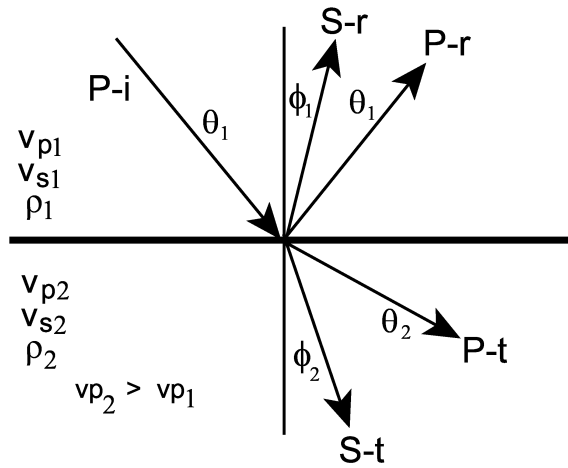


Figure 6.1: Ray paths according to Snell's law.

Richards, 1980; Castagna and Backus, 1993). Although the complete Zoeppritz equations can be evaluated numerically, approximations have been proposed which are often useful and give more insight (Aki and Richards, 1980; Shuey, 1985; Castagna and Backus, 1993). Here, Shuey's approximation for R_{pp} is given:

$$R_{pp} = R_{p0} + B \sin^2 \Theta + C(\tan^2 \Theta - \sin^2 \Theta), \quad (6.3)$$

$$B = A_0 R_{p0} + \frac{\Delta\sigma}{(1 - \sigma)} \quad (6.4)$$

$$C = \frac{\Delta v_p}{2v_p}. \quad (6.5)$$

A_0 specifies the normal, gradual decrease of amplitude with offset. R_{p0} , also called the AVO intercept, is the reflection coefficient for normal incidence. The parameter B is also referred to as the AVO gradient and describes the variation for intermediate offsets, i.e. $15\text{-}30^\circ$, whereas C dominates at far offsets for angles greater than 30° . From the definition of B , one can see that the shear wave velocity in the form of the Poisson ratio contributes significantly to the AVO behaviour. AVO intercept and gradient have been extracted from the CDP gathers of the MCS data and will be discussed in Section 6.4. To illustrate the general AVO behaviour of the reflected PP and PS phases, the solutions of the Zoeppritz equations for input parameters that can be expected at a typical BSR interface are shown in Figure 6.2. Two cases are shown that differ only in the shear wave velocity below the BSR, which is 200 m/s for the black curves and 350 m/s for the red curves. In general, the PP amplitudes show a rapid increase at incidence angles higher than $\sim 30^\circ$ whereas the PS conversion reaches its maximum at 45° . In the case of the large contrast in v_s the PS reflection which is of positive polarity compared to the negative PP reflection is much higher than for the small contrast. A more efficient conversion due to a higher v_s contrast reduces the PP reflection coefficient, which can be seen by the black line shifted downward compared to the red line.

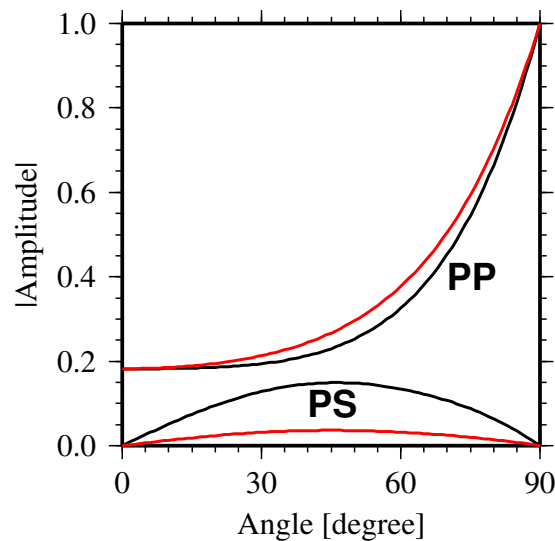


Figure 6.2: Amplitude as a function of incidence angle for a reflected *P*-wave (PP) and a reflected PS-converted wave. Elastic parameters are realistic for a BSR interface: $v_{p1} = 1590$ m/s, $v_{p2} = 1100$ m/s, $\rho_1 = \rho_2 = 1.69$ g/cm³, $v_{s1} = 400$ m/s. Black curves represent $v_{s2} = 200$ m/s and red curves $v_{s2} = 350$ m/s.

6.2 Amplitude analysis at location OBS 41

A detailed amplitude analysis was performed at the location of OBS 41 and is presented in the following. It was the only instrument with sufficient data quality for an AVO processing and interpretation of P-S converted reflections. Since the hydrophone data suffer from severe overamplification, the data of the radial and vertical seismometer component shown in Figure 6.3 were used for the analysis. The seismic phases of interest are marked as PP, i.e. the pure P-wave reflection, and PS, the shear wave phase generated by conversion of the P-wave at the BSR. An illustration of the different raypath geometries of the two phases is given in Figure 6.4. The lateral extent of the area sampled by the reflection, the so-called reflection footprint, differs significantly. Whereas the PP reflection footprint is ~ 450 m wide the PS wave samples a much smaller area of ~ 30 m due to the much smaller shear wave velocity. This has important implications for the AVO interpretation. The AVO curves for the PP phases will reflect all lateral variations in the BSR properties within the footprint region. Thus, they do not allow a detailed interpretation at a specific BSR location, but rather give average qualitative constraints. However, on the other hand, lateral changes can be identified by variations in the AVO behaviour, and due to the wider ray coverage, the reflector of interest can be sampled with larger instrument spacings. In contrast, the PS wave permits a very local and accurate analysis because practically all shear waves have their conversion point nearly directly beneath the instrument. For an area-wide AVO analysis using PS-waves, instrument spacings of less than 20 m would be required, which is impossible unless OBC technology or video-guided OBS deployments are used.

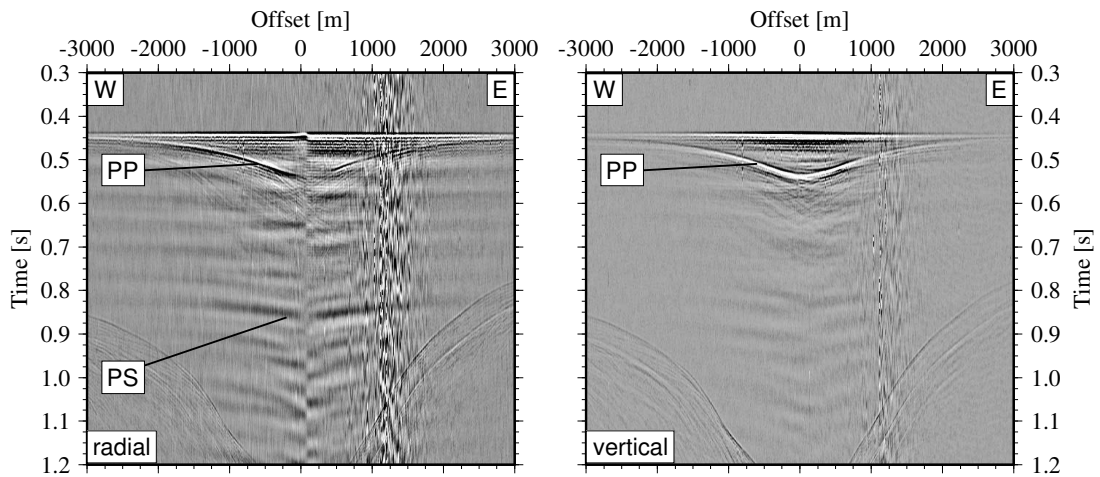


Figure 6.3: *Radial and vertical component of OBS 41 used for amplitude analysis.*

The main approach for the following amplitude analysis is to obtain the elastic parameters at the BSR by fitting synthetic seismograms to the real data. The synthetics were modeled using the reflectivity program OASES (*Schmidt, 1999*), which allows to calculate the viscoelastic wavefield for 1D velocity models. A flow chart of the presented analysis is shown in Figure 6.5. First, the PP BSR phase is analyzed. The velocity model obtained from the traveltime inversion and the density logs of ODP Site 892 provide constraints on the P-wave velocity above the BSR and on the density contrast at the BSR, respectively. Vertical-incidence synthetic seismogram modeling yields information about the P-wave velocity below the BSR, about the quality factor for compressional wave attenuation Q_p and about the structural type of the BSR interface. The S-wave velocity below the BSR is constrained by the shear wave velocity log of ODP Leg 204.

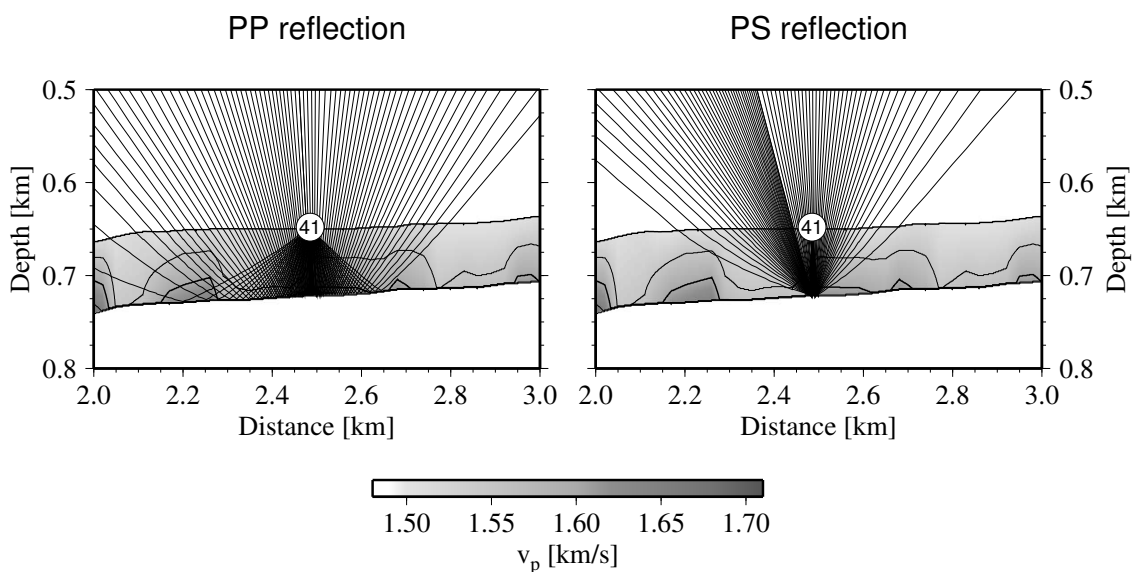


Figure 6.4: *Raypath geometry and footprints of BSR reflections: PP (left), PS (right).*

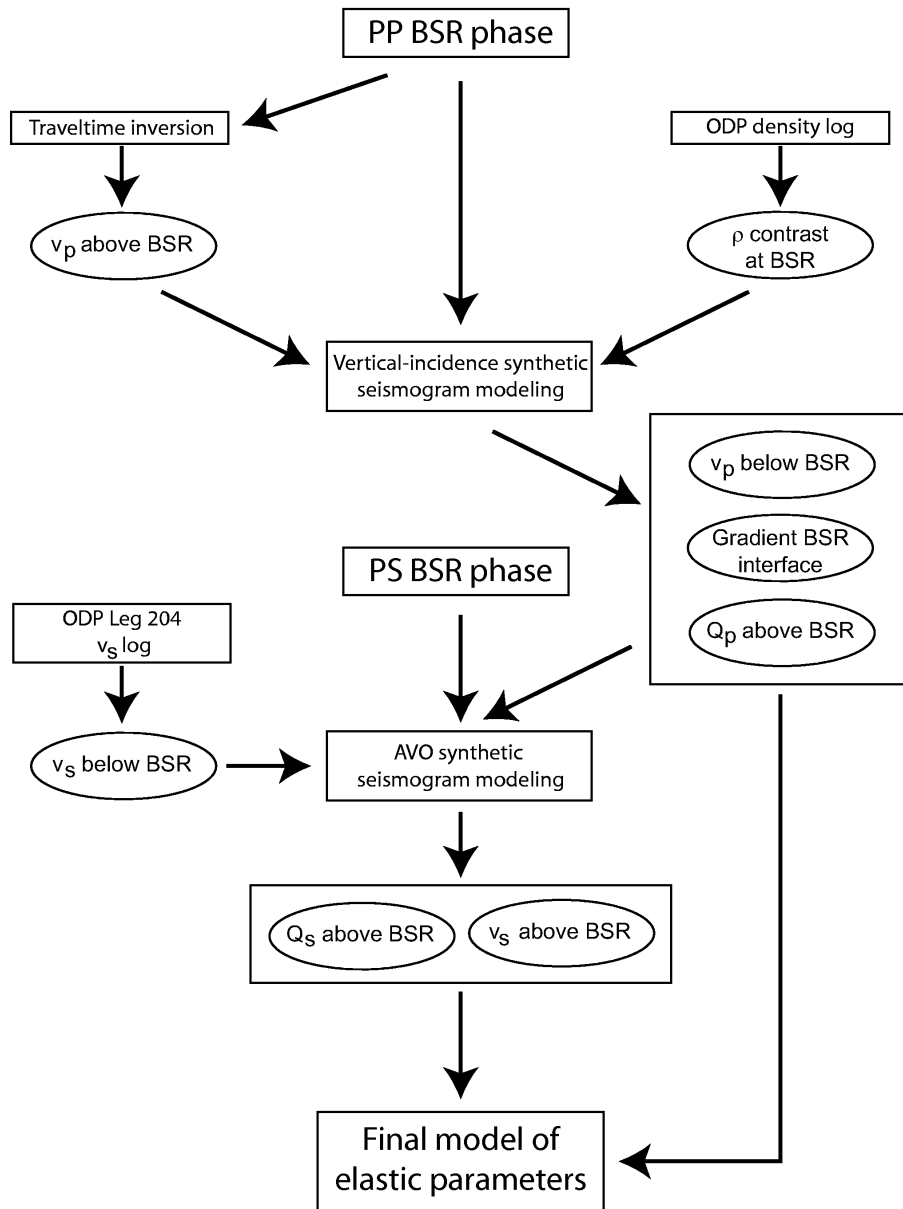


Figure 6.5: Flow chart of amplitude analysis performed at the location of OBS 41.

Using the determined parameters, the PS BSR phase is investigated in detail. The shear wave velocity v_s above the BSR and the quality factor for shear wave attenuation Q_s are obtained from synthetic AVO modeling of the PS phase, leading to a complete model of the elastic parameters at the BSR beneath OBS 41. Rock physics models, which will be discussed in Chapter 7, establish a link of the derived elastic parameters to hydrate and free gas concentrations.

6.2.1 Determination of v_p , ρ and Q_p

The seismic reflection coefficient at the seafloor R_{sf} is used to constrain the seafloor elastic parameters v_p and ρ . R_{sf} is given by the ratio of the amplitude of the seafloor reflection and its multiple for streamer data, and of the direct wave and its multiple for OBH/S data.

To account for geometrical spreading the ratio has to be multiplied by -2 for the streamer and by -3 for the OBH/S data. The reflection coefficients derived for the MCS-array, the GI-Gun and the Watergun sources at OBS 41 are summarized in Table 6.1.

	Watergun	GI-Gun	MCS-Array
R_{sf}	SCS: 0.205 ± 0.02 OBS: 0.214 ± 0.02	SCS: 0.22 ± 0.02 OBS: 0.22 ± 0.02	0.215 ± 0.02
R_{bsr}	SCS: -0.066 ± 0.01 OBS: -0.067 ± 0.01	SCS: -0.107 ± 0.01 OBS: -0.108 ± 0.01	-0.189 ± 0.01
$f_{m,sf}$	550-560 Hz	120-140 Hz	30-40 Hz
$f_{m,bsr}$	420-450 Hz	115-130 Hz	30-40 Hz

Table 6.1: *Reflection coefficients and main frequencies at the seafloor and at the BSR for different sources at OBS 41.*

The seafloor reflection coefficient does not show a strong frequency dependency. A value of 0.22 was assumed in the subsequent studies because the analysis was focused on the GI-Gun data. The lateral variation of R_{sf} along the main line is shown above the seismic sections in Figure 4.2. All amplitudes were picked in the migrated sections and calibrated to 0.22 at the position of OBS 41. Although there are differences in R_{sf} for the different sources, the general seafloor response is consistent for all frequencies. Assuming a seafloor reflection coefficient of 0.22, a P-wave velocity of 1.504 km/s and a density of 1.54 g/cm^3 were chosen at the seafloor. With these parameters, the solution for R_{sf} of the Zoeppritz equations perfectly matches 0.22. Density information was available from ODP drilling and are displayed in Figure 6.6. Since the log data suffered from severe scattering, the data were filtered after excluding density values below 1.5 and above 1.8 g/cm^3 . The density value at the seafloor was taken from the log of Hole A, which is fairly consistent with the reference value of 1.53 g/cm^3 given by *Hamilton (1976b)*. The assumed compressional wave velocity is also consistent with the result from the OBH inversion.

The reflection coefficients at the BSR R_{bsr} plotted beneath the seismic sections in Figure 4.2 were obtained by using the same scaling factor as for the seafloor. Therefore, energy losses due to the seafloor reflection, attenuation and effects of a gradient BSR interface have not been accounted for. Especially attenuation and the structure of the BSR interface play a significant role which can be seen in the frequency-dependent variation of R_{bsr} . In principal, both attenuation and gradient interfaces will affect the amplitudes in a way that higher frequencies yield lower BSR amplitudes. In Table 6.1, the derived values at OBS 41 clearly illustrate this. The R_{bsr} of 0.189 for the low frequency MCS data is the least affected by attenuation and the transition type, and thus it is believed to represent a value close to the absolute reflection coefficient, which would be obtained from the Zoeppritz equations assuming a sharp boundary.

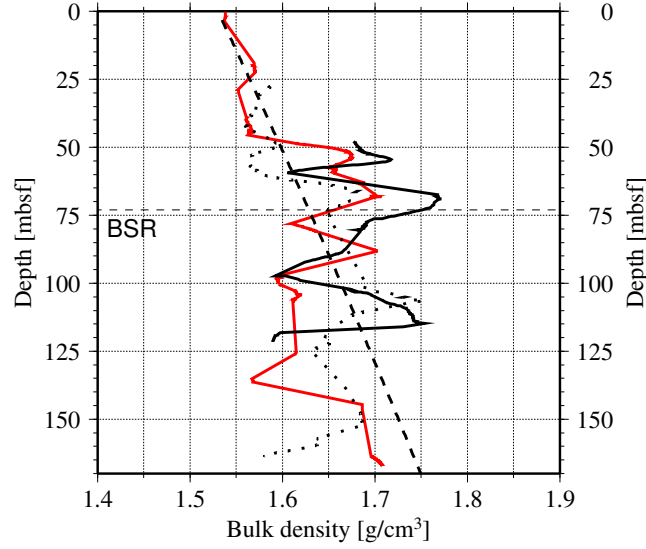


Figure 6.6: *Density logs from ODP Site 892: Hole A (solid red), Hole C (solid black), Hole D (dotted), reference curve (dashed, Hamilton (1976b)).*

P-wave attenuation Q_p

The P-wave attenuation of seismic waves due to the dissipation of acoustic energy into heat can be estimated by:

$$Q_p = \frac{\pi \cdot R}{\lambda \cdot \ln A_0/A_1}, \quad (6.6)$$

where Q_p is the quality factor describing the attenuation, A_0 is the reference amplitude and A_1 is the amplitude of the seismic wave with wavelength λ after traveling the distance R (e.g., *White, 1992; De et al., 1994*). To illustrate the frequency-dependent effect of attenuation on the seismic amplitudes and to determine Q_p from the frequency loss, synthetic seismic traces have been calculated using the model shown in Table 6.2 which is very simple, but fits the conditions at OBS 41 regarding average elastic parameters and BSR depth. Velocities above the BSR were taken from the OBH velocity model, the chosen density contrast is an average estimate from the ODP log data for Holes A and D (Figure 6.6). All density logs show a decrease at the BSR which is consistent with the assumption of free gas with lower density underlying the GHSZ.

The vertical-incident reflection at the BSR interface has been modeled for frequencies similar to those of the MCS-Array, GI-Gun and Watergun sources assuming Q_p values of 0, 100, 150 and 200 and is shown together with the frequency spectrum in Figure 6.7.

Depth [mbsf]	v_p [km/s]	ρ [g/cm ³]
0-36	1.504	1.54
36-73	1.590	1.69
73-	1.130	1.62

Table 6.2: *Parameters for v_p and ρ used for Q_p modeling.*

The reflection coefficients are corrected for geometrical spreading and amplitude loss at the reflection boundaries. No damping yields a R_{bsr} of 0.189 which is consistent with the result from the Zoeppritz equations. The frequency dependence of Q_p is clearly demonstrated by the increasing decrease in R_{bsr} for higher frequencies. Q_p can be estimated to 150 from the loss of higher frequencies in the spectra by comparison with the main frequencies measured at the seafloor and at the BSR from Table 6.1. This average value coincides with other studies for near-surface sediments (*Ayres and Theilen, 2001*). To account for the slight attenuation effect on the low frequency data, the velocity below the BSR in the model given in Table 6.2 has to be modified from 1.13 to 1.1 km/s. The modified impedance contrast yields a reflection coefficient at the BSR of -0.2. Including attenuation with a Q_p of 150, the measured value of -0.189 is obtained, which was determined from the MCS data. Hence, the synthetic reflection coefficient for $Q_p = 150$ changes to -0.160 for the 130 Hz source and to -0.073 for the 550 Hz source.

By comparing the synthetic R_{bsr} with the measured ones in Table 6.1, it is obvious that intrinsic attenuation alone cannot explain the frequency-dependent decrease. The measured GI-Gun reflection coefficient is still much too low, whereas the values for the

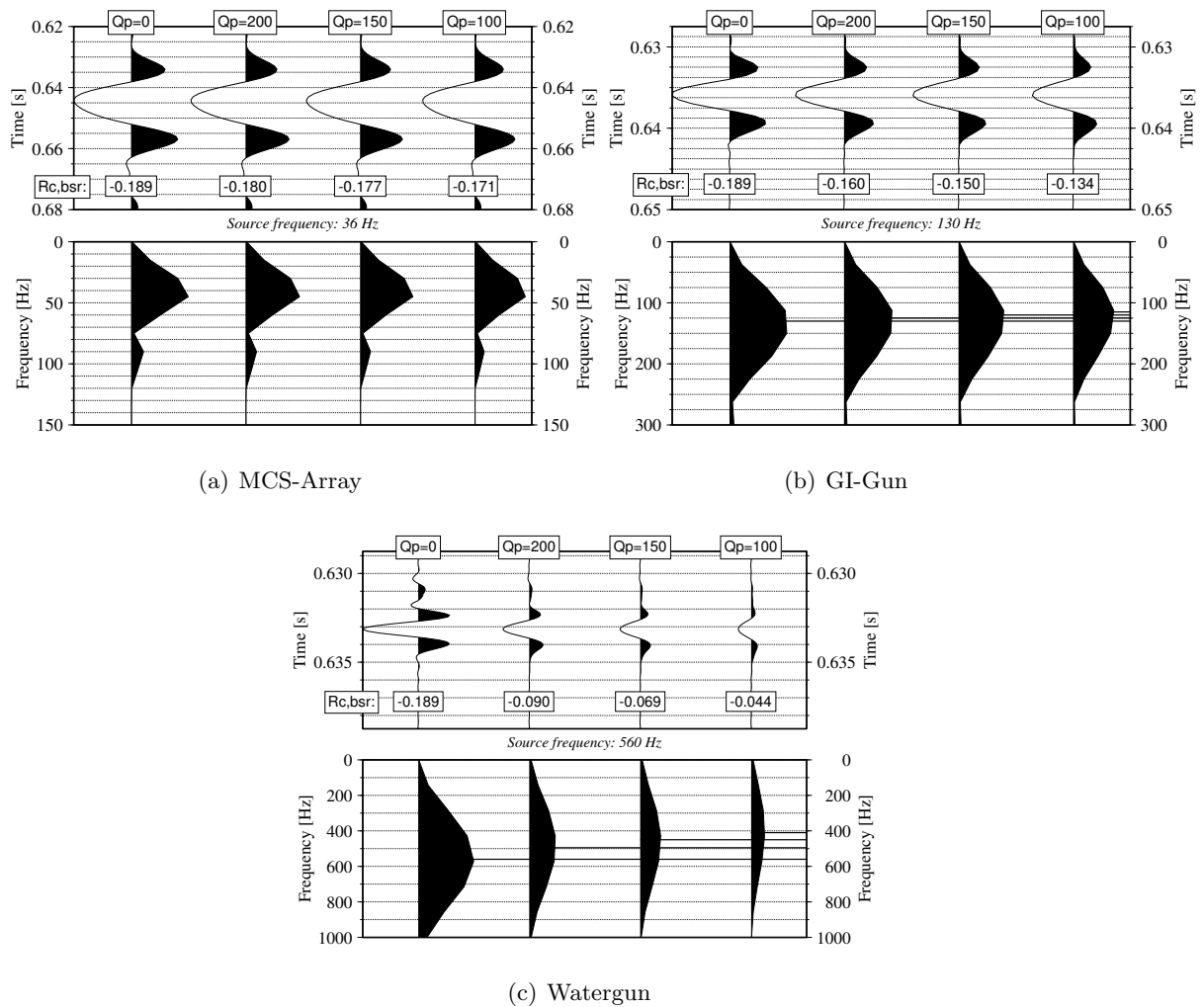


Figure 6.7: Attenuation effect for different source frequencies.

Watergun are roughly in agreement. Since the high frequency waves are much more affected by small-scale variations and thus not as reliable as the GI-Gun data, a model which explains the amplitudes of the ladder has to be found first. The structural type of the BSR transition zone is another important factor controlling the reflection strength, and its effect has to be incorporated.

Gradient BSR interface

Velocity gradients affect reflection amplitudes in a way that the reflection coefficient will start to decrease significantly if the transition zone thickness approaches dimensions of significant portions of the wavelength, i.e. $\frac{\lambda}{8}$ to $\frac{\lambda}{4}$. Richards (1972) has reviewed the dependency of reflection coefficients on transition thicknesses analytically for smooth and linear gradients. In Figure 6.8, it can be seen that a smooth transition is decreasing the amplitudes more efficiently than a linear ramp. A reflection coefficient-versus-frequency analysis was also performed on high-frequent data by Chapman *et al.* (2002) to estimate the transition thickness for a gas hydrate reservoir offshore Vancouver Island. The result is shown in Figure 6.9, and it led to a thickness of 4-8 m in that particular area assuming a smooth velocity model.

To explain the data at OBS 41, the transition zone must decrease the GI-Gun reflection coefficient from -0.2 to -0.148, i.e. by a factor of ~ 1.35 , in order to yield the measured value of -0.108 with included attenuation. The MCS data should be less affected by the gradient layer because the low frequency wave is likely to encounter the interface as a first order discontinuity. According to Richards (1972) this would require a thickness L of approximately 1.4 m for a smooth transition and 2 m for a linear transition. From the study of Chapman *et al.* (2002) a value between 1.5 and 2.5 m can be estimated. However, a detailed derivation for the GI-Gun data is not possible from the published Figures 6.8 and 6.9. Moreover, these studies only take a compressional velocity gradient into account, but consider the density contrast to be zero. Since it can be assumed that if there is a gradational transition in v_p , there is also one in ρ , and in order to have

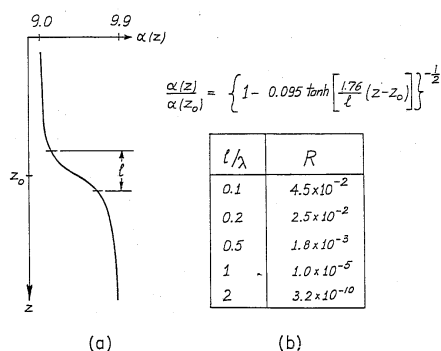


Fig. 1: a) The velocity profile α (km/sec) for a particular EPSTEN layer, shown as a function of depth z .
b) The specific equation of the profile, and a table of values for the reflection coefficient R , calculated as a function of the ratio l/λ .

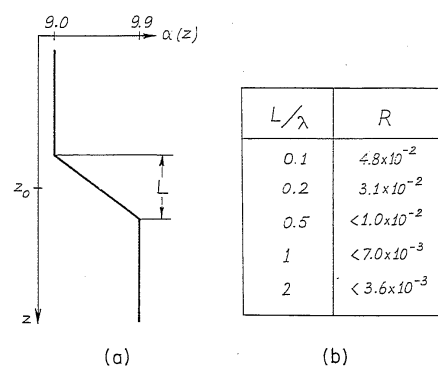


Fig. 2: The velocity profile α (km/sec) for a linear transition between two half-spaces.
b) A table of values for the reflection coefficient R , calculated as a function of the ratio L/λ .

Figure 6.8: Influence of transition thickness on R_c for gradient and linear transitions (Richards, 1972), $R = 5.7 \cdot 10^{-2}$ for $l = 0$.

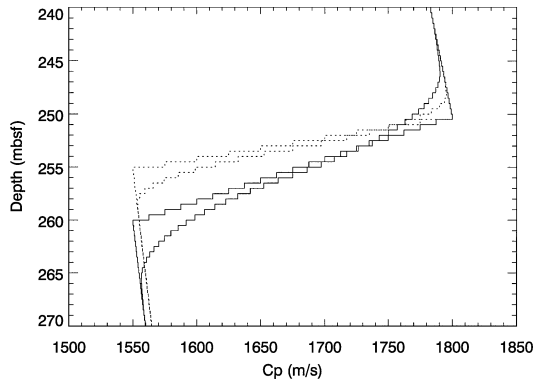


FIG. 7. Velocity versus depth for the sharp and smoothed velocity models for the 5-m (broken line) and the 10-m (solid line) negative gradient layers at the BSR. The velocity gradients in the model were approximated by steps of 0.5 m.

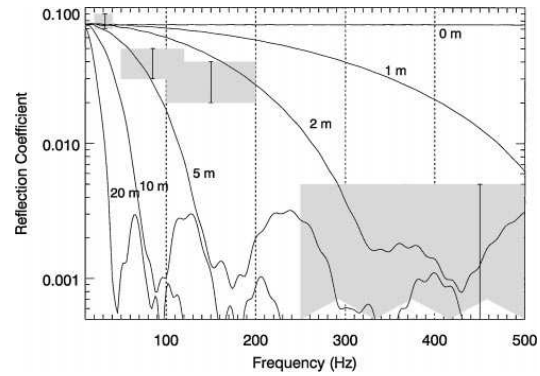


FIG. 9. Normal incidence reflection coefficients versus frequency calculated for the smoothed velocity model for layer thicknesses of the negative velocity gradient layer from 2 to 20 m. The measured reflection coefficients for the BSR data are shown by the shaded rectangles.

Figure 6.9: *Frequency-dependent behaviour of the reflection coefficient for different gradient layer thicknesses (Chapman et al., 2002).*

better constraints for the GI-Gun data, synthetic models were calculated for different linear transitions in v_p only and in both, v_p and ρ . The results are summarized in Table 6.3. Only assuming a gradient in velocity yields a thickness L of 2.2 m, which coincides in principal with the above mentioned studies. By adding a gradational transition in density, higher reflection coefficients are obtained, leading to a required thickness of 2.5 m. The observed differences result from different interference effects, which depend on the prevailing layer thickness.

Transition zone thickness L [m]	R_{bsr} gradient in v_p only	R_{bsr} gradient in v_p and ρ
1.5	-0.138	-0.141
2.0	-0.118	-0.119
2.1	-0.112	-0.115
2.2	-0.107	-0.114
2.3	-0.102	-0.113
2.5	-0.099	-0.109
3.0	-0.082	-0.089

Table 6.3: R_{bsr} for different linear transitions ($Q_p = 150$).

The resulting BSR model with a linear transition of 2.5 m for v_p and ρ is shown in Figure 6.10. A smooth transition at the BSR would reduce the thickness by about 1 m. With the derived model parameters, the reflection coefficient at the BSR for the low frequency data is only slightly reduced to -0.183, but for the high frequency wave it drops down to -0.0085, which is far too low compared to the observed value of -0.066. Thus, the strong BSR in the Watergun data has to be explained by other mechanisms. One possibility might be small-scale variations within the gradient layer which are sufficient to

produce high-frequent reflections, but have no significant influence on the lower frequent waves. A model with a 20 cm interval within the transition zone, in which v_p and ρ decrease suddenly to 1.1 km/s and 1.62 g/cm³, respectively, was capable of producing a reflection coefficient of -0.059, but lowered the GI-Gun reflection coefficient also to -0.07. A more complex type of interference due to small-scale structural variations with several wedges in the centimeter range might be suggested. The possibility of having a layer of gas several meters thick beneath the BSR with a wedge-shaped velocity profile, which would be able to enhance the reflection coefficients for the MCS-Array frequencies, can be ruled out at northern Hydrate Ridge because the accompanying phase shifts can not be observed in the MCS data. Moreover, the VSP measurements show evidence for a low-velocity free gas zone at least 50 m thick (MacKay *et al.*, 1994, 1995).

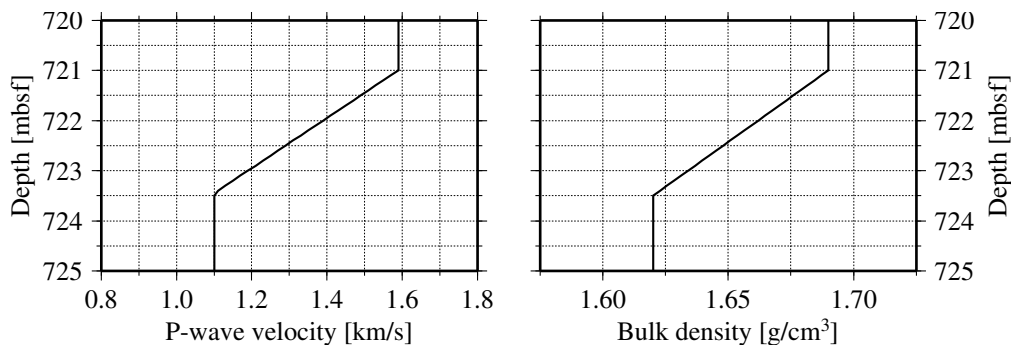


Figure 6.10: *Final model for v_p and ρ assuming a linear transition at the BSR.*

6.2.2 Determination of v_s and Q_s

This section aims at determining the sediment's shear properties beneath OBS 41 from an analysis of the PS-converted waves and, thus, at complementing the elastic parameter model. At first, analogous to the determination of Q_p , the attenuation of the shear waves Q_s is derived from the frequency loss of the PS-converted BSR reflection by comparison with synthetic modeling results. Hereafter, amplitude modeling leads to an estimate of the shear wave velocity contrast at the BSR assuming the linear transition of 2.5 m at the BSR determined earlier.

S-wave attenuation Q_s

In order to constrain the shear wave attenuation, synthetic seismograms have been calculated for different Q_s values and compared to the observed real data. The GI-Gun source wavelet (see Figure 3.1) was used as input wavelet. The input model was taken from the Q_p /gradient analysis complemented by a linear transition of v_s from 390 to 240 m/s. The lower bound of 240 m/s was estimated from the v_s -log available from Hole 1245 of ODP Leg 204 (Figure 5.9). This value represents sediments with small amounts of hydrate, which are assumed to be insufficient to increase the shear strength significantly. Therefore, it is suggested that the log velocities roughly correlate with the shear wave velocities beneath the BSR at the northern ridge. The upper velocity was chosen in such a way that

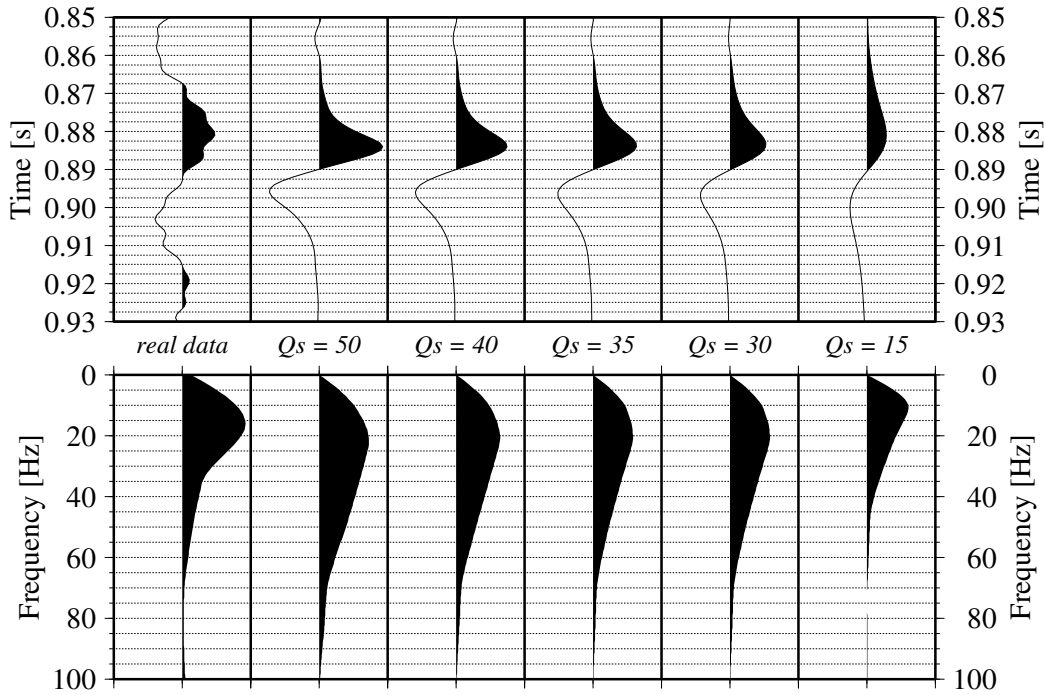


Figure 6.11: *PS-converted wave at 200 m offset, radial component of OBS 41 (left) and reflectivity modeling results assuming different Q_s values for a linear transition of 2.5m width at the BSR with a decrease in v_s from 390 to 240m/s; v_p and ρ are taken from Figure 6.10, $Q_p = 150$.*

a sufficient impedance contrast at the BSR was ensured. In Figure 6.11, the results for Q_s values of 15, 30, 35, 40 and 50 are shown at 200m offset, at which the conversion angle was large enough to produce a sufficient PS phase.

The real P-S converted phase on the left side shows a rather strange blocky appearance, probably due to the low amplification (measured maximum amplitude is 5 for a bandwidth of ± 32768), with a main frequency of ~ 18 Hz. The amplitude decay and the loss of higher frequencies for increasing attenuation values is clearly visible. Because of the waveform differences between synthetic and real data, it is difficult to determine Q_s accurately. When looking at both the waveforms and the frequency spectra, an attenuation value of 35 seems to be appropriate and was selected for the further analysis. The estimated Q_s is by a factor of ~ 4.3 smaller than the derived Q_p value. Thus, attenuation of S-waves in near-surface sediments seems to be much more pronounced than the attenuation of P-waves, which is consistent with results from laboratory measurements (Ayres and Theilen, 2001).

Shear wave velocity v_s

With the now available information about the BSR transition, v_p , ρ , Q_p , Q_s and v_s below the BSR, the only unknown left is v_s above the BSR. In order to determine v_s , several models with different shear wave velocity contrasts at the BSR have been calculated using the OASES reflectivity program. The input models contained similar smooth velocity and density gradients for the sediments between seafloor and BSR. They were adopted

from the OBH velocity data and ODP log data and, in addition, held approximated to the Hamilton reference curves. Below the BSR, the shear wave velocity decreases linearly to 240 m/s within the 2.5 m transition zone. The resulting synthetic seismograms have to be calibrated with the measured seismometer data to ensure a reliable comparison of the amplitudes. For this purpose, the raw amplitudes of the direct wave recorded by the vertical and radial component are particularly suitable and have been picked in the rotated OBS data. In Figure 6.12, the measured amplitudes are displayed together with the synthetic amplitudes. A good match is obtained when multiplying the synthetic amplitudes with a calibration factor of 5200.

Thus, using the same calibration factor for the synthetic amplitudes of the PS phase allows the direct comparison with the measured amplitudes and the determination of v_s . The obtained amplitude distributions are shown in Figure 6.13(a). The shear wave velocity can be estimated to 400 ± 20 m/s. A perfect match of one velocity could not be expected because the conversion angle strongly depends on lateral variations in the P-wave velocity field, which cannot be taken into account by the 1D reflectivity program. Assuming an uncertainty of ± 5 in Q_s leads to variations in v_s of ± 30 m/s. The transition zone at the BSR also has a significant influence in such a way that a thinner transition lowers the derived shear wave velocities; a sharp interface for all elastic parameters yields a v_s of ~ 370 m/s, whereas ~ 380 m/s is obtained for a sharp transition in v_s only. Since v_s below the BSR has been estimated from the southern ridge log data taken in similar depth and the shear strength might vary between north and south due to different consolidation states, the absolute velocity above the BSR has an additional uncertainty of $\sim \pm 50$ m/s. However, the derived velocity contrast of $\sim 160 \pm 50$ m/s clearly indicates the presence of hydrate in the pore space above the BSR.

A synthetic PP BSR AVO curve was computed with the obtained shear wave velocity contrast. A comparison with the measured amplitudes of the vertical component is shown in Figure 6.13(b). The amplitude curves only fit well for the very near offsets, but

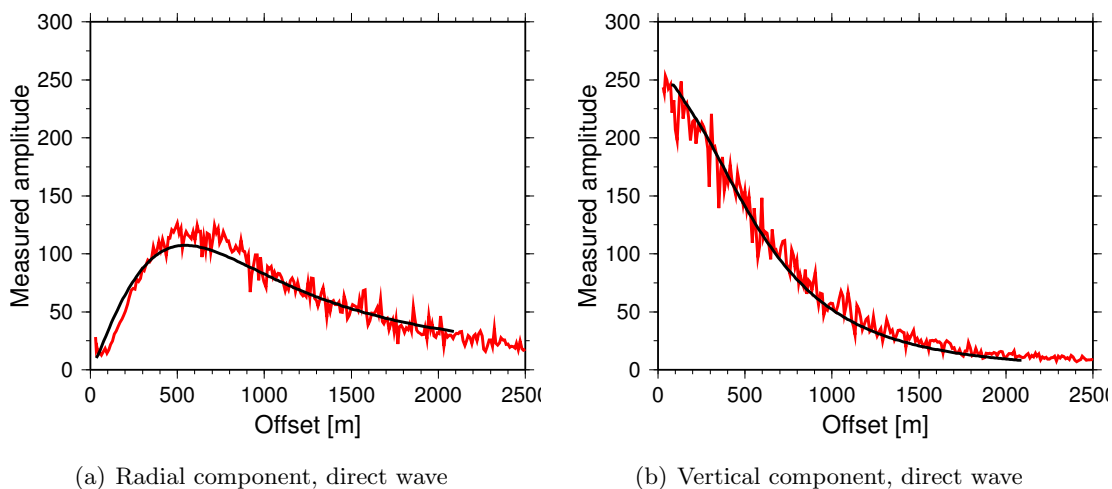


Figure 6.12: *Measured amplitudes of the direct wave: radial and vertical component amplitudes (red lines), synthetic amplitudes multiplied with a calibration factor of 5200 in black.*

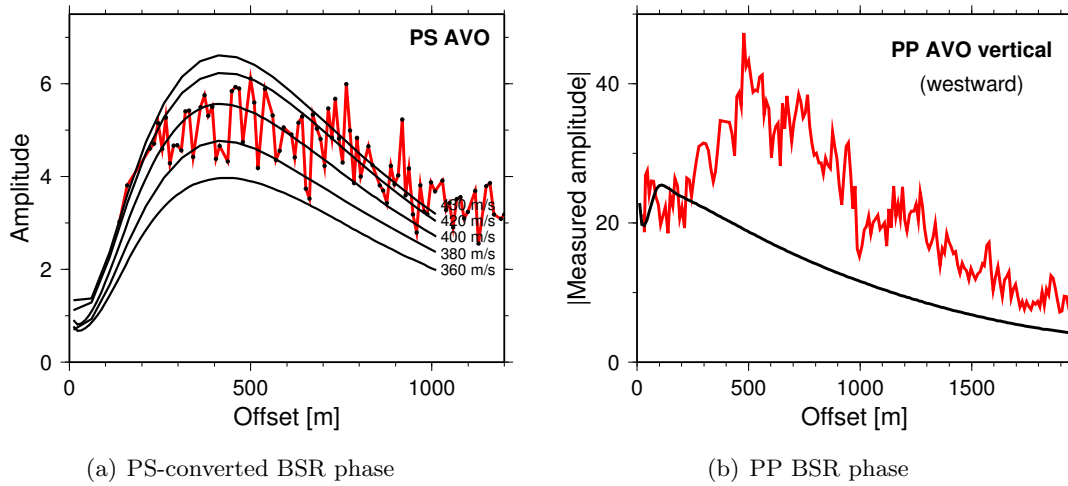


Figure 6.13: AVO behaviour of the P-S converted BSR phase modeled for different v_s values above the BSR (left), PP AVO curve (vertical component) ($v_s = 400$ m/s) for comparison, real amplitudes are plotted as red lines.

diverge significantly with increasing offsets. The higher measured P-wave amplitudes can be caused by either larger impedance contrasts in v_p and ρ or by lower shear wave velocity contrasts west of OBS 41. The former is supported by a westward increase in R_{bsr} (see GI-Gun section in Figure 4.2). Moreover, lower P-wave velocities are obtained from the inversion model in the westward offset range of ~ 200 m at the BSR, which is associated with a shot offset range of 1500 m. They indicate lower hydrate saturations and thus lower v_p and v_s . Therefore, lower P-wave velocities below the BSR seem to be a more likely explanation, which is supported by the changing style of the sub-BSR reflectivity seen in the GI-Gun section pointing towards increased accumulations of gas that produce the higher amplitudes. In conclusion, this illustrates the limited accuracy that can be expected from PP AVO analyses when lateral variations are present.

The effect of the gradient interface on the AVO behaviour compared to a sharp transition has also been investigated by synthetic modeling and is shown in Figure 6.14. For the PP phase, it can be seen that the two curves converge with increasing offset, i.e. the amplitude loss caused by the gradient decreases. The offset-dependent decrease results from the increase in wavelength caused by attenuation. In order to convert the PP amplitudes measured in the case of a gradient layer to those that would have been observed if a sharp transition was present, a calibration function c_{pp} was determined empirically:

$$c_{pp} = 0.65 + 0.35 \cdot \frac{x}{2500}, \quad (6.7)$$

where x is offset in m. In case of the PS amplitudes, a good fit is yielded by applying a scalar factor c_{ps} of 0.75. Calibration of the amplitudes for a sharp transition results in the dashed curves in Figure 6.14 which fit the AVO curve in case of a gradient very well.

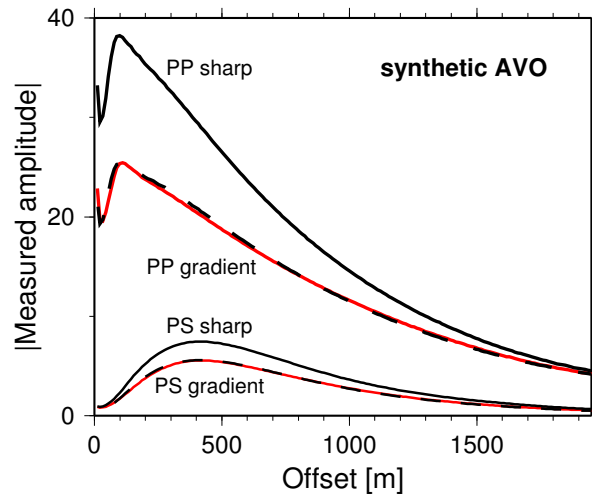


Figure 6.14: AVO behaviour of the BSR phases modeled for a sharp transition at the BSR (solid black) and a linear transition of 2.5m (red). Dashed lines are obtained after scaling of sharp AVO curve with calibration functions given in text.

The final model of the elastic parameters beneath OBS 41 resulting from the performed analysis is displayed in Figure 6.15. The associated synthetic seismograms of the radial and vertical component are shown in Figure 6.16.

A good match between the calculated traveltimes of the PP and PS phases and those observed in the real data (Figure 6.3) can be stated. The P-wave velocity distribution matches the Hamilton reference curve down to the BSR depth and thus, would not indicate high saturations of hydrate if the reference curve is valid for the Hydrate Ridge region.

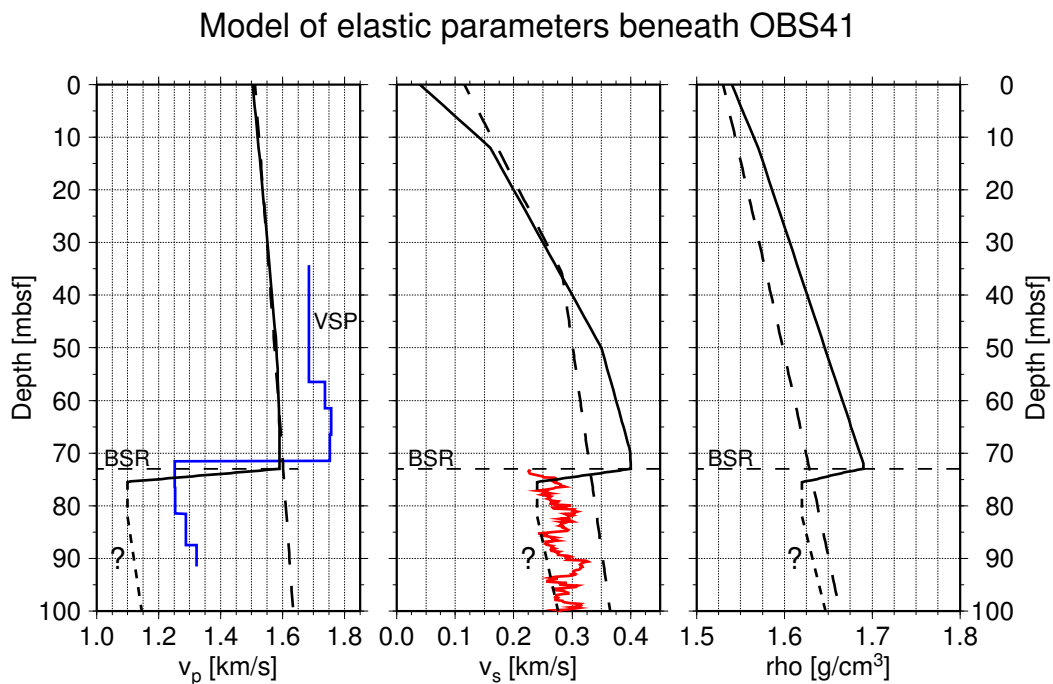


Figure 6.15: Final model of the elastic parameters beneath OBS 41. Sonic v_s log of ODP Leg 204 in red, VSP velocities in blue.

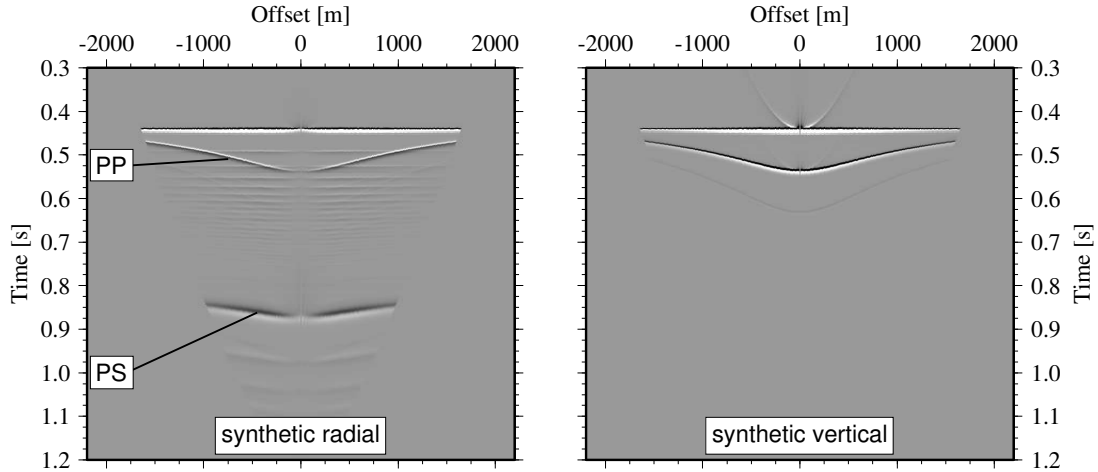


Figure 6.16: *Synthetic radial and vertical component calculated for model shown in Figure 6.15, compare to real data in Figure 6.3.*

Compared to the VSP data from ODP Site 892, it shows lower velocities but a similar impedance contrast at the BSR. The assumed v_s distribution coincides only partly with the reference, showing lower velocities beneath the seafloor and increased velocities below 40 mbsf. In contradiction to v_p the elevated velocities clearly indicate hydrated sediments above the BSR. Below the BSR v_s is lower but in principal comparable with the Hamilton curve. From the $\frac{v_p}{v_s}$ ratios of 3.96 above the BSR and 4.58 below the BSR, an increase in Poisson ratio at the BSR from 0.466 to 0.475 can be deduced. The density curve, which was inferred by ODP log data, is always above the displayed reference curve, indicating that sediment properties are different from those underlying the Hamilton curve.

6.3 PP AVO analysis of OBH/S data

The P-wave data recorded along the main line by the OBH/S instruments were input for a qualitative AVO analysis. Unfortunately, only six instruments had unclipped data and could be used. The locations of these instruments are displayed in Figure 4.2 and are also marked in the regional maps shown in Chapter 4. A detailed quantitative approach like at OBS 41 was not possible because shear wave data were either missing, as for the OBH, or they were of too low s/n ratio, as for the other OBS stations. Due to the above mentioned large footprint of the PP reflection, the AVO curves do not represent the BSR properties beneath the instruments, but rather they reflect their lateral variation within the footprint area.

Several corrections have to be accounted for in order to enable a comparison with amplitudes obtained from the Zoeppritz equations. First, the effect of geometrical spreading, i.e. the amplitude loss attributed to wave propagation, is corrected by multiplying the amplitudes with the particular traveltimes. In principal, this is only valid for a constant medium velocity, but it can be justified by the fact that the BSR is very shallow and that sediment velocities are only slightly higher than the water velocity. Second, the ghost of the seismic source produces an amplitude decrease with increasing angles. For a point

source that is operated at a depth much smaller than the dominant wavelength, the amplitude loss is approximately proportional to the cosine of the take-off angle ϕ . The GI-Gun was towed in ~ 2 m depth and thus, the amplitudes were divided by $\cos \phi$. The fact that the airgun is not a perfect point source is neglected. Third, the seismometer components record the particle motion in the direction of the horizontal or vertical axes. Therefore, amplitudes of a seismic wave arriving at an oblique angle ψ at the geophone are actually higher than those recorded. This receiver directivity can be corrected by division of the amplitudes by $\cos \psi$ or $\sin \psi$ for the vertical and radial component, respectively. The necessary information about the traveltimes, the take-off angles and the arriving angles was obtained from the log files of the inversion program *rayinvr*. Although the overall correction is afflicted with some inaccuracies due to the mentioned simplifications, the result was satisfactory, as it could be checked for the direct arrivals. As it was shown for OBS 41, attenuation and a gradient transition zone affect the amplitudes as well. Lacking reliable information about the lateral variation of these parameters, they have not been taken into account. In principal, a correction for both Q_p and a possible gradient BSR interface over a few meters would result in a general increase of the amplitudes. The attenuation effect increases with increasing offset due to the longer travel paths through the sediment, whereas the gradient interface effect is strongest at the near-offset. Since the purpose of this analysis is a qualitative estimate, the vertical-incidence reflection amplitudes have been normalized to the reflection coefficients obtained from the MCS data at the particular locations.

The obtained corrected amplitudes for the six instruments are plotted against the incidence angle at the BSR in Figure 6.17. The angle at the BSR was also derived from the inversion program and thus represents the true incidence angle, i.e. ray bending effects are included.

By looking at the AVO curves, evidence for the strong influence of lateral variations is given by the different appearances of the eastward and westward curves. Only OBH 55, which is located above a very smooth and continuous BSR, shows a uniform AVO behaviour towards both sides. Especially the PP AVO curve at OBS 41, for which the detailed amplitude analysis was performed, strongly deviates from the theoretical Zoeppritz curve calculated for the derived elastic model (solid line). The dotted line represents the theoretical AVO curve when no contrast in v_s is assumed. The difference is far too small to explain the much higher measured amplitudes, which are rather a result of lateral variations of BSR properties.

This clearly demonstrates that a PP AVO analysis of the OBH/S data that were available is not capable of resolving the v_s contrast that can be expected at the BSR. For the other stations, theoretical AVO curves were fitted to the measured R_{bsr} for vertical incidence. Since v_p above the BSR could be taken from the inversion velocity model, a rough estimation of the P-wave velocity below the BSR was obtained assuming similar contrasts in v_s and ρ as for OBS 41. For OBH 57 and OBH 58, density was only decreased to 1.65 g/cm^3 due to the lower reflection coefficients. The obtained velocities are summarized in Table 6.4 and give an indication of the amounts of gas present, which will be discussed in Chapter 7.

By comparison with the BSR amplitudes of the GI-Gun SCS data shown in Figures 4.2 and 4.6 (b), a good consistency in a broad sense can be stated. Major dif-

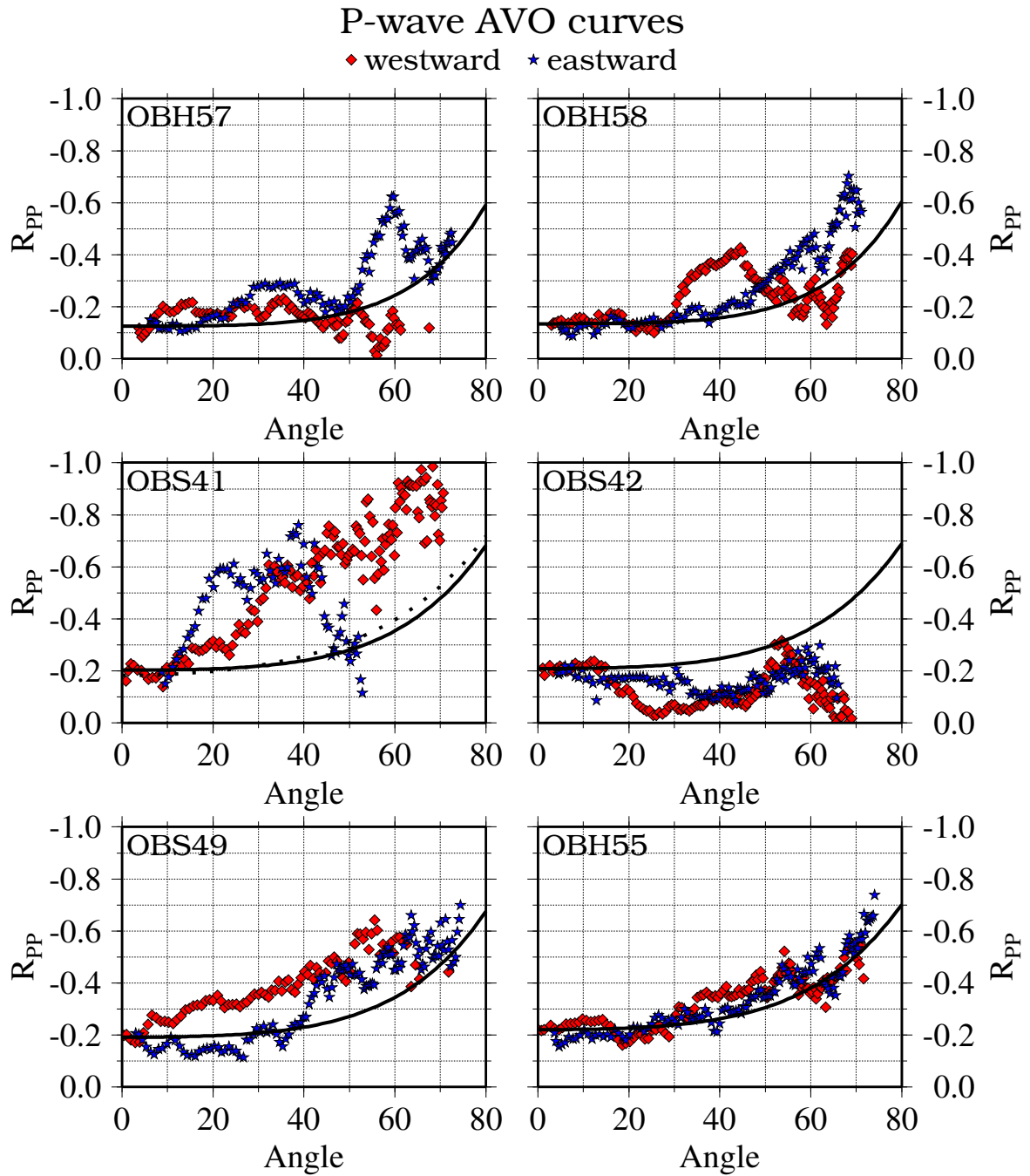


Figure 6.17: AVO behaviour of the PP BSR reflection at OBH/S stations. Locations of instruments are shown in Figure 4.2

ferences occur only for the western stations 49 and 55 for which the SCS data yields smaller values. This is due to the larger deviation of the SCS R_{bsr} from the one obtained from the MCS data at these locations. The ratios of the particular reflection coefficients for the six instruments are also given in Table 6.4. The higher values indicate a wider transition at the BSR than that of 1.5-2.5 m obtained beneath OBS 41.

	v_p above BSR	v_p below BSR	Δv_p	$\frac{R_{bsr}(MCS)}{R_{bsr}(SCS)}$
OBS 49	1670 m/s	1150 m/s	520 m/s	~ 2.61
OBH 55	1620 m/s	1050 m/s	570 m/s	~ 2.54
OBS 41	1590 m/s	1100 m/s	490 m/s	~ 1.83
OBS 42	1610 m/s	1100 m/s	510 m/s	~ 1.75
OBH 57	1635 m/s	1300 m/s	335 m/s	~ 1.92
OBH 58	1600 m/s	1250 m/s	350 m/s	~ 1.79

Table 6.4: *Input parameters for the Zoeppritz solutions shown in Figure 6.17 and ratio between BSR reflection coefficients derived from MCS and SCS data for the six OBH/S used for the PP AVO analysis.*

In conclusion, despite of the deviations due to varying BSR transition thicknesses, this analysis shows that the regional map of the BSR amplitude (Figure 4.6 (b)) provides good constraints on the relative distribution of free gas at northern Hydrate Ridge. However, it must be kept in mind that larger quantities of free gas moving rapidly into the GHSZ are likely to disrupt or even destroy the BSR signature. Thus, areas in the regional map, which show an abrupt drop to zero BSR amplitudes, i.e. no BSR could be picked, are likely to represent regions of massive upward migration of free gas and are indicative for even higher free gas saturations. To overcome the problem of lateral changing BSR properties for the P-wave AVO analysis, closer instrument spacings of less than 30 m are needed, which would allow a sorting into CDP gathers. The Fresnel zone increases significantly with offset for the common OBH/S configuration. By operating a seismic source at or near the seafloor it would be much smaller. Moreover, a true-amplitude migration of the OBH/S data would further improve the AVO analysis by reducing the Fresnel zone.

6.4 MCS profile OR89-09

The data of MCS profile OR89-09 acquired along the main line (*MacKay et al.*, 1992) were used for a P-wave AVO processing. With a streamer length of 3 km and 72 channels, a CDP spacing of 12.5 m was obtained. Although the low frequency source and the surface streamer configuration lead to a large Fresnel radius of about 120 m, accurate results could be expected due to the close CDP coverage. Processing steps included corrections for source and receiver directivities and a 2D time migration in the common offset domain to minimize the Fresnel zone and take focusing and defocusing effects into account. Prior to extracting the AVO gradient and AVO intercept, angles greater than 30° have been discarded from the analysis because of the limitation of the AVO gradient concept to intermediate offsets (see Section 6.1). The results are displayed in Figure 6.18.

The AVO gradient shows strong lateral variations, which are consistent with the observations from the OBH/S P-wave AVO curves. In general, values fluctuate from 0 to about 0.4 indicating sudden lateral changes in elastic parameters. These are most probably caused by varying free gas saturations or structural variations. The deduced low to intermediate positive gradients agree in principal with the OBH/S AVO curves for OBS 49, OBH 55, OBH 57 and OBH 58 at angles smaller than 30° . A prominent maximum

can be seen west of OBS 41, which correlates well with the increased amplitudes in the OBS AVO curve. The negative gradients beneath OBS 42 and west of OBH 55 can also be assigned to decreases in the particular OBH/S AVO curves. The derived AVO intercept values at the BSR, which should be similar to $R_{b_{sr}}$ for vertical-incidence, are of little interpretative importance because they deviate from the reflection coefficients obtained directly from the migrated data. The reason for the deviation, which can be observed in particular at the AVO gradient maximum west of OBS 41, is that gradient and intercept are determined by a linear regression of the amplitudes plotted against $\sin^2 \phi$. If lateral changes occur within the Fresnel zone, which is the case beneath OBS 41, the amplitudes in the CDP gather will also reflect these changes and the extrapolated regression curve leads to wrong reflection coefficients.

However, due to the close CDP coverage, a reliable qualitative assessment of the AVO behaviour can be obtained from the AVO gradient analysis. For example, it can be suggested that the strong positive anomaly west of OBS 41 represents a pocket containing high amounts of free gas.

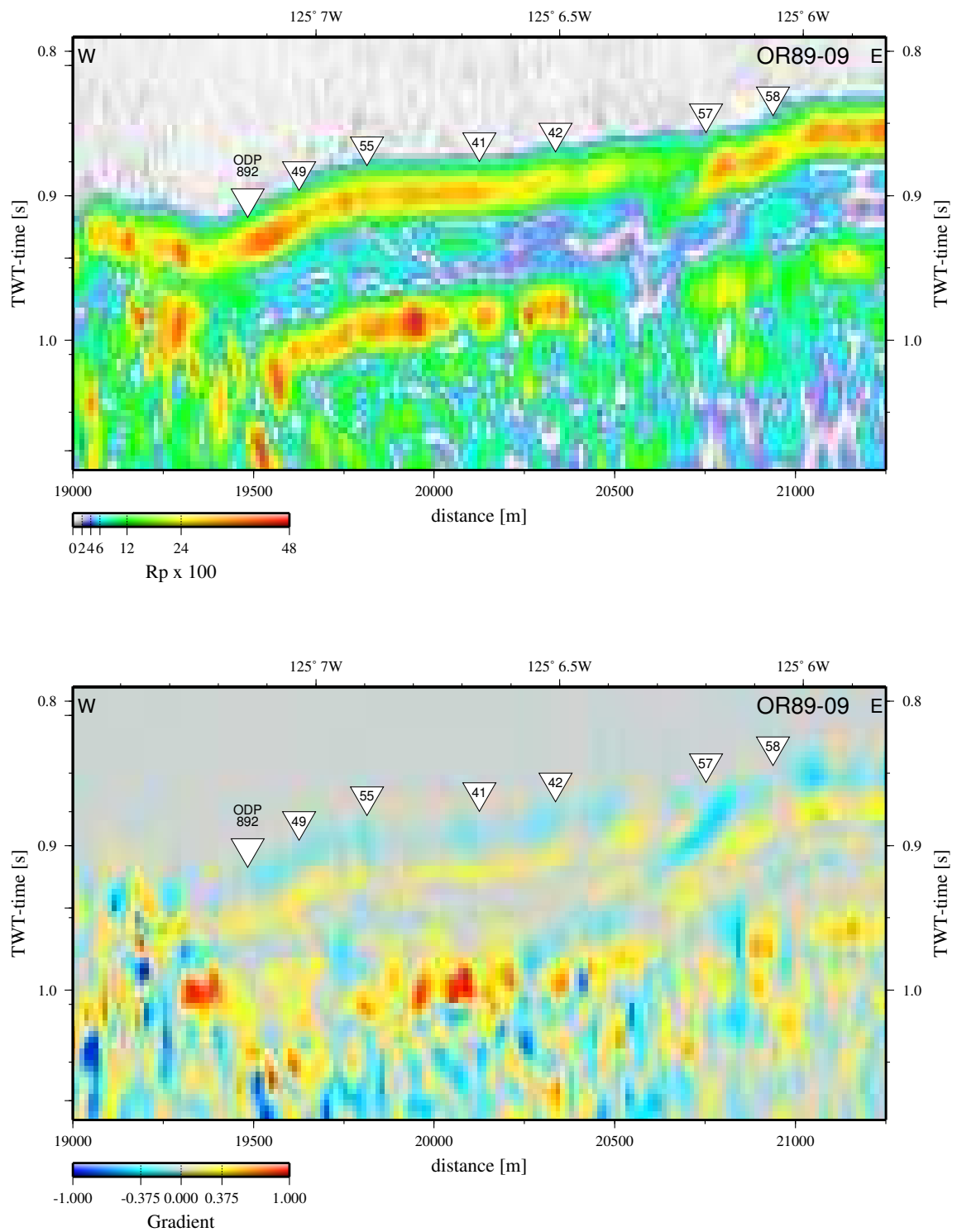


Figure 6.18: AVO intercept and AVO gradient derived from CDP gathers of MCS line OR89-09.

Chapter 7

Estimation of hydrate and free gas saturation

An estimate of the hydrate and free gas saturations can be obtained by rock physics models, which are used to calculate the macroscopic elastic properties of the sediment from the particular sediment constituents and its microstructure. Since the presence of hydrate increases v_p and v_s and the presence of free gas decreases v_p , the respective amounts of hydrate and free gas can be quantified by comparing the observed deviations of these properties from those predicted for sediments where no gas hydrate or free gas is present.

In this context, several methods based on an effective-medium approach have been developed that obtain the elastic parameters of the composite sediment by averaging different physical parameters of the sediment constituents. These theories are the weighted-equation (WE) approach of *Lee et al.* (1996), a three-phase effective-medium (TPEM) theory (*Ecker et al.*, 1998; *Helgerud et al.*, 1999; *Ecker et al.*, 2000), a three-phase Biot theory (TPB) (*Carcione and Tinivella*, 2000; *Gei and Carcione*, 2003) and a differential effective-medium (DEM) approach of *Jakobsen et al.* (2000). A detailed discussion of these models is beyond the scope of this thesis and the reader is referred to the cited publications. A general comparison of the different methods including application to field data has been given recently by *Chand et al.* (2004). The predicted variation of v_p and v_s with hydrate saturation for the particular elastic velocity models assuming a clay content of 50 % is illustrated in Figure 7.1. Only the TPEM and the TBM models predict velocities for a hydrate-free, high-porosity and clay-rich sediment, which are in the range of the observed values for v_p above and for v_s below the BSR. The other models yield velocities for zero hydrate saturation, which are already higher than those observed and consequently, have been discarded for the analysis at northern Hydrate Ridge. The comparison of the TPEM and the TBM model for the velocity and porosity values obtained at Hydrate Ridge shows that the TBM model yields higher hydrate saturations. Since the equations underlying the TBM model could not be recalculated, it was not further analyzed. Only a rough estimate of the hydrate saturation to about 10-15 % is possible from Figure 7.1. *Zillmer et al.* (submitted) derived explicit formulas for the gas hydrate and free gas saturations from the Gassmann equations. The method is equivalent to the TPEM approach and is presented in detail in the following.

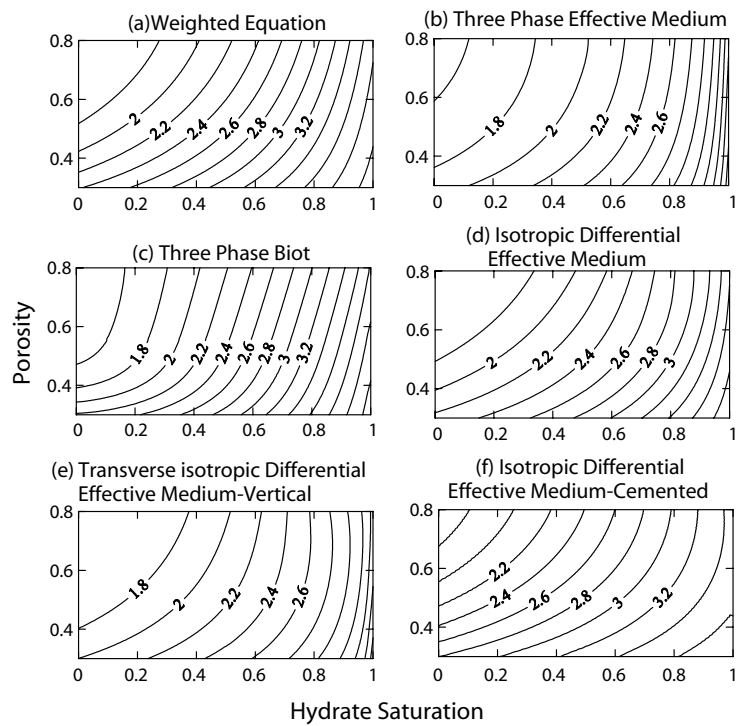


Figure 5. V_p as a function of porosity and hydrate saturation at 50 per cent clay content for different models: (a) WE, (b) TPBM, (c) TPB, (d) isotropic DEM model with clay-water starting model, (e) vertical velocity for transverse isotropic DEM model with clay-water starting model and an aspect ratio of 0.05, (f) isotropic DEM model with clay-hydrate starting model.

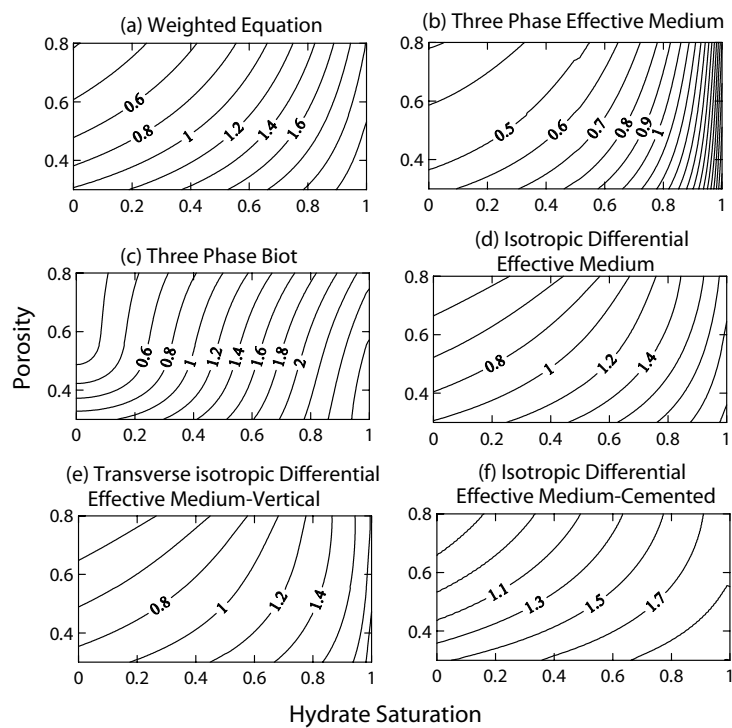


Figure 6. V_s as a function of porosity and hydrate saturation at 50 per cent clay content for different models: (a) WE, (b) TPBM, (c) TPB, (d) isotropic DEM model with clay-water starting model, (e) vertical velocity for transverse isotropic DEM model with clay-water starting model and an aspect ratio of 0.05, (f) isotropic DEM model with clay-hydrate starting model.

Figure 7.1: Predicted variations of v_p and v_s with hydrate saturation for the different elastic velocity models (Chand et al., 2004).

7.1 Bulk and shear modulus

The elastic moduli of the saturated sediments beneath OBS 41 can be directly obtained from the derived model of v_p , v_s and ρ . The bulk modulus K is given by:

$$K = \rho v_p^2 - \frac{4}{3}\mu, \quad (7.1)$$

and the shear modulus μ is given by:

$$\mu = \rho v_s^2. \quad (7.2)$$

The calculated moduli are shown in Figure 7.2. The bulk modulus increases from 3.5 GPa at the seafloor to 3.9 GPa at the BSR, where it decreases below 2 GPa in the free gas layer. The shear modulus is zero at the seafloor, increases to 0.27 GPa at the BSR and drops down to 0.09 GPa below the BSR.

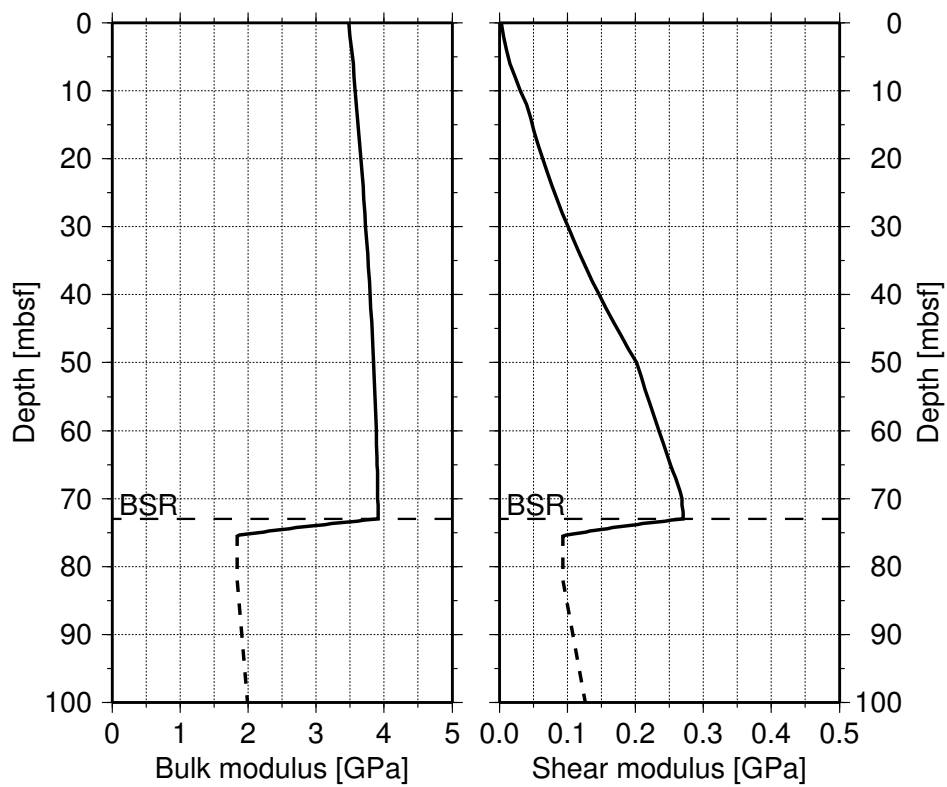


Figure 7.2: Bulk and shear modulus of the saturated sediment obtained for elastic parameter model at OBS 41 given in Figure 6.15.

7.2 Hydrate saturation

For the determination of the hydrate and free gas saturations beneath OBS 41 the approach proposed by *Zillmer et al.* (submitted) is used. The fundamental equation describing the elasticity of a porous media is the Gassmann equation which was used to calculate the bulk modulus of the saturated sediment (*Gassmann, 1951; Geertsma and Smit, 1961; Sheriff and Geldart, 1995*):

$$K = K^* + \beta^2 \left[\frac{\phi}{K_f} + \frac{\beta - \phi}{K_s} \right]^{-1}, \quad \beta = 1 - \frac{K^*}{K_s}, \quad (7.3)$$

where ϕ is porosity and K, K^*, K_s and K_f are the bulk moduli of the saturated and the dry sediment, and of the solid and of the fluid phase, respectively. For the subsequent analysis a mineralogy of 60 % clay, 20 % quartz and 20 % feldspar was assumed which is an averaged estimate from the ODP data at Site 892A (*Westbrook et al., 1994*). The relevant elastic parameters are given in Table 7.1.

	Clay	Quartz	Feldspar	Hydrate	Water	Methane
Bulk modulus [GPa]	21*	36.6*	37.5*	8.3 ⁺	2.28 ¹	0.012 ¹
Shear modulus [GPa]	7*	45*	15*	3.5 ⁺	0	0
Density [g/cm ³]	2.6*	2.65*	2.62*	0.91 ⁺⁺	1.02 ¹	0.06 ¹

Table 7.1: *Properties of sediment constituents used for elastic modeling* (* = *Mavko et al. (1998)*,⁺ = *Helgerud et al. (2003)*,⁺⁺ = *Sloan (1998)*,¹ = *calculated according to Mavko et al. (1998)* for a temperature of 9°C and a pressure of 7.5 MPa at the BSR.

The bulk modulus of the solid phase K_s is calculated from those of the individual mineral constituents using Hill's average formula (*Hill, 1952*):

$$K_s = \frac{1}{2} \left[\sum_i (f_i K_i) + \left(\sum_i \left(\frac{f_i}{K_i} \right)^{-1} \right)^{-1} \right], \quad (7.4)$$

where f_i and K_i are the volumetric fraction and the bulk modulus of the i -th constituent, respectively. A value of K_s of 26.4 GPa is obtained for the mineralogy given above. Analogue, the shear modulus μ_s can be calculated to 13 GPa leading to a Poisson ratio σ_s of 0.29 for the solid phase.

The dry sediment bulk modulus K^* can be obtained by an empirical formula given by *Hamilton (1971)*:

$$K^* \approx K_s \cdot 10^{-4.25\phi}. \quad (7.5)$$

A theoretical approach to calculate K^* based on the Hertz-Mindlin theory has been proposed by *Mavko et al. (1998)* and *Dvorkin et al. (1999)*. With a porosity of 58 % at the BSR for the northern Hydrate Ridge sediments estimated from ODP measurements (*Jarrard et al., 1995*) Equation 7.5 leads to a K^* of 0.09 GPa, whereas the theoretical method yields 0.19 GPa. Similar results for the gas hydrate saturation are obtained (see Equations 7.8 and 7.9 below), because K^* is small compared to K and K_s . The empirical Equation 7.5 is preferred to the theoretical approach due to its simpler form.

Another empirical relation for K^* has been derived at Blake Ridge using borehole information from ODP Leg 164 (*Guerin et al.*, 1999):

$$K^* \approx K_s \cdot 10^{3.02-7.372\phi}. \quad (7.6)$$

This equation yields a much higher K^* of 1.44 GPa which has been attributed to gas hydrate cementing the grain boundaries. For the Hydrate Ridge data, use of Equation 7.6 results in negative values for the hydrate saturation which are physically implausible. Consequently, the empirical equation by Hamilton was used for the saturation estimate.

Two different models are considered, one with hydrate as a part of the pore fluid (suspension model), the other with hydrate as a part of the solid phase (grain contact model). Both models were proposed by *Helgerud et al.* (1999) and by *Ecker et al.* (2000).

If hydrate is a part of the pore fluid, it does not affect the stiffness of the dry frame. In this case, the effective bulk modulus of the pore fluid K_f is calculated by using the Reuss average of the water and hydrate bulk moduli K_w and K_h (*Reuss*, 1929; *Mavko et al.*, 1998):

$$\frac{1}{K_f} = \frac{\bar{S}_h}{K_h} + \frac{1 - \bar{S}_h}{K_w}, \quad (7.7)$$

where \bar{S}_h is the hydrate saturation of the pore space. Following *Zillmer et al.* (submitted) \bar{S}_h can be derived by substitution of Equation 7.7 into the Gassmann equation 7.3:

$$\bar{S}_h = \left(\frac{1}{K_w} - \frac{1}{K_h} \right)^{-1} \left[\frac{1}{K_w} - \frac{1}{K_s} - \frac{\beta}{\phi} \left(\frac{\beta}{K - K^*} - \frac{1}{K_s} \right) \right]. \quad (7.8)$$

In the grain contact model, hydrate reduces the porosity and alters the elastic properties of the solid phase. With the effective porosity $\bar{\phi} = \phi - \phi S_h$ substituted for ϕ in Equation 7.3 the hydrate saturation S_h is given by:

$$S_h = 1 - \left(\frac{1}{K_w} - \frac{1}{K_s} \right)^{-1} \frac{\beta}{\phi} \left(\frac{\beta}{K - K^*} - \frac{1}{K_s} \right). \quad (7.9)$$

In principal, K_s and K^* are functions of S_h which requires a numerical solution of Equations 7.9 and 7.8. However, if the hydrate saturation is small, the equations can be solved directly.

7.3 Free gas saturation

To estimate the free gas saturation, two different models have been proposed by *Helgerud et al.* (1999). The first assumes a homogenous gas distribution in the form of a suspension in the pore fluid, the second assumes a patchy distribution of fully gas and fully water saturated sediment. For the suspension model, it is assumed that each pore has the same proportions of gas and water. Formally, the same result as for the hydrate saturation (Equation 7.8) is obtained after substituting K_h with K_g :

$$\bar{S}_g = \left(\frac{1}{K_w} - \frac{1}{K_g} \right)^{-1} \left[\frac{1}{K_w} - \frac{1}{K_s} - \frac{\beta}{\phi} \left(\frac{\beta}{K - K^*} - \frac{1}{K_s} \right) \right]. \quad (7.10)$$

In case of a patchy distribution, the pore space is assumed to consist of neighbouring regions of fully gas-saturated and fully water-saturated regions on a length scale larger

than the pore size, but much smaller than the seismic wavelength. The derivation of the equation for the patchy saturation S_g can be found in *Zillmer et al.* (submitted), and the ratio of the estimated free gas saturation of the two models is given by:

$$\frac{S_g}{S_g} = (K - K^*)\beta^{-2}\phi^{-1}\left(K + \frac{4}{3}\mu\right)^{-1}\left[\beta^2 + (K^* + \frac{4}{3}\mu)\left(\frac{\phi}{K_g} + \frac{\beta - \phi}{K_s}\right)\right]. \quad (7.11)$$

Application of the given equations to the elastic parameter model derived at OBS 41 (Figure 6.15) leads to the hydrate and free gas saturations shown in Figure 7.3. Since the ODP porosity data show scattering and only allow a rough estimation of ϕ , a smooth porosity function was calculated from the density distribution. Density is described by the volumetric average of the sediment's constituents:

$$\rho = (1 - \phi)\rho_s + (\phi - \phi S_h)\rho_w + \phi S_h\rho_h. \quad (7.12)$$

Thus, ϕ is given by:

$$\phi = \frac{\rho_s - \rho}{\rho_s - \rho_w + S_h(\rho_w - \rho_h)}. \quad (7.13)$$

For small gas hydrate saturations, the porosity can be approximated by the porosity of the fully water-saturated sediment (*Zillmer et al.*, submitted):

$$\phi \approx \frac{\rho_s - \rho}{\rho_s - \rho_w}. \quad (7.14)$$

For $\rho_s = 2.61 \text{ g/cm}^3$ the porosity function shown on the right in Figure 7.3 is obtained. It is in good agreement with the ODP porosity data (*Jarrard et al.*, 1995).

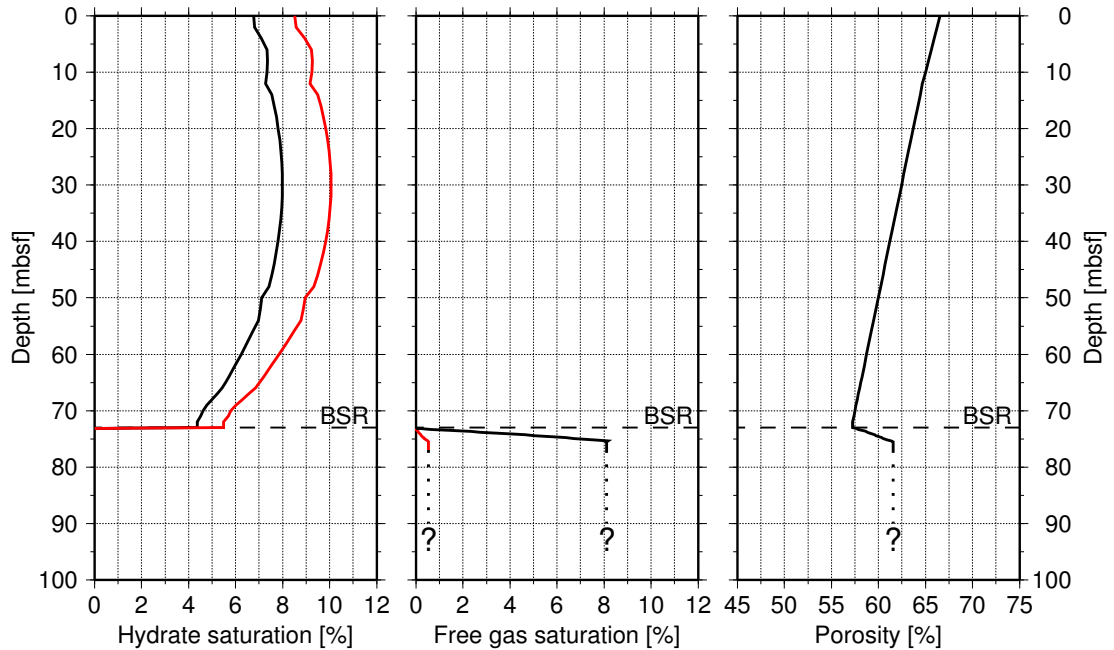


Figure 7.3: Hydrate and free gas saturations obtained for elastic parameter model given in Figure 6.15, hydrate as part of the solid phase/ patchy distribution of free gas (black lines); hydrate and free gas as part of the pore fluid (red lines).

The grain contact model yields a hydrate saturation of 4.4 % at the BSR, whereas the model of gas hydrate as part of the pore fluid leads to a higher value of 5.5 %. The hydrate saturation distribution from the seafloor to the BSR is afflicted with higher uncertainties because of the assumed smooth distributions due to missing seismic reflectors. However, assuming that the derived elastic properties are in principal reliable, the hydrate saturation starts with 6.8 % (8.5 %) at the seafloor, increases to a maximum of 8 % (10 %) at 30 mbsf and finally decreases to the values at the BSR. Values in brackets represent the results for the pore fluid model. Assuming that the two models represent upper and lower bounds for gas hydrate saturation, an average estimate of 4-10 % can be suggested for the GHSZ. The free gas saturations below the BSR obtained for the homogenous and patchy distribution differ significantly. The suspension model predicts very small saturations of 0.53 %, which reflects that minor amounts of uniformly distributed free gas are sufficient to decrease v_p dramatically (*Domenico, 1976*). In contrast, the patchy model leads to a much smaller velocity variation at small gas saturations. Therefore, an about 15 times higher gas saturation of 8.1 % is obtained. Since both models represent the extreme end members of possible gas distributions, it can be assumed that an intermediate model applies to the pore space settings prevailing in reality. With this assumption, an average free gas saturation of 0.5-8 % might be suggested.

At the locations of the other five OBH/S instruments for which an P-wave amplitude analysis was performed, the hydrate and free gas saturations are also calculated based on the P-wave velocities above and below the BSR given in Table 6.4. The other elastic parameters were assumed similar to those at OBS 41. With this assumption, the hydrate and free gas saturations given in Table 7.2 are obtained.

It can be seen that small variations in P-wave velocity affect the hydrate saturation significantly, whereas minor changes in gas saturation lead to major changes in v_p below the BSR. Since the variations in P-wave velocity along the main line do not correlate well with the determined reflection coefficients, it can be assumed for the Hydrate Ridge area that the BSR reflection amplitude is mostly controlled by the free gas saturation. This observation is consistent with results from previous investigations (e.g. *Trehu et al., 1995*). The dominant influence of gas on the BSR amplitude was also shown in studies at other gas hydrate locations (e.g. *Singh et al., 1993; Singh and Minshull, 1994; Minshull et al., 1994*). The higher hydrate saturation obtained for OBS 49 correlates well with the maximum saturation of 16 % determined from chlorinity measurements at ODP Site 892

	S_h	\bar{S}_h	S_g	\bar{S}_g
OBS 49	16 %	20 %	0.42 %	6.6 %
OBH 55	9 %	11 %	0.64 %	9.8 %
OBS 41	4.4 %	5.5 %	0.53 %	8.1 %
OBS 42	7.4 %	9 %	0.52 %	8.1 %
OBH 57	11 %	14 %	0.19 %	3.1 %
OBH 58	6 %	7.4 %	0.26 %	4.2 %

Table 7.2: Gas hydrate and free gas saturations at OBH/S obtained from velocities given in Table 6.4.

(Kastner *et al.*, 1995). The strongest decrease in v_p is observed at OBH 55 leading to slightly higher free gas saturations of 0.64 % (9.8 %) for the suspension model (patchy model) as determined at OBS 41. Similar free gas saturations are obtained at OBS 42 and OBS 49, whereas the most easterly stations 57 and 58 show a much smaller v_p decrease indicative for lower amounts of gas underlying the BSR. For the suspension model, 0.19-0.26 % are obtained whereas the patchy model yields about 3-4 %.

7.4 Error discussion

An error estimation was performed for the calculated hydrate and free gas saturations on the basis of the error propagation after Gauss. The errors for the particular saturations are calculated using the following equation:

$$\Delta S = \sqrt{\sum_{i=1}^n \left(\frac{\partial S}{\partial x_i} \Delta x_i \right)^2}, \quad (7.15)$$

where Δx_i are the absolute errors of the single input parameters, which are given in Table 7.3. The partial derivatives of Equations 7.8, 7.9, 7.10 and 7.11 with respect to the independent variables can be found in *Zillmer et al.* (submitted).

parameter	assumed error
v_p	± 25 m/s
v_s	± 100 m/s
ρ	± 0.05 g/cm ³
ϕ	± 5 %
K	± 0.1 GPa
μ	± 0.05 GPa
K^*	± 0.07 GPa
K_w	± 0.02 GPa
K_g	± 0.001 GPa
K_s	± 3 GPa

Table 7.3: Errors assumed for the estimation of the hydrate and free gas saturations.

For the hydrate saturation ΔS_h , an absolute error of ± 9 % is obtained. The uncertainty in porosity has the most dominant influence on ΔS_h . For small hydrate concentrations, it can be shown that the relative error in porosity $\frac{\Delta \phi}{\phi}$ is approximately equivalent to the absolute error in hydrate saturation. Application of Equation 7.15 to the gas saturation equations yields an absolute error of ± 0.12 % for the suspension model and ± 4.4 % in case of a patchy distribution.

Thus, the hydrate saturation at OBS 41 might vary between 0 % and 14.5 %, which is the upper bound for the model with hydrate being a part of the pore fluid. The error for the free gas saturations leads to possible ranges from 0.41 % to 0.65 % for the suspension model and from 3.7 % to 12.5 % for the patchy model.

Chapter 8

Discussion and conclusions

The presented seismic data analyses aimed at the seismic characterization of the gas hydrate reservoir at northern Hydrate Ridge. This aim was achieved by an integrated approach, which consisted of a very detailed local amplitude study at a single OBS location, a velocity and amplitude analysis along a 2D line and a 3D investigation of the sediment structures and BSR properties using regional SCS data. In the following, the implications that arise from the particular studies are discussed and combined to derive a characterization of the hydrate and free gas environment as complete as possible with the available database.

The local amplitude analysis at OBS 41 yielded a detailed model of the elastic parameters at the BSR. The multi-frequency data was essential to this analysis, because it enabled the determination of the compressional wave attenuation and of the thickness of the BSR transition zone. The elastic model could only be obtained because a prominent S-wave, which was generated by a P-S conversion at the BSR, was recorded by the seismometer. The amplitude analysis of the P-S converted BSR phase enabled the determination of the shear wave velocity contrast at the BSR. With a drop from 400 m/s to 240 m/s, the contrast is quite large for the rather low hydrate saturations of about 5 % obtained from the rock physics modeling. This indicates that a small percentage of hydrate might be sufficient to increase the shear modulus by stiffening the sediment frame. Since an increased shear modulus also results in higher P-wave velocities, a principal problem is encountered by the fact that v_p values are only slightly increased. Moreover, no correlation between high BSR reflectivity and increased P-wave velocities has been found. A possible solution might be given by a co-existence of free gas and gas hydrate within the GHSZ. Massive gas venting is known to occur at Hydrate Ridge, which clearly indicates that free methane is moving through the GHSZ. It was suggested by *Suess et al.* (1999) that this phenomenon is a result of a special circumstance of gas-water segregation, i.e., the free gas moves along channels lined with gas hydrate that has incorporated all surrounding water. *Milkov et al.* (2004) gave further evidence for the co-existence of free gas and hydrate by observations from a pressurized core recovered at southern Hydrate Ridge during ODP Leg 204. Rather than arguing for a segregation of free gas and water, they hypothesize that the free gas moves through the GHSZ in association with high salinity pore fluids. During gas hydrate formation, methane and water are extracted from the pore water, whereas dissolved ions remain in the pore fluid resulting in an increase in salinity. According to *Handa* (1990)

at a certain point during hydrate formation a gas hydrate-free gas-brine equilibrium is reached, permitting excess gas to enter the free gas phase rather than the hydrate phase. Thus, a possible explanation for the co-existence might be given by rapid hydrate formation due to high gas fluxes. However, the exact cause of the co-existence is yet unclear, but, since the physical properties are strongly affected by the presence of free gas, hydrate and salinity, it has severe consequences for the hydrate quantification methods. Regarding the hydrate saturation estimates from seismic velocities, the presence of free gas would lower the P-wave velocities and thus an underestimation of the hydrate saturation can be expected. Consequently, the hydrate saturation of about 4-6 % at the BSR and up to 10 % within the GHSZ obtained from the rock physics models represents a lower limit and actually might be higher. However, the derived saturations roughly agree with estimates obtained from Cl^- measurements from ODP Site 892, which indicate maximum saturations of 16 % (Kastner *et al.*, 1995). The higher saturations correlate well with the higher P-wave velocity of 1670 m/s (Tables 6.4 and 7.2) and the higher average shear wave velocity of 240 m/s obtained from the P-S converted BSR phase at OBS 49 which is closest to the ODP Site (compared to a \bar{v}_s of 195 m/s at OBS 41, Section 5.4). Since the velocities at OBS 41 represent medium values within the range of velocities obtained along the main line, the deduced hydrate saturation is assumed to represent a good average of the prevailing conditions at the northern ridge. Compared to other areas, the obtained hydrate saturations are slightly higher than those at southern Hydrate Ridge (ODP204) and Blake Ridge (ODP164) which yielded similar average concentrations of 3-8 % and 2-7 %, respectively (Trehu *et al.*, 2003, 2004; Holbrook *et al.*, 1996; Dickens *et al.*, 1997). At the northern Cascadia margin, which is in a structurally similar setting, estimates of 20-35 % have been reported based on geophysical and chlorine anomaly data from ODP Site 889 (Hyndman *et al.*, 2001; Spence *et al.*, 2003). There is no evidence for cementation effects due to hydrate formation at northern Hydrate Ridge. The P- and S-wave velocities are much lower than would be expected if hydrate acts as an intergranular cement. This is not surprising since the cementation model is only appropriate for sediments with original porosities around the critical porosity of a sphere pack of about 35-40 % (Dvorkin *et al.*, 1994, 1999). Thus, its application is limited rather to low-porosity sand formations than to fine-grained clay-rich sediments with high porosities unless very high hydrate saturations are present. Uncemented sediments within the GHSZ have also been suggested for the southern Hydrate Ridge, the Blake Ridge and the northern Cascadia margin.

The determined free gas saturation of 0.5-8 % depending on the underlying model is sufficient to significantly decrease v_p and thus can be suggested to be the main cause for the strong BSR. Studies in other areas obtained similar amounts of gas beneath the BSR (e.g. Ecker *et al.*, 2000; Spence *et al.*, 2003; Schnurle *et al.*, submitted). The extent of the free gas layer was not constrained directly by the seismic data. However, a relatively thin layer of less than 20 m is unlikely because otherwise phase shifts would have been observed, especially in the low-frequent MCS data. Moreover, the absence of reflections from a possible base of free gas for all frequencies is a good indication for a gas layer of at least 50 m thickness with a gradual downward decrease in gas saturation. These assumptions are corroborated by results from VSP measurements at ODP Site 892 (MacKay *et al.*, 1994) and from a seismic refraction data analysis at northern Hydrate Ridge (Trehu and Flueh, 2001) pointing to a free gas layer of >50 m and possibly 500-600 m, respectively.

The analysis of the frequency-dependent variation of the reflection coefficients for the PP and PS BSR reflections enabled an estimation of the average attenuation of both compressional and shear waves at the location of OBS 41. The derived Q_p value of 150 stands in good agreement with commonly assumed P-wave attenuation values for marine near-surface sediments (*Hamilton, 1972; Wood et al., 2000; Ayres and Theilen, 2001*). The Q_s value of 35 is considerably lower than typically suggested attenuations of about 100 (e.g. *Bromirski et al., 1991*). Laboratory investigations indicated that attenuation in near-surface marine sediments is more pronounced for S-waves than for P-waves (*Ayres and Theilen, 2001*). The obtained Q_s was necessary to explain the low-frequency nature of the P-S converted waves. The low-frequency seems to be a general feature of soft, clay-rich, marine sediments and has also been observed at other locations, e.g. in the Black Sea (*Zillmer et al., submitted*) and at the Peruvian margin (*Flueh et al., 2002*). The observation that shear waves, which converted at both shallower and deeper structures than the BSR, also exhibit these low frequencies points toward an extremely high attenuation limited to the upper 5-10 mbsf. Another explanation could be a frequency-dependent conversion, which might be more efficient for low-frequencies due to a specific structure of the sediment. However, this is very speculative and future investigations in that topic are needed.

After taking the attenuation effects into account, it was shown that the reflection coefficients at the BSR derived from the GI-Gun data were still too small with respect to the MCS data. It is well known that a gradational transition in elastic parameters causes a frequency-dependent loss in reflection amplitude (*Richards, 1972*). Therefore, a model for the BSR interface was proposed based on results from vertical-incidence synthetic seismogram modeling, which consisted of a 1.5-2.5 m thick gradient zone and was able to explain the observed variation for the GI-Gun data, but yielded far too small coefficients for the high frequency Watergun data. Since the BSR signature has a rather chaotic and disrupted appearance in the high frequency data, it was suggested that the anomalously high amplitudes are a result of interferences at small-scale variations on a centimeter scale, which do not affect the lower frequency waves. The higher value of 2.5 m was obtained for a linear transition. If a smooth transition is assumed, the necessary thickness decreases to 1.5 m. Knowledge of the extent of the BSR interface is important because it strongly affects the P-wave AVO behaviour. The amplitude decreasing effect was shown to be most significant for vertical-incidence and to become less distinct with increasing offset. Thus, future AVO investigations should be aware of this and incorporate possible gradients in their processing.

The PP AVO analysis at six OBH/S locations showed that the AVO behaviour is strongly affected by lateral variations in BSR properties. To take these into account, closer instrument spacings, which allow a sorting into CDP gathers, would have been needed. An alternative processing of the existent data would have been to use the BSR reflection coefficients obtained from the streamer data and to determine calibration functions for the AVO curves. This approach was not performed but is likely to be able to smooth the AVO curves.

The traveltimes inversion of the OBH/S data yielded a detailed 2D-velocity field with assumed velocity uncertainties of ± 25 m/s. However, due to the restrictions regarding the inversion model parameterization, the final model assumes linear vertical velocity gradient

at each node. Since in reality, the vertical velocity functions are likely to have a non-linear character, this limitation has to be kept in mind. Nonetheless, an excellent fit of the traveltimes could be achieved, which indicates that the obtained model with the linear assumption is one of many non-unique possible models. In general, the ray coverage was sufficient for the velocity analysis, but at some locations between the instruments, no rays sampled the BSR and a better data redundancy by means of closer instrument spacings would have been desired. By comparison of the velocity model with the P-wave AVO analysis results from the OBH/S and MCS data, a poor correlation must be stated. This reflects that BSR amplitude anomalies are caused by changes in the free gas saturation below the BSR rather than by varying hydrate saturations. Some of the observed low velocity anomalies seem to be related to weak or chaotic BSR reflectivity, e.g. beneath OBH 43 or in the major thrust fault region, where rapid upward gas-rich fluid flow is suggested, but also to high BSR amplitudes, e.g. west of OBS 41. Here, the above mentioned co-existence of gas hydrate, free gas and brine might provide a mechanism for free gas to protrude into the GHSZ and to lower the P-wave velocity. Thus, the interpretation of the velocities in terms of hydrate saturation is strongly hampered by the possibility that sediments might contain significant amounts of hydrate despite of low velocities. Only where positive anomalies were found, the sediment velocities might not be affected by free gas, e.g. beneath OBS 49 and ODP Site 892. By taking a P-wave velocity of 1670 m/s above the BSR at OBS 49 and otherwise similar parameters to those at OBS 41, a hydrate saturation of 16 % is obtained for the grain contact model, which correlates well with the ODP results. Due to the above mentioned limited interpretative value of the P-wave velocities, a transformation of the complete P-wave velocity model to hydrate saturations was not performed.

The main focus of the regional SCS data analysis was to obtain information about variations in sedimentary structures and heat flow as well as about the distribution of gas hydrate and free gas saturations across northern Hydrate Ridge.

The structural analysis was able to link locations of active venting and carbonate chemoherm directly to subsurface features, which are characterized by chaotic reflectivity and disrupted BSR signatures in the seismic data. For example, a distinct upward deflection of the BSR along with enhanced reflectivity patterns could be observed beneath the *Sonne* chemoherm indicating that the build-ups of carbonate structures and sites of massive gas venting are coupled with tectonically-induced focused fluid flow from greater depths. The disruptive appearance of the BSR clearly reflects the activity of the gas and fluid regime at the ridge. In particular, the strongly disturbed sediment strata at the northern flank, where no evidence for carbonate structures is given by side-scan sonar backscatter data, is an indicator for unfocused fluid flow and massive occurrence of free gas possibly due to destabilizing gas hydrates. The derived three-dimensional structural image might be of use for future site selections with respect to active venting, hydrate and carbonate outcrops and chemosynthetic benthic fauna.

From the BSR depth distribution, a detailed map of the heat flow was deduced. The most remarkable feature is a N-S trending band of highly increased heatflow at the western flank of the ridge. The major eastward-dipping thrust fault is directly connected to the higher temperature gradients and might be a result of increased pressure from subduction-driven upward fluid flow. At the *Alvin* chemoherm, which is located at the surface outcrop

of the fault, the highest values of over 100 mW/m² were obtained. In general, areas of elevated heat flow indicate increased fluid and gas venting and thus the western flank can be suggested to represent the currently most active region at northern Hydrate Ridge.

The measured vertical-incidence BSR amplitudes along the SCS profiles provide an estimate of the possible regional distribution of gas hydrate and free gas. Since it was shown that the influence of the free gas saturation on the reflection strength dominates with respect to the possible variations in hydrate saturations, the map mainly reflects the distribution of free gas. However, it can be suggested that increased hydrate formation is linked to higher methane supplies and thus the BSR amplitude distribution is a good semi-quantitative indicator for both free gas and hydrate amounts. A perspective view of the high-resolution bathymetry draped with the BSR reflectivity is shown in Figure 8.1.

Free gas saturations of 0.4-0.6 % (6-10 %) are represented by the yellow to orange areas (amplitude range of 30000-38000) whereas lower values of 0.2-0.4 % (3-6 %) can be associated to the light blue, green and yellow colours (17000-30000). The three major regions of anomalously high BSR amplitudes represented by the orange to red colours (38000-44000) may contain free gas saturations of 0.6-1 % (10-15 %). The purple areas in the greater vicinity of the summit are locations where the BSR was disrupted and obscured probably by upward migrating gas-rich fluids and thus are indicative of even higher free gas saturations. In these areas, a fixed average value of 1 % (15 %) is assumed. An estimation of the regional gas hydrate distribution is not possible due to the poor correlation of the hydrate saturations derived from the P-wave velocities with the obtained free gas saturations. However, considering the above mentioned mechanisms which limit the interpretative value of the P-wave velocities, a general link between free gas and hydrate saturation is suggested. A conservative approach that assumes 0-5 % for the blue to yellow, 5-10 % for the yellow to orange and 10-15 % for the orange to red and purple areas is proposed.

In general, it can be inferred from the regional BSR amplitude distribution that free gas and gas hydrate saturations are highest west of the summit, which is consistent with the heat flow observations that active fluid flow from greater depth is focused to the western flank of the ridge. In order to classify the hydrate and free gas properties at northern Hydrate Ridge within a global context, a rough calculation of the total amount of free gas and hydrate in the sediment volume was done. The area for this calculation was restricted to 44°39'N-44°41.2'N and 125°4.5'W-125°8.1'W because here the SCS coverage was highest and interpolation errors could be minimized. The chosen region covers an area of 19.57 km² with a volume of the GHSZ of 1.67 km³. The free gas layer below the BSR has a volume of 0.98-1.96 km³ assuming a thickness of 50-100 m. The porosity is averaged to 60 % within the GHSZ and to 55 % for the free gas layer. With assumed densities of 0.06 g/cm³ and 0.91 g/cm³ for methane at the BSR depth (see Table 7.1) and methane hydrate, respectively, the total amounts $M_{g,h}$ can be estimated by:

$$M_{g,h} = V \cdot \rho_{g,h} \cdot \phi \cdot S_{g,h}. \quad (8.1)$$

A total amount of free methane below the BSR of 0.1-0.2 Mt for the suspension model and 1.6-3.2 Mt for the patchy distribution is obtained for the surveyed area. The amount of hydrate exceeds the free gas by far and can be estimated to be 48±10 Mt. The hydrate-bound amount of methane is obtained by assuming an average gas yield of 164 m³ per m³

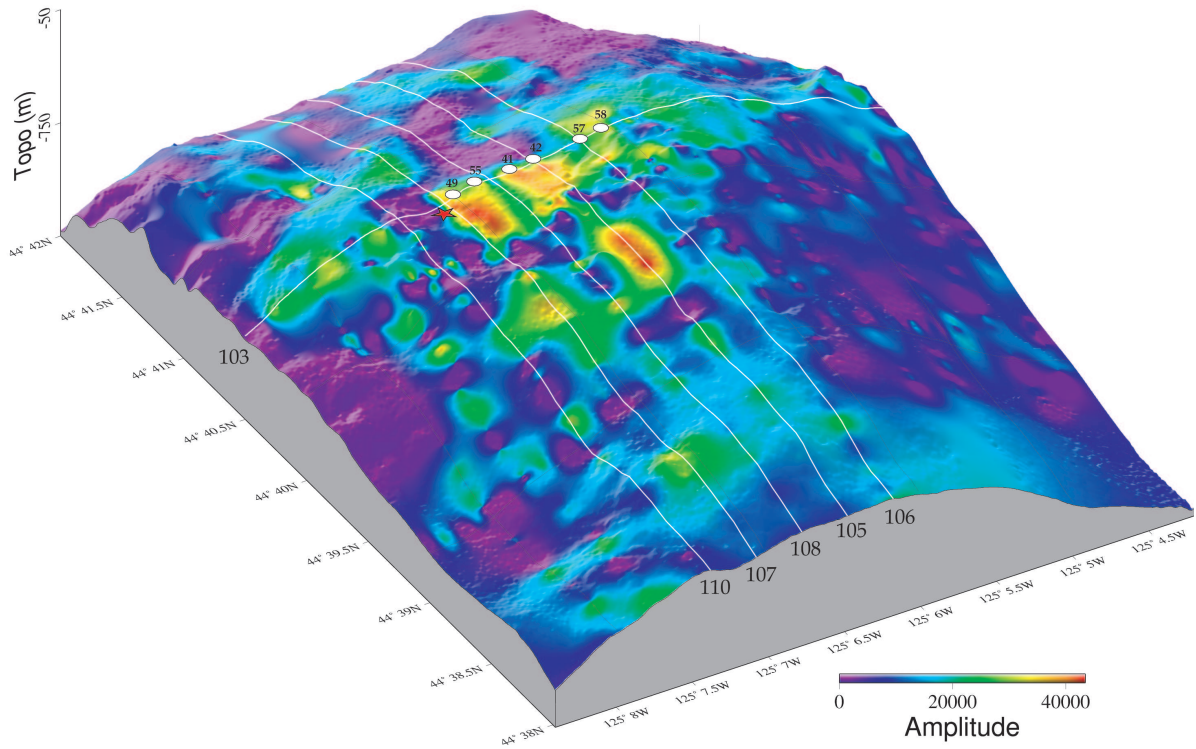


Figure 8.1: *BSR amplitude map derived from SCS profiles.*

hydrate and a methane density at standard conditions of 0.00068 g/cm^3 . This results in an amount of 4.7-7.1 Mt of methane stored in gas hydrates in the volume of the GHSZ in the surveyed area, which is equivalent to $2.8\text{-}4.3 \text{ Mt/km}^3$.

In total, 4.8 to 10.3 Mt of methane carbon can be suggested to be present in the specified area around the summit of northern Hydrate Ridge. This leads to an amount of $1.3\text{-}3.9 \text{ Mt/km}^3$ of hydrate-bound and free methane in the sediment above the free gas layer associated with the BSR.

The surveyed area at the northern summit constitutes approximately one-twentieth of the whole Hydrate Ridge, which covers an area of $\sim 375 \text{ km}^2$. Neglecting the fact that both the thickness of the GHSZ and the methane supply change across the ridge, a rough extrapolation might be suggested assuming similar hydrate saturations. With this, the total amount of hydrate-bound methane at Hydrate Ridge can be roughly estimated to be 0.09-0.14 Gt. Global estimates of the hydrate-bound gas in marine sediments have been recently reviewed by *Milkov* (2004), who suggest $\sim 500\text{-}2500 \text{ Gt}$ of methane carbon. Thus, the hydrate-bound methane carbon at Hydrate Ridge might represent about 0.004 to 0.03 % of the global budget.

In conclusion, the major results of the thesis can be summarized as follows:

- The BSR amplitude is dominantly controlled by the free gas saturation.
- Acquisition of multi-frequency data is essential for the determination of the compressional wave attenuation and of the thickness of the BSR transition zone.
- Average attenuation values of $Q_p = 150$ and $Q_s = 35$ were obtained within the GHSZ.
- The BSR is characterized by a gradient transition of 1.5-2.5 m width.
- A shear wave velocity above the BSR of 400 m/s was determined indicating that already small amounts of hydrate are sufficient to increase the shear modulus of the sediment.
- The hydrate saturation averages about 4-10 % within the GHSZ.
- The average free gas saturation is 0.5 % or 8 % for the suspension or the patchy gas model, respectively.
- The extent of the free gas layer is likely to exceed 50 m.
- Support for the co-existence of free gas, gas hydrate and brine within the GHSZ was found, which questions the principal method to infer hydrate saturations from P-wave velocities in active venting areas.
- A regional estimation lead to a total amount of hydrate-bound and free methane of 1.3-3.9 Mt/km³ in the sediment above the free gas layer associated with the BSR.

Chapter 9

Outlook

Several drawbacks regarding the seismic characterization of gas hydrates have been encountered during the presented analyses. These concern both acquisition and data processing issues.

Regarding the acquisition geometry, it was shown that in general the OBH/S spacing of ~ 200 m permitted a reliable velocity modeling, although it was insufficient at some locations. The spacing was at the limit for the velocity analysis and should be chosen smaller in future investigations. Especially for the AVO analysis, a much better ray coverage at the BSR with higher data redundancy is needed, which can be obtained with an instrument spacing of ~ 30 m for a target like Hydrate Ridge. Of course, the instrument spacing depends on the water depth and the BSR depth. It should be evaluated by synthetic modeling before the seismic data are acquired. Since it is very difficult, if not impossible, to deploy OBH/S instruments with the required accuracy in the common way, new concepts are needed, e.g. video-guided deployments. Moreover, although they are time-consuming, such deployments would be of great benefit regarding the control on seismometer position and coupling to the seafloor. Another possibility is the use of Ocean Bottom Cable (OBC) technology. Receiver spacings of 25 m and acquisition lengths of 4 km are well-suited for a detailed area-wide AVO analysis of PP and PS phases. However, at locations with rough seafloor morphology, e.g. carbonate crusts, OBCs are known to suffer from weak coupling. In addition, OBCs are very expensive and predominantly used by the oil and gas exploration industry. In academic research, there has only been a single application to gas hydrates at the Storegga Slide yet (*Andreassen et al.*, 2003). In this case, the BSR did not produce P-S converted waves.

Operating the seismic source at the sea surface can also be considered as a shortcoming in acquisition geometry. With a source near or at the seafloor, the Fresnel zone is smaller and a much higher lateral resolution is achievable. Deep-towed high-resolution source and streamer configurations have been developed and already used in gas hydrate research in recent years (e.g. *Wood et al.*, 2002).

Concerning the data processing, several suggestions arise from the made experiences. In order to increase the lateral resolution, a migration of the OBH/S data is recommendable. However, to assure a reliable amplitude analysis, an amplitude-preserving algorithm is needed. *Haris* (2003) successfully applied a true-amplitude migration to synthetic OBH data. For the OBS data true-amplitude multicomponent elastic migration algorithms are

needed which have been developed recently (e.g. *Goertz, 2002*).

The type of transition at the BSR and interference effects due to gas layers and fine-scaled variations play a significant role in BSR investigations. By using synthetic forward modeling, these effects can only be roughly investigated. Full waveform inversion methods include both amplitude and phase information and have shown to be capable of resolving these features accurately. With increasing computer capacities, future investigations will be able to obtain area-wide detailed constraints on the shape of the BSR interface.

A drawback of the rock physics models available at present is that they are based on theoretical assumptions concerning the sediment structure, which might be far away from reality, e.g. packages of identical spheres. Thus, they fail to predict accurate velocities for specific sediments, e.g. marine silty-clays, which are commonly associated with continental margin settings. Here, further combined experimental and theoretical studies are needed.

Bibliography

- Aki, K., and P. G. Richards, *Quantitative Seismology: Theory and Methods*, 932 pp., W.H. Freeman and Co., San Francisco, 1980.
- Andreassen, K., K. A. Berteussen, H. Sognnes, K. Henneberg, J. Langhammer, and J. Mienert, Multicomponent ocean bottom cable data in gas hydrate investigation offshore of Norway, *J. Geophys. Res.*, *108*, 2399, doi:10.1029/2002JB002245, 2003.
- Ayres, A., and F. Theilen, Preliminary laboratory investigations into attenuation of compressional and shear waves on near-surface sediments, *Geophys. Prospect.*, *49*, 120–127, 2001.
- Bialas, J., and E. R. Flueh, Ocean Bottom Seismometers, *Sea Technology*, *40*(4), 41–46, 1999.
- Bohrmann, G., J. Greinert, E. Suess, and M. E. Torres, Authigenic carbonates from the Cascadia subduction zone and their relation to gas hydrate stability, *Geology*, *26*, 647–650, 1998.
- Bohrmann, G., P. Linke, E. Suess, and O. Pfannkuche, Cruise Report SO143 TECFLUX, *GEOMAR Report 93*, GEOMAR Research Center for Marine Geosciences, ISSN 0936-5788, 2000.
- Bohrmann, J. G. G., and E. Suess, Gas hydrate-associated carbonates and methane-venting at Hydrate Ridge: classification, distribution, and origin of authigenic lithologies, in *Natural Gas Hydrates: Occurrence, Distribution and Detection*, *Geophys. Monogr. Ser.*, vol. 124, edited by C. K. Paull and W. Dillon, pp. 99–113, AGU, 2001.
- Bromirski, P. D., N. Frazer, and F. K. Duennebier, Sediment q_β from spatial ratios of converted shear reflections, in *Shear waves in marine sediments*, edited by J. Hovem, M. Richardson, and R. Stoll, pp. 361–368, Kluwer Academic Publishers, 1991.
- Brown, K. M., C. Goldfinger, G. Bohrmann, M. Torres, M. Tryon, C. Jung, E. Suess, H. Sahling, and A. M. Trehu, Geological and hydrogeologic interrelationships around seeps and gas vent regions on hydrate ridge: seabed observation, in *Suppl. to Eos*, p. 510, AGU Fall Meeting, 1999.
- Carcione, J. M., and U. Tinivella, Bottom-simulating reflectors: Seismic velocities and AVO effects, *Geophysics*, *65*, 54–67, 2000.

- Carson, B., E. Seke, V. Paskevich, and M. L. Holmes, Fluid expulsion sites on the Cascadia accretionary prism: mapping diagenetic deposits with processed GLORIA imagery, *J. Geophys. Res.*, *99*, 11.959–11.969, 1994.
- Castagna, J. P., and M. Backus, *Offset-Dependent Reflectivity - Theory and Practice of AVO Analysis*, Investigations in Geophysics, No.8, Society of Exploration Geophysicists, Tulsa, Oklahoma, 1993.
- Chand, S., T. A. Minshull, D. Gei, and J. M. Carcione, Elastic velocity models for gas-hydrate-bearing sediments - a comparison, *Geophys. J. Int.*, *158*, 1–18, doi:10.1111/j.1365-246X.2004.02387.x, in press, 2004.
- Chapman, N. R., J. F. Gettrust, R. Walla, D. Hannay, G. D. Spence, W. T. Wood, and R. D. Hyndman, High-resolution, deep-towed, multichannel seismic survey of deep-sea gas hydrates off western Canada, *Geophysics*, *67*(4), 1038–1047, 2002.
- Clague, D., N. Maher, and C. K. Paull, High-resolution multibeam survey of Hydrate Ridge, offshore Oregon, in *Natural Gas Hydrates: Occurrence, Distribution and Detection*, *Geophys. Monogr. Ser.*, vol. 124, edited by C. K. Paull and W. Dillon, pp. 297–306, AGU, 2001.
- Clenell, B., and A. Maltman, Microstructures in accreted sediments of the Cascadia Margin, in *Proc.ODP, Sci. Results*, vol. 146, edited by B. Carson, G. Westbrook, R. Musgrave, and E. Suess, pp. 201–216, Texas AM University, Ocean Drilling Program, College Station, TX, United States, 1995.
- Cochrane, G. R., B. T. R. Lewis, and K. J. McClain, Structure and subduction processes along the Oregon-Washington margin, *Pure Appl. Geophys.*, *128*, 767–800, 1988.
- Collett, T. S., Natural Gas Hydrate as a Potential Energy Resource, in *Natural Gas Hydrate in Oceanic and Permafrost Environments, Coastal Systems and Continental Margins*, vol. 5, edited by M. Max, pp. 123–136, Kluwer Academic Publishers, 2003.
- Davis, E. E., R. D. Hyndman, and H. Villinger, Rates of Fluid Expulsion Across the Northern Cascadia Accretionary Prism: Constraints From New Heat Flow and Multichannel Seismic Reflection Data, *J. Geophys. Res.*, *95*, 8869–8889, 1990.
- Davis, E. E., K. Becker, K. Wang, and B. Carson, Long-term observations of pressure and temperature in Hole 892B, Cascadia accretionary prism, in *Proc.ODP, Sci. Results*, vol. 146, edited by B. Carson, G. Westbrook, R. Musgrave, and E. Suess, pp. 299–311, Texas AM University, Ocean Drilling Program, College Station, TX, United States, 1995.
- De, G. S., D. F. Winterstein, and M. A. Meadows, Comparison of P- and S-wave velocities and Q's from VSP and sonic log data, *Geophysics*, *59*, 1512–1529, 1994.
- DeMets, C., R. G. Gordon, D. F. Argus, and S. Stein, Current plate motions, *Geophys. J. Int.*, *101*, 425–478, 1990.
- Dickens, G. R., and M. S. Quinby-Hunt, Methane hydrate stability in seawater, *Geophys. Res. Lett.*, *21*, 2115–2118, 1994.

- Dickens, G. R., C. K. Paull, and P. Wallace, Direct measurements of in situ methane quantities in a large gas-hydrate reservoir, *Nature*, *385*, 426–428, 1997.
- Domenico, S. N., Effect of brine-gas mixture on velocity in an unconsolidated sand reservoir, *Geophysics*, *41*, 882–894, 1976.
- Dvorkin, J., A. Nur, and H. Yin, Effective properties of cemented granular material, *Mechanics of Materials*, *18*, 351–366, 1994.
- Dvorkin, J., M. Prasad, A. Sakai, and D. Lavoie, Elasticity of marine sediments: Rock physics modeling, *Geophys. Res. Lett.*, *26*, 1781–1784, 1999.
- Ecker, C., J. Dvorkin, and A. Nur, Sediments with gas hydrates: Internal structure from seismic AVO, *Geophysics*, *63*, 1659–1669, 1998.
- Ecker, C., J. Dvorkin, and A. Nur, Estimating the amount of gas hydrate and free gas from marine seismic data, *Geophysics*, *65*, 565–573, 2000.
- Flueh, E. R., and J. Bialas, A digital, high data capacity ocean bottom recorder for seismic investigations, *Int. Underwater Systems Design*, *18*(3), 18–20, 1996.
- Flueh, E. R., D. Klaeschen, and J. Bialas, Options for multi-component seismic data acquisition in deep water, *First Break*, *20*(12), 764–769, 2002.
- Gassmann, F., Über die Elastizität poröser Medien, *Vierteljahr. Naturforsch. Gesell. Zürich*, *96*, 1–23, 1951.
- Geertsma, J., and D. C. Smit, Some aspects of elastic wave propagation in fluid-saturated porous solids, *Geophysics*, *26*, 169–181, 1961.
- Gei, D., and J. M. Carcione, Acoustic properties of sediments saturated with gas hydrates, free gas and water, *Geophys. Prospecting*, *51*, 141–157, 2003.
- Goertz, A., *True-amplitude multicomponent migration of elastic wavefields*, 131 pp., Logos-Verlag, 2002.
- Greinert, J., Rezent submarine Mineralbildungen: Abbild geochemischer Prozesse an aktiven Fluidaustrittsstellen im Aleuten- und Cascadia-Akkretionskomplex, Geomar Report 87, University of Kiel, PhD thesis, 1999.
- Guerin, G., D. Goldberg, and A. Meltser, Characterization of in situ elastic properties of gas hydrate-bearing sediments on the Blake Ridge, *J. Geophys. Res.*, *104*, 17.781–17.795, 1999.
- Hamilton, E. L., Elastic properties of marine sediments, *Geophysics*, *76*, 579–604, 1971.
- Hamilton, E. L., Compressional-wave attenuation in marine sediments, *Geophysics*, *37*, 620–646, 1972.
- Hamilton, E. L., Shear-wave velocity versus depth in marine sediments: a review, *J. Geophys. Res.*, *41*, 985–996, 1976a.

- Hamilton, E. L., Variations of density and porosity with depth in deep-sea sediments, *J. Sediment. Petrol.*, *46*, 280–300, 1976b.
- Hamilton, E. L., Sound velocity gradients in marine sediments, *J. Acoust. Soc. Am.*, *65*, 909–922, 1979.
- Handa, Y. P., Effect of hydrostatic pressure and salinity on the stability of gas hydrates, *J. Phys. Chem.*, *94*, 2651–2657, 1990.
- Haq, B. U., Climatic Impact of Natural Gas Hydrate, in *Natural Gas Hydrate in Oceanic and Permafrost Environments, Coastal Systems and Continental Margins*, vol. 5, edited by M. Max, pp. 137–148, Kluwer Academic Publishers, 2003.
- Haris, A., Amplitude-preserving migration and its application to imaging of a bsr in marine multichannel seismic reflection data, Ph.D. thesis, University of Kiel, 2003.
- Helgerud, M. B., J. Dvorkin, A. Nur, A. Sakai, and T. S. Collett, Elastic-wave velocity in marine sediments with gas hydrates: effective medium modelling, *Geophys. Res. Lett.*, *26*, 2021–2024, 1999.
- Helgerud, M. B., W. F. Waite, S. H. Kirby, and A. Nur, Measured temperature and pressure dependence of v_p and v_s in compacted, polycrystalline sI methane and sII methane-ethane hydrate, *Canadian Journal of Physics*, *81*, 47–53, 2003.
- Herzig, P., E. Suess, and P. Linke, Cruise Report SO109 Hydrotrace, *GEOMAR Report 58*, GEOMAR Research Center for Marine Geosciences, iSSN 0936-5788, 1997.
- Hill, R., The elastic behaviour of crystalline aggregate, *Proc. Phys. Soc., London*, *A65*, 349–354, 1952.
- Holbrook, W. S., H. Hoskins, W. T. Wood, R. A. Stephen, D. Lizzarralde, and the Leg 164 Science Party, Methane hydrate and free gas on the Blake Ridge from vertical seismic profiling, *Science*, *273*, 1840–1843, 1996.
- Hovland, M., D. Lysne, and M. Whiticar, Gas hydrate and sediment gas composition, Hole 892A, in *Proc. ODP, Sci. Results*, vol. 146, edited by B. Carson, G. Westbrook, R. Musgrave, and E. Suess, pp. 151–161, Texas AM University, Ocean Drilling Program, College Station, TX, United States, 1995.
- Hyndman, R. D., G. D. Spence, R. Chapman, M. Riedel, and R. N. Edwards, Geophysical studies of marine gas hydrate in northern Cascadia, in *Natural Gas Hydrates: Occurrence, Distribution and Detection*, *Geophys. Monogr. Ser.*, vol. 124, edited by C. K. Paull and W. Dillon, pp. 273–295, AGU, 2001.
- Jakobsen, M., J. A. Hudson, T. A. Minshull, and S. C. Singh, Elastic properties of hydrate-bearing sediments using effective-medium theory, *J. Geophys. Res.*, *105*, 561–577, 2000.
- Jarrard, R. D., M. E. MacKay, G. K. Westbrook, and E. J. Screaton, Log-based porosity of ODP Sites on the Cascadia accretionary prism, in *Proc. ODP, Sci. Results*, vol. 146, edited by B. Carson, G. Westbrook, R. Musgrave, and E. Suess, pp. 313–335, Texas AM University, Ocean Drilling Program, College Station, TX, United States, 1995.

- Johnson, J. E., C. Goldfinger, and E. Suess, Geophysical constraints on the surface distribution of authigenic carbonates across the Hydrate Ridge region, Cascadia margin, *Marine Geol.*, 202, 79–120, 2003.
- Kastner, M., K. A. Kvenvolden, M. J. Whiticar, A. Camerlenghi, and T. D. Lorenson, Relation between pore fluid chemistry and gas hydrates associated with Bottom-Simulating Reflectors at the Cascadia margin, Sites 889 and 892, in *Proc. ODP, Sci. Results*, vol. 146, edited by B. Carson, G. Westbrook, R. Musgrave, and E. Suess, pp. 175–187, Texas AM University, Ocean Drilling Program, College Station, TX, United States, 1995.
- Kastner, M., K. A. Kvenvolden, and T. D. Lorenson, Chemistry, isotopic composition, and origin of a methane-hydrogen sulfide hydrate at the Cascadia subduction zone, *Earth Planet. Sci. Lett.*, 156, 173–183, 1998.
- Klaeschen, D., A. Kopf, M. Arsenault, and J. Bialas, Cruise Report SO150 HYDGAS - Quantification of gas hydrates and gas in the sediments of the Cascadia accretionary wedge using seismic methods, *Report*, GEOMAR Research Center for Marine Geosciences, 2001.
- Klaucke, I., G. Bohrmann, and W. Weinrebe, Estimation of the regional methane efflux on Hydrate Ridge, Oregon, *G-cubed*, submitted.
- Kulm, L. D., R. von Huene, J. R. Duncan, J. C. Ingle, S. Kling, D. J. W. Piper, R. M. Pratt, H. J. Schrader, S. W. Wise, L. F. Musich, and O. E. Weser, *Initial Reports of the Deep Sea Drilling Project*, vol. 18, Texas AM University, Ocean Drilling Program, College Station, TX, United States, ocean Margin Drilling Program Regional Atlas Series, Atlas 1, 1973.
- Kulm, L. D., M. Thornburg-Todd, and P. Dang-Steven, *Western North American Continental Margin and Adjacent Ocean Floor off Oregon and Washington*, Mar. Sci. Int., Woods Hole, ocean Margin Drilling Program Regional Atlas Series, Atlas 1, 1984.
- Kulm, L. D., E. Suess, J. C. Moore, B. Carson, B. T. Lewis, S. D. Ritger, D. C. Kadko, M. Thornburg, R. W. Embly, W. D. Rugh, G. J. Massoth, M. G. Langseth, G. R. Cochrane, and R. L. Scamman, Oregon subduction zone: Venting, fauna and carbonates, *Science*, 231, 561–566, 1986.
- Kvenvolden, K. A., Gas hydrates - geological perspective and global change, *Rev. Geophys.*, 31, 173–183, 1993.
- Kvenvolden, K. A., and T. D. Lorenson, The global occurrence of natural gas hydrate, in *Natural Gas Hydrates: Occurrence, Distribution and Detection*, *Geophys. Monogr. Ser.*, vol. 124, edited by C. K. Paull and W. Dillon, pp. 3–18, AGU, 2001.
- Lee, M. W., D. R. Hutchinson, T. S. Collett, and W. P. Dillon, Seismic velocities for hydrate-bearing sediments using weighted equation, *J. Geophys. Res.*, 101, 20.347–20.358, 1996.
- Linke, P., and E. Suess, Cruise Report SO148 TECFLUX-II - tectonically-induced material fluxes, *GEOMAR Report 98*, GEOMAR Research Center for Marine Geosciences, ISSN 0936-5788, 2001.

- Linke, P., E. Suess, M. E. Torres, V. Martens, W. D. Rugh, W. Ziebis, and L. D. Kulm, In situ measurements of fluid flow from cold seeps at the active continental margins, *Deep Sea Research*, *41*, 721–739, 1994.
- MacKay, M. E., Structural variation and landward vergence at the toe of the Oregon accretionary prism, *Tectonics*, *14*, 1309–1320, 1995.
- MacKay, M. E., G. F. Moore, G. R. Cochrane, J. C. Moore, and L. D. Kulm, Landward vergence and oblique structural trends in the Oregon margin accretionary prism: Implications and effect on fluid flow, *Earth Planet. Sci. Lett.*, *109*, 477–491, 1992.
- MacKay, M. E., R. D. Jarrad, G. K. Westbrook, R. D. Hyndman, and the Shipboard Scientific Party of ODP Leg 146, Origin of bottom simulating reflectors: geophysical evidence from the Cascadia accretionary prism, *Geology*, *22*, 459–462, 1994.
- MacKay, M. E., R. D. Jarrad, G. K. Westbrook, R. D. Hyndman, and the Shipboard Scientific Party of ODP Leg 146, Technical notes and additions to: Origin of bottom simulating reflectors: geophysical evidence from the Cascadia accretionary prism, in *Proc. ODP, Sci. Results*, vol. 146, edited by B. Carson, G. Westbrook, R. Musgrave, and E. Suess, pp. 461–463, Texas AM University, Ocean Drilling Program, College Station, TX, United States, 1995.
- Mavko, G. T., T. Mukherji, and J. Dvorkin, *The Rock Physics Handbook-Tools for Seismic Analysis in Porous Media*, Cambridge University Press, New York, 1998.
- Milkov, A. V., Global estimate of hydrate-bound gas in marine sediments: how much is really out there?, *Earth-Science Reviews*, *66*, 183–197, 2004.
- Milkov, A. V., G. R. Dickens, G. E. Claypool, Y. J. Lee, W. S. Borowski, M. E. Torres, W. Xu, H. Tomaru, A. M. Trehu, and P. Schultheiss, Co-existence of gas hydrate, free gas, and brine within the regional gas hydrate stability zone at Hydrate Ridge (Oregon margin): evidence from prolonged degassing of a pressurized core, *Earth Planet. Sci. Lett.*, *222*, 829–843, 2004.
- Minshull, T. A., S. C. Singh, and G. K. Westbrook, Seismic velocity structure at a gas hydrate reflector offshore western Colombia, from full waveform inversion, *J. Geophys. Res.*, *99*, 4715–4734, 1994.
- Moran, K., W. G. D. Gray, and C. A. Jarrett, Permeability and stress history of sediment from the Cascadia margin, in *Proc. ODP, Sci. Results*, vol. 146, edited by B. Carson, G. Westbrook, R. Musgrave, and E. Suess, pp. 275–280, Texas AM University, Ocean Drilling Program, College Station, TX, United States, 1995.
- Otterbein, C., Untersuchung der lateralen Auflösung verschiedener Meßsysteme der marinen Reflexionsseismik, Diploma thesis, University of Kiel, 1997.
- Papenberg, C. A., Seismic Investigations of a Bottom Simulating Reflector: Implications on Gas Hydrate and Free Gas at Southern Hydrate Ridge, Ph.D. thesis, University of Kiel, in prep.

- Paull, C. K., W. Ussler III, and W. P. Dillon, Potential Role of Gas Hydrate Decomposition in Generating Submarine Slope Failures, in *Natural Gas Hydrate in Oceanic and Permafrost Environments, Coastal Systems and Continental Margins*, vol. 5, edited by M. Max, pp. 149–156, Kluwer Academic Publishers, 2003.
- Pfannkuche, O., A. Eisenhauer, P. Linke, and C. Utecht, Cruise Report SO165 OTEGA I, *GEOMAR Report 112*, GEOMAR Research Center for Marine Geosciences, iSSN 0936-5788, 2002.
- Reuss, A., Berechnung der Fließgrenzen von Mischkristallen auf Grund der Plastizitätsbedingung für Einkristalle, *Zeitschr. für Angewandte Math. und Mech.*, 9, 49–58, 1929.
- Richards, P. G., Seismic waves reflected from velocity gradient anomalies within the earth's upper mantle, *Zeitschr. Geophys.*, 38, 517–527, 1972.
- Ruppel, C., Anomalously cold temperatures observed at the base of gas hydrate stability zone on the US Atlantic passive margin, *Geology*, 25, 699–702, 1997.
- Sample, J. C., Isotopic evidence from authigenic carbonates for rapid upward fluid flow in accretionary wedges, *Geology*, 24, 897–900, 1996.
- Sample, J. C., and M. R. Reid, Contrasting hydrogeologic regimes along strike-slip and thrust faults in the Oregon convergent margin: Evidence from the chemistry of syntectonic carbonate cements and veins, *Geol. Soc. Am. Bull.*, 110, 48–59, 1998.
- Schmidt, H., OASES Version 2.2: User guide and reference manual, *Tech. rep.*, Department of Ocean Engineering, Massachusetts Institute of Technology, 1999.
- Schnurle, P., C. S. Liu, T. H. Hsiuan, T. K. Wang, K. MacIntosh, and D. L. Reed, Characteristics of Gas Hydrate and free gas Offshore Southwestern taiwan from a Combined MCS/OBS Data Analysis, *MGR, special issue*, submitted.
- Scranton, M., and P. G. Brewer, Consumption of dissolved methane in the deep ocean, *Limnol. Oceanol.*, 15, 883–886, 1978.
- Sheriff, R. E., Nomogramm for Fresnel-zone calculation, *Geophysics*, 45, 968–972, 1980.
- Sheriff, R. E., and L. P. Geldart, *Exploration Seismology*, 2nd ed., Cambridge University Press, 1995.
- Shipley, T. H., M. H. Houston, R. T. Buffler, F. J. Shaub, K. J. McMillen, J. W. Ladd, and J. L. Worzel, Seismic evidence for widespread possible gas hydrate horizons on continental slopes and rises, *Am. Assoc. Pet. Geol. Bull.*, 63, 2204–2213, 1979.
- Shuey, R. T., A simplification of the Zoeppritz equations, *Geophysics*, 50, 609–614, 1985.
- Singh, S. C., and T. A. Minshull, Velocity structure of a gas hydrate reflector at Ocean Drilling Program site 889 from a global seismic waveform inversion, *J. Geophys. Res.*, 99, 24.221–24.233, 1994.
- Singh, S. C., T. A. Minshull, and G. D. Spence, Velocity structure of a gas hydrate reflector, *Science*, 260, 204–207, 1993.

- Sloan, E. D., *Clathrate Hydrates of Natural Gases*, second ed., Marcel Dekker, 1998.
- Snavely, P. D., Tertiary geologic framework, neotectonics, and petroleum potential of the Oregon-Washington continental margin, in *Geology and Resource Potential of the Continental Margin of Western North America and Adjacent Ocean Basins-Beaufort Sea to Baja California*, *Earth Sci. Ser.*, vol. 5, edited by D. W. Scholl, A. Grantz, and J. G. Vedder, pp. 305–335, Circum-Pacific Council for Energy and Mineral Resources, Houston, Tex., 1987.
- Snavely, P. D., H. C. Wagner, and D. L. Lander, Geologic cross section of the central Oregon continental margin, *Geol. Soc. Am. Map Chart Ser.*, MC-28J, 1980.
- Spence, G. D., R. D. Hyndman, N. R. Chapman, M. Riedel, N. Edwards, and J. Yuan, Cascadia margin, northeast Pacific ocean: hydrate distribution from geophysical investigations, in *Natural Gas Hydrate in Oceanic and Permafrost Environments, Coastal Systems and Continental Margins*, vol. 5, edited by M. Max, pp. 183–198, Kluwer Academic Publishers, 2003.
- Suess, E., and G. Bohrmann, Cruise Report SO110 SO-RO, *GEOMAR Report 59*, GEOMAR Research Center for Marine Geosciences, ISSN 0936-5788, 1997.
- Suess, E., M. E. Torres, G. Bohrmann, R. W. Collier, J. Greinert, P. Linke, G. Rehder, A. Trehu, K. Wallmann, G. Winckler, and E. Zuleger, Gas hydrate destabilization: enhanced dewatering, benthic material turnover and large methane plumes at the Cascadia convergent margin, *Earth Planet. Sci. Lett.*, 170, 1–15, 1999.
- Torres, M. E., J. McManus, D. E. Hammond, M. A. de Angelis, K. U. Heeschen, S. L. Colbert, M. D. Tryon, K. M. Brown, and E. Suess, Fluid and chemical fluxes in and out of sediments hosting methane hydrate deposits on Hydrate Ridge, OR, I: Hydrological provinces, *Earth Planet. Sci. Lett.*, 201, 525–540, 2002.
- Trehu, A. M., and E. R. Flueh, Estimating the thickness of the free gas zone beneath Hydrate Ridge, Oregon continental margin, from seismic velocities and attenuation, *J. Geophys. Res.*, 106, 2035–2045, 2001.
- Trehu, A. M., G. Lin, E. Maxwell, and C. Goldfinger, A seismic reflection profile across the Cascadia subduction zone offshore central Oregon: New constraints on methane distribution and crustal structure, *J. Geophys. Res.*, 100, 15.101–15.116, 1995.
- Trehu, A. M., M. E. Torres, G. Moore, E. Suess, and G. Bohrmann, Temporal and spatial evolution of a gas hydrate-bearing accretionary ridge on the Oregon continental margin, *Geology*, 27, 939–942, 1999.
- Trehu, A. M., N. L. Bangs, M. A. Arsenault, G. Bohrmann, C. Goldfinger, J. E. Johnson, Y. Nakamura, and M. E. Torres, Complex subsurface plumbing beneath southern Hydrate Ridge, Oregon continental margin, from high-resolution 3D seismic reflection data, *Proceedings of the 4th International Conference on Gas Hydrates, Yokohama, Japan*, 2002.

- Trehu, A. M., G. Bohrmann, F. R. Rack, and M. E. T. et al., *Proc. ODP, Initial reports*, vol. 204, Texas AM University, Ocean Drilling Program, College Station, TX 77845-9547, USA, 2003.
- Trehu, A. M., P. E. Long, M. E. Torres, G. Bohrmann, F. R. Rack, and T. S. C. et al., Three-dimensional distribution of gas hydrate beneath southern Hydrate Ridge: constraints from ODP Leg 204, *Earth Planet. Sci. Lett.*, *222*, 845–862, 2004.
- Westbrook, G. K., B. Carson, and R. J. M. et al., *Proc. ODP, Initial reports*, vol. 146, Texas AM University, Ocean Drilling Program, College Station, TX, United States, 1994.
- White, R. E., The accuracy of estimating Q from seismic data, *Geophysics*, *57*, 1508–1511, 1992.
- Wood, W., J. Gettrust, N. Chapman, G. Spence, and R. D. Hyndman, Decreased stability of methane hydrates in marine sediments owing to surface roughness, *Nature*, *420*, 656–660, 2002.
- Wood, W. T., W. S. Holbrook, and H. Hoskins, In situ measurements of P-wave attenuation in the methane hydrate- and gas-bearing sediments of the Blake Ridge, in *Proc. ODP, Sci. Results*, vol. 164, edited by C. Paull, R. Matsumoto, P. Wallace, and W. Dillon, pp. 265–272, Texas AM University, Ocean Drilling Program, College Station, TX, United States, 2000.
- Xu, W., and C. Ruppel, Predicting the occurrence, distribution and evolution of methane gas hydrate in porous sediments, *J. Geophys. Res.*, *104*, 5081–5095, 1999.
- Yefremova, A. G., and B. P. Zhizhchenko, Occurrence of crystal hydrates of gas in sediments of modern marine basins, *Doklady Akademii Nauk SSSR*, *214*, 1179–1181, 1974.
- Zelt, C. A., and R. B. Smith, Seismic travelttime inversion for 2-d crustal velocity structure, *Geophys. J. Int.*, *108*, 16–34, 1992.
- Zillmer, M., E. R. Flueh, and J. Petersen, Seismic investigation of a bottom simulating reflector and quantification of gas hydrate in the Black Sea, *Geophys. J. Int.*, submitted.
- Zoeppritz, K., Über Reflexion und Durchgang seismischer Wellen durch Unstetigkeitsflächen, *Aus den Nachrichten der Königlichen Gesellschaft der Wissenschaften zu Göttingen, Mathematisch-physikalische Klasse*, 66–84, 1919.
- Zwart, G., J. C. Moore, and G. R. Cochran, Variations in temperature gradients identify active faults in the Oregon accretionary prism, *Earth Planet. Sci. Lett.*, *139*, 485–495, 1996.

Appendix A

Model statistics

```
-----  
total of 21072 rays consisting of 976440 points were traced  
model consists of 3 layers and 379 blocks  
-----
```

```
Number of data points used: 2680  
RMS travelttime residual: 0.001  
Normalized chi-squared: 0.519
```

phase	npts	Trms	chi-squared
2	2680	0.001	0.519

shot	dir	npts	Trms	chi-squared
0.698	-1	12	0.001	0.338
0.698	1	49	0.002	0.999
0.910	-1	68	0.001	0.562
0.910	1	150	0.002	0.706
1.102	1	87	0.001	0.265
1.291	-1	86	0.001	0.362
1.291	1	67	0.002	0.790
1.440	-1	81	0.001	0.324
1.440	1	29	0.002	0.875
1.620	-1	9	0.002	0.660
1.620	1	10	0.001	0.143
1.749	-1	15	0.002	0.837
1.749	1	103	0.001	0.372
2.000	-1	79	0.002	0.931
2.000	1	158	0.002	0.686
2.101	-1	160	0.002	0.585
2.101	1	172	0.002	0.589
2.184	-1	180	0.002	0.875
2.184	1	149	0.001	0.129
2.485	-1	187	0.002	0.749
2.485	1	132	0.001	0.206
2.693	-1	35	0.002	0.647
2.693	1	49	0.002	0.575
2.891	-1	177	0.002	0.776
2.891	1	64	0.001	0.132
3.104	-1	57	0.001	0.270
3.104	1	72	0.001	0.297
3.286	-1	186	0.001	0.177
3.286	1	57	0.000	0.056

Figure A.1: χ^2 and rms misfit measures for final OBH velocity model derived by travelttime inversion.

Acknowledgments

I would like to thank Dr. Dirk Klaeschen for his ongoing advice and many helpful discussions over the past years. His assistance was essential to this study, and it significantly deepened my knowledge of seismic data processing.

I am very grateful to Prof. Dr. Ernst Flueh for his continuous support and his friendly advice. He gave me the opportunity to participate in numerous research cruises, which I thoroughly enjoyed. Because of his help I was able to attend many scientific meetings. I especially appreciate the continuous financial support over the past years.

I would like to thank Cord Papenberg for the numerous discussions on gas hydrates and for being such a nice companion in dealing with the daily problems of a geophysicist.

Furthermore, I thank Anne Krabbenhöft, Lars Planert, Thomas Leythaeuser, Heidrun Kopp, Ivonne Arroyo and Wendy Perez for their encouraging company and the cheerful time that we spent together.

Many thanks to Dr. Matthias Zillmer for his friendly advice, which significantly helped to clarify many aspects of rock physics modeling.

I would like to thank Dr. Jörg Bialas for providing extended financial support.

I thank Prof. Dr. Wolfgang Rabbel for spontaneously agreeing to act as co-referee.

Many thanks to all the members of the Marine Geodynamics Department for their assistance and the nice working atmosphere in recent years.

Curriculum Vitae

Name:	Carl Jörg Petersen
Date and Place of birth:	26 April 1974 in Geesthacht
Citizenship:	German
1980-1984:	Franz-Böttcher-Grundschule, Heiligenhafen
1984-1993:	Freiherr-vom-Stein-Gymnasium, Oldenburg/Holstein
1993-1994:	Military service, Neumünster
1994-1998:	Study of Physics at Christian-Albrechts-Universität zu Kiel
1998-2001:	Study of Geophysics at Christian-Albrechts-Universität zu Kiel
since 2001:	Research Assistant at IFM-GEOMAR

Eidesstattliche Erklärung

Hiermit versichere ich an Eides Statt, daß ich diese Arbeit ausschließlich unter Anleitung meiner wissenschaftlichen Lehrer und unter Verwendung der angegebenen Hilfsmittel angefertigt habe.

Kiel,